3-20-2014 12:00 AM

Quantitative Susceptibility Imaging of Tissue Microstructure Using Ultra-High Field MRI

David A. Rudko
The University of Western Ontario

Supervisor
Dr. Ravi S. Menon
The University of Western Ontario

Graduate Program in Physics
A thesis submitted in partial fulfillment of the requirements for the degree in Doctor of Philosophy

Recommended Citation

Rudko, David A., "Quantitative Susceptibility Imaging of Tissue Microstructure Using Ultra-High Field MRI" (2014). *Electronic Thesis and Dissertation Repository*. 1922.
https://ir.lib.uwo.ca/etd/1922

QUANTITATIVE SUSCEPTIBILITY IMAGING OF TISSUE MICROSTRUCTURE USING ULTRA-HIGH FIELD MRI

(Thesis format: Integrated Article)

by

David Alexander Rudko

Graduate Program in Physics and Astronomy

A thesis submitted in partial fulfillment
of the requirements for the degree of

Doctor of Philosophy

The School of Graduate and Postdoctoral Studies
The University of Western Ontario
London, Ontario, Canada

Abstract

This thesis has used ultra-high field (UHF) magnetic resonance imaging (MRI) to investigate the fundamental relationships between tissue microstructure and such susceptibility-based contrast parameters as the apparent transverse relaxation rate (R_2^*), the local Larmor frequency shift (LFS) and quantitative volume magnetic susceptibility (QS). The interaction of magnetic fields with biological tissues results in shifts in the LFS which can be used to distinguish underlying cellular architecture. The LFS is also linked to the relaxation properties of tissues in a gradient echo MRI sequence. Equally relevant, histological analysis has identified iron and myelin as two major sources of the LFS. As a result, computation of LFS and the associated volume magnetic susceptibility from MRI phase data may serve as a significant method for in vivo monitoring of changes in iron and myelin associated with normal, healthy aging, as well as neurological disease processes.

In this research, the cellular level underpinnings of the R_2^* and LFS signals were examined in a model rat brain system using 9.4 T MRI. The study was carried out using biophysical modeling and correlation with quantitative histology. For the first time, multiple biophysical modeling schemes were compared in both gray and white matter of excised rat brain tissue. Suprisingly, R_2^* dependence on tissue orientation has not been fully understood. Accordingly, scaling relations were derived for calculating the reversible, mesoscopic magnetic field component, R_2', of the apparent transverse relaxation rate from the orientation dependence in gray and white matter. Our results demonstrate that the orientation dependence of R_2^* and LFS in both white and cortical gray matter has a sinusoidal dependence on tissue orientation and a linear dependence on the volume fraction of myelin in the tissue.

A susceptibility processing pipeline was also developed and applied to the calculation of phase-combined LFS and QS maps. The processing pipeline was subsequently used to monitor myelin and iron changes in multiple sclerosis (MS) patients compared to healthy, age and gender-matched controls. With the use of QS and R_2^* mapping, evidence of statistically significant increases in iron deposition in sub-cortical gray matter, as well as myelin degeneration along the white matter skeleton, were identified in MS patients. The magnetic susceptibility-based MRI methods were then employed as potential clinical biomarkers for disease severity monitoring of MS. It was demonstrated that the combined use of R_2^* and QS, obtained from multi-echo gradient echo MRI, could serve as an improved metric for monitoring both gray and white matter changes in early MS.

Keywords

myelin, iron, quantitative susceptibility mapping, apparent transverse relaxation rate

Acknowledgements

The research documented in this study would not have been possible without the exceptional guidance, support and encouragement of a few key people. First and foremost, I would like to thank my supervisor, Dr. Ravi Menon. His insistence on precision, clarity and rigorous research standards remains an enduring influence. Ravi's insightful suggestions and knowlegeable mentoring have been particularly invaluable. He has been an exceptional role model.

I also wish to thank Joe Gati for his continual encouragement and good-natured advice during my work at the Center for Functional and Metabolic Mapping. As well, I am particularly indebted to my advisory committee members, Dr. Charles McKenzie and Dr. Tamie Poepping. They were always available, provided supportive insights and shared their professional expertise during committee meetings.

I am especially grateful to Dr. Marcelo Kremenchutzky for his expert clinical guidance during my observership sessions at the London Multiple Sclerosis Clinic. His clear, concise medical diagnoses, coupled with the extensive time he spent talking with patients, were truly exemplary. Jennifer Moussa, clinical coordinator for Dr. Kremenchutzky, was indispensable in helping me navigate the organization and ethics associated with the 7T MS clinical study.

My experience as a graduate student in the Medical Physics program at the University of Western Ontario has been incredibly rewarding thanks to the stimulating work, supportive relationships and shared challenges with fellow grad students and co-workers at the Robarts Research Institute. Andrew Curtis was a great friend and cohort throughout my time at Robarts. Our thoughtful discussions about research in particular and life in general helped place things in proper perspective. I would also like to thank Igor Solovey, a software engineer in our group. His assistance with the processing pipeline facilitated some of the reconstructions outlined in this thesis.

Most of all, though, I would like to thank both my fiancé, Sonali, and my wonderful family for their constant understanding, unconditional support and ongoing guidance throughout my PhD journey.

Co-Authorship Statement

The contributions of the authors to each of the manuscripts documented in this thesis are outlined below:

Mr. David Rudko, in the capacity of doctoral candidate, outlined the objectives, developed the methodology, conducted the experiments, acquired and analyzed the data, and developed the software employed for data analysis. He also wrote and prepared the manuscripts for publication. Dr. Martyn Klassen, in the capacity of co-author for the first manuscript (presented in Chapter 4), assisted the primary author in data analysis. Ms. Sonali de Chickera, in the capacity of co-author for the first manuscript, prepared, sectioned, and stained tissue sections for histological analysis. She also assisted in generating figures for publication. Mr. Greg Dekaban, in the capacity of co-author for the first manuscript, contributed histological staining reagents and helped with editing.

Dr. Marcelo Kremenchutzky, in the capacity of co-author of the second manuscript (presented in Chapter 5), assisted in protocol planning for the 7 T MS study. He is listed as a principal investigator for the human ethics protocol associated with this study. Mr. Joseph Gati, in the capacity of co-author for both manuscripts, assisted with scan protocol development. Dr. Ravi Menon, the candidate's supervisor and co-author of both manuscripts, provided guidance, mentorship, and supervision for both projects. He is also listed as a principal investigator for the human ethics protocol used in the 7 T MS study.

Table of Contents

List of Tables

List of Figures

List of Appendices

List of Abbreviations and Symbols

ΔB	magnetic field shift
CIS	clinically isolated syndrome
CNS	central nervous system
EDSS	extended disability status scale
f_{ext}	external/background Larmor frequency shift
f_{int}	internal/local, tissue-specific Larmor frequency shift
f_{tot}	total Larmor frequency shift integrated over the imaging volume
f_L	local (Larmor) frequency shift
GM	gray matter
GRE	gradient recalled echo
LFS	local (Larmor) frequency shift
MS	multiple sclerosis
OD	optical density
qMRI	quantitative magnetic resonance imaging
QSM	quantitative susceptibility mapping
R_2	transverse relaxation rate
R_2^*	effective transverse relaxation rate
R_2'	reversible component of the effective transverse relaxation rate
ROI	region of interest
RRMS	relapsing-remitting multiple sclerosis
SNR	signal-to-noise ratio
T_1	longitudinal relaxation rate
T_2	transverse relaxation rate
TE	echo time
TR	repetition time
UHF	ultra-high field
WM	white matter
θ	image phase
γ	gyromagnetic ratio

Scope of Thesis

The following is a brief overview of each chapter contained in this thesis. Chapter One introduces the principles, methodologies and relevance of the research studies composing the thesis. The second chapter discusses the underlying background of MRI physics, signal acquisition and phase processing necessary for understanding relaxometry and susceptibility mapping. A processing pipeline for multi-echo, gradient echo-based quantification of tissue magnetic properties (R_2^*, LFS, and $\Delta\chi$) is then examined in the third chapter.

Chapter Four derives from a manuscript published in the Proceedings of the National Academy of Sciences of the United States of America (Rudko et al., PNAS, Jan 7, 2014, 111(1), E159-167). It presents a fundamental research study utilizing combined R_2^*, LFS and QS mapping with multi-echo, gradient echo MRI at high field and ultra-high resolution. Multiple biophysical modeling schemes are compared for the first time in both gray and white matter for excised rat brain tissue.

Chapter Five derives from a manuscript accepted for publication in the journal, Radiology (Rudko et al., Radiology, manuscript #RAD-13-2475). It highlights a 7 T imaging study using whole-brain, quantitative $\Delta\chi$ and R_2^* mapping for simultaneous monitoring of iron deposition and demyelinating processes in MS patients. For the first time, voxel based morphometry is combined with generalized linear model (GLM) analysis to identify whole brain differences between patients and controls. The sixth and final chapter briefly summarizes the research carried out for this thesis. It also suggests ways of extending this research, with an emphasis on both technical developments and clinical applications.

Chapter 1

Introduction

The Prize is the pleasure of finding things out.

– Richard Feynman, *Quantum Man*

Over the last four decades, magnetic resonance imaging (MRI) has made dramatic progress as a non-invasive imaging modality for evaluating human tissue properties. Advanced technological breakthroughs in MRI now enable more accurate assessment of both the structure and function of many human organ systems. Not only is MRI being used to diagnose a wide range of disease processes, it is also being applied to such diverse research areas as the study of heart valve abnormalities (1), functional brain activation (2) and autoimmune cell tracking (3).

Fundamentally, MRI uses a strong external magnetic field to generate a bulk magnetization in the hydrogen nuclei of the human body. When these nuclei are excited by a radiofrequency (RF) pulse, an MR signal can be detected by a receiver coil. By adding spatially-varying, linear magnetic field gradients, images can then be reconstructed which represent the radiofrequency signal emitted from tissues (4). For standard MRI techniques at clinical field strengths of 1.5 and 3 Tesla (T), the radiofrequency signal is primarily a measure of the nuclear magnetization properties of water protons. However, in ultra-high field MRI (UHF MRI, $B_0 \geq 7$ T), the interaction between the external magnetic field and the orbital electrons in biological molecules also leads to an appreciable increase in the *Larmor resonance frequency* experienced by water protons (5). This frequency perturbation can be related to the concentration of biomolecules (6-8) and serves as a useful, quantitative MRI (qMRI) biomarker.

In any MRI scan, the specific physical characteristics of tissue being visualized depend on how the magnetic field is modulated during the acquisition process (9). Since the acquisition consists of a repetitive cycle of varying magnetic field gradients and RF pulses, the tissue magnetization undergoes a concomitant series of repetitive changes. Essentially, the magnetization is perturbed from its natural state and then allowed to recover to equilibrium through a process known as relaxation. This process provides the basic contrast in MRI. The differential relaxation rates of tissues result in relative signal differences observed in an image (10). In the section that follows, the sensitization of the MRI signal to different tissue relaxation properties is outlined in more detail and related to qMRI – a significant topic of discussion in this thesis.

1.1 Sensitizing the MRI signal to tissue properties

A pivotal improvement of MRI compared to other diagnostic imaging techniques such as x-ray computed tomography (CT), positron emission tomography (PET), ultrasound and optical imaging, is its ability to sensitize the signal to different properties of biological tissue (10). The MRI signal is flexible enough to reflect such biophysical quantities as tissue-specific nuclear relaxation rates (longitudinal relaxation rate: T_1, transverse relaxation rate: T_2, or effective transverse relaxation rate: T_2^*), rate of blood flow (11), blood oxygenation (12), water molecule self-diffusion (13), as well as tissue magnetic and electrical properties (7, 14).

The T_1 or T_2–weighted contrast obtained in standard MRI methods is controlled through the adjustment of pulse sequence timing parameters such as the duration between successive radiofrequency (RF) pulses, or the flip angle of these pulses. This, in turn, results in qualitative differences in signal intensity. For example, with an external magnetic field strength of 3 T, if contrast between gray and white matter in the human brain is desired, one can exploit the differences in either T_1 (white matter = 1100 ms, gray matter = 1800 ms) or T_2 (white matter = 70 ms , cortical gray matter = 100 ms) relaxation characteristics of brain tissue (15).

Because of its flexibility in generating contrast, MRI is used clinically by radiologists to confirm many soft tissue neurological disorders. However, the standard T_1- and T_2-weighted images employed by radiologists do not provide true quantitative metrics of tissue composition. They only identify *relative* differences in nuclear relaxation properties (4). This is problematic when seeking to relate the MRI signal to underlying cellular-level changes associated with either disease or normal, healthy aging. To make MRI more predictive of underlying biology, qMRI methods have been developed. For a qMRI parameter to be effective, it must be (i) reproducible, (ii) accurate and (iii) specific to underlying cellular architecture (16). Reproducibility reflects the magnitude of random errors that occur from one scan session to the next. Generally, these should be significantly less than the natural variation of the qMRI parameter itself. Accuracy reflects how closely a measurement is to the true value. Specificity reflects how closely the change in the qMRI parameter reflects the change in biology of the tissue.

Two frequently employed qMRI techniques are T_1 and T_2 relaxometry (16). With these two methods, specific magnetic field gradients and RF pulse combinations are used to probe the relaxation of nuclear magnetization over time. A quantitative value of T_1 or T_2 can then be assigned to each location in the brain. Relaxometry has proven valuable in understanding such neurological conditions as cerebral edema (17), Alzheimer’s and multiple sclerosis (MS) (18). However, T_1 and T_2 relaxometry require long acquisition times and are usually not suitable for whole-brain imaging.

This thesis examines the use of three magnetic susceptibility-based qMRI parameters acquired using a time-efficient, multi-echo, gradient echo sequence: apparent transverse relaxation rate (R_2^*), local Larmor frequency shift (LFS) and volume magnetic susceptibility ($\Delta\chi$). In all computations, standard error analysis methods are employed to identify accuracy. In the following section, the susceptibility-based MRI parameters are described in further detail.

1.2 Ultra-High Field (UHF) MRI and its applications to susceptibility-induced contrast

Currently, MRI scanners at high ($\geq$ 3 T) and ultra high-field (UHF, $\geq$ 7 T) offer improved signal-to-noise ratio (SNR) and increased spatial resolution compared to standard clinical imaging at 1.5 T. UHF MRI allows visualization of smaller structures in the human brain, including cortical folding patterns (19) and venous vasculature organization (20). A further advantage of UHF MRI is its increased magnetic susceptibility contrast, particularly useful in functional MRI (fMRI) (21) and superparamagnetic iron-oxide nano-particle (SPIO) tracking (22-24). Such applications employ the magnitude of the complex MRI signal but disregard the phase. Recently however, it has been demonstrated that with proper processing, the contrast observed in the MRI phase is sensitive to relative concentration differences of such important biological substrates as myelin and iron (6, 25).

When the human body is exposed to a strong external magnetic field, small differences in magnetic susceptibility between neighbouring tissues result in perturbations of the local magnetic field (26). These perturbations give rise to a detectable shift in the LFS, which is measurable through the complex image phase. Notably, the linear increase in magnetic susceptibility-induced field perturbations in UHF MRI results in higher signal-to-noise ratio (SNR) and improved contrast at higher B_0 fields for phase imaging (27). Once the image phase has been unwrapped and background magnetic field contributions have been removed, an estimate of tissue specific magnetic susceptibility properties may be computed (7, 28, 29). The magnetic susceptibility is calculated through a field-to-source inverse problem known as Quantitative Susceptibility Mapping (QSM), which reveals anatomical features in the brain with unprecedented quality. QSM also allows quantitative characterization of deep gray matter structures (7, 30), brain tumours (31) , and sub-cortical iron increases in MS (32).

Presently, the clinical applicability of QSM is hampered by challenges associated with proper phase processing and interpretation of the QS signal (7). Numerical instabilities in the field-to-source inverse calculation can result in streaking or blurring artifacts which complicate quantitation (33). As well, the quality of QS maps critically depends on the accuracy of the measured image phase. Incorrect phase values due to blood flow, low SNR, or incomplete/inaccurate phase unwrapping produce significant non-local artifacts (6). Several solutions to these issues are addressed in this thesis, as well as the application of QSM in conjunction with R_2^* mapping to underlying tissue biology. Additionally, the clinical applicability for MS monitoring using combined whole-brain QS and R_2^* maps is described for the first time.

1.3 Application of UHF MRI to multiple sclerosis

UHF, susceptibility-based MRI of multiple sclerosis constitutes one of the major chapters in this thesis. Accordingly, a brief overview follows of (i) the clinical symptoms and pathophysiology of MS and (ii) the clinical monitoring of MS using UHF MRI.

1.3.1 Clinical symptoms and pathophysiology of MS

MS is a chronic, inflammatory disease of the central nervous system (CNS) characterized by a varied and unpredictable time course (34). It is the most common neurological disease affecting young adults in Canada (35, 36). Although the specific cause is unknown, it appears to involve both genetic susceptibility and triggers such as a virus, a dysregulated metabolism or environmental factors (37, 38). In most patients, MS consists of initial episodes of reversible neurological deficit followed by progressive deterioration, which can become severe and result in early death (34). Evolution of the disease produces a spectrum of clinical features that may include motor weakness, sensory and gait disturbances, vision loss and cognitive changes (34).

Several MS disease sub-types have been characterized. These are determined on the basis of such clinical criteria as frequency of relapses, time to disease progression, and lesion development (39). The major MS sub-types include: relapsing-remitting MS (RRMS, approximately 85% of cases), primary progressive MS (PPMS, approximately 10% of cases) and progressive-relapsing MS (PRMS, about 5% of cases) (34). RRMS is characterized by unpredictable relapses followed by months to years of remission. A fourth major sub-type, secondary progressive MS (SPMS), occurs for approximately 65% of those with initial RRMS and is defined by a progressive neurologic decline between attacks without definite periods of remission (34). After initial symptoms, PPMS patients experience no remission and symptoms steadily worsen (34). PPMS patients have steady neurologic decline from the onset, superimposed with attacks (34, 39).

The hallmark pathophysiology of MS is damage to myelin, axons and oligodendrocytes (37). This occurs through a multistep mechanism involving sequential inflammation, demyelination and neurodegeneration (34). The specific autoimmune targets are believed to be cellular components of the CNS normally inaccessible due to their location behind the blood–brain barrier. During disease initiation, entry of autoimmune cells (T-cells, B-cells and monocytes) through the blood brain barrier is triggered by cytokine and chemokine signals (37). Once within the CNS, T-cells are stimulated and retained there by resident microglia, which present antigen receptor sites to the T-cells. Microglia are also involved in clearing away myelin debris. This results in further T-cell/lymphocyte infiltration (34). Concurrent with the initial autoimmune response, the inflammatory infiltrate in white matter lesions eventually includes macrophages at the lesion centre. These are principally responsible for myelin digestion (37, 38).

The trigger for the T-cell mediated autoimmune attack in MS is unclear. However, it is recognized that MS consists of repeated attacks on both myelin and oligodendrocytes via an inflammatory cascade activated repeatedly over time. The existing knowledge of the interconnected cellular components in the cascade has already been used to create targeted therapies aimed at reducing progression (37, 40). From an MRI standpoint, targeted imaging of these cellular components utilizing, for example, iron-labeled cellular MRI (23), represents a promising avenue for monitoring critical components in the MS immune response.

1.3.2 UHF MRI of MS

Conventional MRI employing standard T_1- and T_2-weighted imaging plays a key role in diagnosing MS (41). However, neither lesion load or lesion volume derived from these standard sequences have correlated well with clinical symptoms and scoring scales (42). In addition, standard MRI findings have not demonstrated significant predictive power for identifying disease progression (39). Post-mortem histopathology has revealed the inability of standard MRI to visualize no more than a subset of the actual lesions and damage (43).

Standard MRI pulse sequences used for monitoring MS, such as T_2-weighted fast spin echo (FSE) and fluid-attenuated inversion recovery (FLAIR), visualize only two-thirds of histopathologically detectable white matter (WM) lesions and less than one-tenth of cortical grey matter (GM) lesions (44). Moreover, the standard sequences are insensitive to damage in normal-appearing white matter, which is known to have a significant role in the onset of MS (45, 46). In contrast, susceptibility-based UHF MRI techniques, including the LFS and QS mapping methods detailed in this thesis, potentially offer more accurate visualization of early myelin changes in gray and white matter not visualized on standard MRI contrasts (6, 7). This is because QSM measures both the nuclear magnetization and the accompanying magnetic susceptibility in an imaging voxel (47). In white matter, these physical parameters are specific to the composition of myelin, since myelin is magnetized by an amount proportional to the magnetic susceptibility of phospholipid molecules in the myelin bilayers. Consequently, by using UHF MRI, QSM detects an *intrinsic property* that may be more closely linked to demyelination than such other methods as T_2-based relaxometry or diffusion MRI measurements of fractional anisotropy.

Equally significant, depicting MS gray matter pathology using MRI directly relates to how clinicians deliver treatment. For example, the identification of gray matter damage may serve as an improved biomarker for MS monitoring (48). Indeed, UHF T_2^*–weighted MRI using 2D gradient echo imaging has already demonstrated an improved sensitivity for detecting gray matter lesions in vivo at 7 T (48). T_2^*–weighted MRI has also been used to monitor the accumulation of non-haeme iron in sub-cortical gray matter (30, 32, 49). Iron in sub-cortical gray matter is essential for normal neuronal metabolism, including mitochondrial energy generation and myelination. However, excessive levels may exert oxidative stress and result in cell death. When excess iron is present, incomplete chelation or storage results in iron catalyzing the production of hydroxyl radicals. The production of such radicals may trigger protein denaturation, damage to DNA or oxidation of phospholipid membranes (50). As result, monitoring the accumulation of non-haeme iron in the basal ganglia and linking this to clinical disability is a major area of interest in UHF MRI of MS. It is a primary focus in the fifth chapter of this thesis.

Several qMRI metrics, including T_2, T_2^*, magnetic field correlation (MFC) and QSM have been proposed for monitoring basal ganglia iron *in vivo*. In this thesis, two of these metrics, T_2^* and QSM, are examined. Recent research has demonstrated that the apparent transverse relaxation rate ($R_2^* = 1/\ T_2^*$) correlates well with basal ganglia iron (27). Regional values of R_2^* differ significantly between CIS patients (n = 32) and MS patients (n = 37) (51). This suggests R_2^* relaxometry may be a useful tool for evaluating differential iron deposition between MS disease groups. Further, it may prove helpful for clarifying whether regional iron accumulation contributes to MS pathology or merely reflects an epiphenomenon.

Recently, QSM has demonstrated an increased sensitivity to changes in iron associated with normal aging (52) and MS (32) in basal ganglia structures compared to R_2^*. This increased sensitivity results from the ability of QS to measure the mean magnetic field perturbation in a voxel, as opposed to the signal relaxation of protons in water molecules (25). The mean magnetic field perturbation can then be directly linked to the amount of iron (52). However, relaxometric measures such as R_2^* are not specific to the mean magnetic field. Rather, they measure the effect of intra-voxel susceptibility *gradients* on phase dispersion of relaxing protons (53). In this thesis, the relative sensitivities of R_2^* and QS to iron accumulation in MS are evaluated as clinically relevant biomarkers.

The second chapter examines the underlying background of MRI physics, signal acquisition and phase processing necessary for understanding relaxometry and susceptibility mapping. For a complete overview of all chapters, refer to the ‘Scope of Thesis’ section on page xvii.

1.4 References

1. Masci, P. G., S. Dymarkowski, and J. Bogaert. 2008. Valvular heart disease: what does cardiovascular MRI add? *Eur Radiol* 18: 197-208.
2. Matthews, P. M., and P. Jezzard. 2004. Functional magnetic resonance imaging. *Journal of Neurology, Neurosurgery & Psychiatry* 75: 6-12.
3. Bonetto, F., M. Srinivas, A. Heerschap, R. Mailliard, E. T. Ahrens, C. G. Figdor, and I. J. de Vries. 2011. A novel (19)F agent for detection and quantification of human dendritic cells using magnetic resonance imaging. *Int J Cancer* 129: 365-373.
4. Haacke, E. M., R. W. Brown, M. R. Thompson, and R. Venkatesan. 1999. *Magnetic resonance imaging: physical principles and sequence design*. Wiley-Liss New York:
5. Lee, J., K. Shmueli, M. Fukunaga, P. van Gelderen, H. Merkle, A. C. Silva, and J. H. Duyn. 2010. Sensitivity of MRI resonance frequency to the orientation of brain tissue microstructure. *Proc Natl Acad Sci U S A* 107: 5130-5135.
6. Schweser, F., K. Sommer, A. Deistung, and J. R. Reichenbach. 2012. Quantitative susceptibility mapping for investigating subtle susceptibility variations in the human brain. *Neuroimage* 62: 2083-2100.
7. Schweser, F., A. Deistung, B. W. Lehr, and J. R. Reichenbach. 2011. Quantitative imaging of intrinsic magnetic tissue properties using MRI signal phase: an approach to in vivo brain iron metabolism? *Neuroimage* 54: 2789-2807.
8. Liu, C., W. Li, G. A. Johnson, and B. Wu. 2011. High-field (9.4 T) MRI of brain dysmyelination by quantitative mapping of magnetic susceptibility. *Neuroimage* 56: 930-938.
9. Lufkin, R., W. L. Davis, and A. G. Osborn. 1993. Overview of MR imaging modalities. *J Comput Assist Tomogr* 17 Suppl 1: S24-9.
10. Plewes, D. B., and W. Kucharczyk. 2012. Physics of MRI: a primer. *J Magn Reson Imaging* 35: 1038-1054.
11. Calamante, F., D. L. Thomas, G. S. Pell, J. Wiersma, and R. Turner. 1999. Measuring cerebral blood flow using magnetic resonance imaging techniques. *J Cereb Blood Flow Metab* 19: 701-735.

12. Ogawa, S., T. M. Lee, A. R. Kay, and D. W. Tank. 1990. Brain magnetic resonance imaging with contrast dependent on blood oxygenation. *Proc Natl Acad Sci U S A* 87: 9868-9872.
13. Basser, P. J., and D. K. Jones. 2002. Diffusion-tensor MRI: theory, experimental design and data analysis - a technical review. *NMR Biomed* 15: 456-467.
14. Tuch, D. S., V. J. Wedeen, A. M. Dale, J. S. George, and J. W. Belliveau. 2001. Conductivity tensor mapping of the human brain using diffusion tensor MRI. *Proceedings of the National Academy of Sciences* 98: 11697-11701.
15. Stanisz, G. J., E. E. Odrobina, J. Pun, M. Escaravage, S. J. Graham, M. J. Bronskill, and R. M. Henkelman. 2005. T1, T2 relaxation and magnetization transfer in tissue at 3T. *Magn Reson Med* 54: 507-512.
16. Tofts, P. S., and E. P. G. H. Du Boulay. 1990. Towards quantitative measurements of relaxation times and other parameters in the brain. *Neuroradiology* 32: 407-415.
17. Barnes, D., W. I. McDonald, G. Johnson, P. S. Tofts, and D. N. Landon. 1987. Quantitative nuclear magnetic resonance imaging: characterisation of experimental cerebral oedema. *Journal of Neurology, Neurosurgery & Psychiatry* 50: 125-133.
18. Kidd, D., G. J. Barker, P. S. Tofts, A. Gass, A. J. Thompson, W. I. McDonald, and D. H. Miller. 1997. The transverse magnetisation decay characteristics of longstanding lesions and normal-appearing white matter in multiple sclerosis. *Journal of neurology* 244: 125-130.
19. Fischl, B. 2012. FreeSurfer. *Neuroimage* 62: 774-781.
20. Budde, J., G. Shajan, J. Hoffmann, K. Ugurbil, and R. Pohmann. 2011. Human imaging at 9.4 T using T(2) *-, phase-, and susceptibility-weighted contrast. *Magn Reson Med* 65: 544-550.
21. Geissler, A., F. P. Fischmeister, G. Grabner, M. Wurnig, J. Rath, T. Foki, E. Matt, S. Trattnig, R. Beisteiner, and S. D. Robinson. 2013. Comparing the Microvascular Specificity of the 3- and 7-T BOLD Response Using ICA and Susceptibility-Weighted Imaging. *Front Hum Neurosci* 7: 474.
22. Modo, M., M. Hoehn, and J. W. Bulte. 2004. Cellular MR imaging. *Molecular imaging* 4: 143-164.

23. Rad, A. M., A. S. Arbab, A. S. M. Iskander, Q. Jiang, and H. Soltanian-Zadeh. 2007. Quantification of superparamagnetic iron oxide (SPIO)-labeled cells using MRI. *Journal of Magnetic Resonance Imaging* 26: 366-374.
24. Heyn, C., C. V. Bowen, B. K. Rutt, and P. J. Foster. 2005. Detection threshold of single SPIO-labeled cells with FIESTA. *Magnetic resonance in medicine* 53: 312-320.
25. Deistung, A., A. Schafer, F. Schweser, U. Biedermann, R. Turner, and J. R. Reichenbach. 2013. Toward in vivo histology: a comparison of quantitative susceptibility mapping (QSM) with magnitude-, phase-, and R2*-imaging at ultra-high magnetic field strength. *Neuroimage* 65: 299-314.
26. Schenck, J. F. 1996. The role of magnetic susceptibility in magnetic resonance imaging: MRI magnetic compatibility of the first and second kinds. *Medical physics* 23: 815.
27. Yao, B., T. Q. Li, P. Gelderen, K. Shmueli, J. A. de Zwart, and J. H. Duyn. 2009. Susceptibility contrast in high field MRI of human brain as a function of tissue iron content. *Neuroimage* 44: 1259-1266.
28. de Rochefort, L., R. Brown, M. R. Prince, and Y. Wang. 2008. Quantitative MR susceptibility mapping using piece-wise constant regularized inversion of the magnetic field. *Magn Reson Med* 60: 1003-1009.
29. de Rochefort, L., T. Liu, B. Kressler, J. Liu, P. Spincemaille, V. Lebon, J. Wu, and Y. Wang. 2010. Quantitative susceptibility map reconstruction from MR phase data using bayesian regularization: validation and application to brain imaging. *Magn Reson Med* 63: 194-206.
30. Lebel, R. M., A. Eissa, P. Seres, G. Blevins, and A. H. Wilman. 2012. Quantitative high-field imaging of sub-cortical gray matter in multiple sclerosis. *Mult Scler* 18: 433-441.
31. Deistung, A., F. Schweser, B. Wiestler, M. Abello, M. Roethke, F. Sahm, W. Wick, A. M. Nagel, S. Heiland, and H.-P. Schlemmer. 2013. Quantitative Susceptibility Mapping Differentiates between Blood Depositions and Calcifications in Patients with Glioblastoma. *PloS one* 8: e57924.

32. Langkammer, C., T. Liu, M. Khalil, C. Enzinger, M. Jehna, S. Fuchs, F. Fazekas, Y. Wang, and S. Ropele. 2013. Quantitative susceptibility mapping in multiple sclerosis. *Radiology* 267: 551-559.
33. Reichenbach, J. R. 2012. The future of susceptibility contrast for assessment of anatomy and function. *Neuroimage* 62: 1311-1315.
34. Compston, A., and A. Coles. 2008. Multiple sclerosis. *Lancet* 372: 1502-1517.
35. Poppe, A. Y., C. Wolfson, and B. Zhu. 2008. Prevalence of multiple sclerosis in Canada: a systematic review. *Can J Neurol Sci* 35: 593-601.
36. Beck, C. A., L. M. Metz, L. W. Svenson, and S. B. Patten. 2005. Regional variation of multiple sclerosis prevalence in Canada. *Mult Scler* 11: 516-519.
37. Ontaneda, D., M. Hyland, and J. A. Cohen. 2012. Multiple sclerosis: new insights in pathogenesis and novel therapeutics. *Annual Review of Medicine* 63: 389-404.
38. Sospedra, M., and R. Martin. 2005. Immunology of multiple sclerosis. *Annu Rev Immunol* 23: 683-747.
39. Ceccarelli, A., R. Bakshi, and M. Neema. 2012. MRI in multiple sclerosis: a review of the current literature. *Curr Opin Neurol* 25: 402-409.
40. Rice, C. M., K. Kemp, A. Wilkins, and N. J. Scolding. 2013. Cell therapy for multiple sclerosis: an evolving concept with implications for other neurodegenerative diseases. *Lancet* 382: 1204-1213.
41. Polman, C. H., S. C. Reingold, B. Banwell, M. Clanet, J. A. Cohen, M. Filippi, K. Fujihara, E. Havrdova, M. Hutchinson, and L. Kappos. 2011. Diagnostic criteria for multiple sclerosis: 2010 revisions to the McDonald criteria. *Annals of neurology* 69: 292-302.
42. Filippi, M., M. A. Rocca, N. De Stefano, C. Enzinger, E. Fisher, M. A. Horsfield, M. Inglese, D. Pelletier, and G. Comi. 2011. Magnetic resonance techniques in multiple sclerosis: the present and the future. *Arch Neurol* 68: 1514-1520.
43. Tardif, C. L., B. J. Bedell, S. F. Eskildsen, D. L. Collins, and G. B. Pike. 2012. Quantitative magnetic resonance imaging of cortical multiple sclerosis pathology. *Multiple sclerosis international* 2012:

44. Geurts, J. J., L. Bo, P. J. Pouwels, J. A. Castelijns, C. H. Polman, and F. Barkhof. 2005. Cortical lesions in multiple sclerosis: combined postmortem MR imaging and histopathology. *AJNR Am J Neuroradiol* 26: 572-577.
45. Rudick, R. A., J. C. Lee, K. Nakamura, and E. Fisher. 2009. Gray matter atrophy correlates with MS disability progression measured with MSFC but not EDSS. *J Neurol Sci* 282: 106-111.
46. Moraal, B., C. Pohl, B. M. Uitdehaag, C. H. Polman, G. Edan, M. S. Freedman, H. P. Hartung, L. Kappos, D. H. Miller, X. Montalban, V. Lanius, R. Sandbrink, and F. Barkhof. 2009. Magnetic resonance imaging predictors of conversion to multiple sclerosis in the BENEFIT study. *Arch Neurol* 66: 1345-1352.
47. Li, W., B. Wu, A. V. Avram, and C. Liu. 2012. Magnetic susceptibility anisotropy of human brain in vivo and its molecular underpinnings. *Neuroimage* 59: 2088-2097.
48. Mainero, C., T. Benner, A. Radding, A. van der Kouwe, R. Jensen, B. R. Rosen, and R. P. Kinkel. 2009. In vivo imaging of cortical pathology in multiple sclerosis using ultra-high field MRI. *Neurology* 73: 941-948.
49. Ropele, S., W. de Graaf, M. Khalil, M. P. Wattjes, C. Langkammer, M. A. Rocca, A. Rovira, J. Palace, F. Barkhof, M. Filippi, and F. Fazekas. 2011. MRI assessment of iron deposition in multiple sclerosis. *J Magn Reson Imaging* 34: 13-21.
50. Nunez, M. T., P. Urrutia, N. Mena, P. Aguirre, V. Tapia, and J. Salazar. 2012. Iron toxicity in neurodegeneration. *Biometals* 25: 761-776.
51. Khalil, M., C. Langkammer, S. Ropele, K. Petrovic, M. Wallner-Blazek, M. Loitfelder, M. Jehna, G. Bachmaier, R. Schmidt, C. Enzinger, S. Fuchs, and F. Fazekas. 2011. Determinants of brain iron in multiple sclerosis: a quantitative 3T MRI study. *Neurology* 77: 1691-1697.
52. Bilgic, B., A. Pfefferbaum, T. Rohlfing, E. V. Sullivan, and E. Adalsteinsson. 2012. MRI estimates of brain iron concentration in normal aging using quantitative susceptibility mapping. *Neuroimage* 59: 2625-2635.
53. Yablonskiy, D. A., and E. M. Haacke. 1994. Theory of NMR signal behavior in magnetically inhomogeneous tissues: the static dephasing regime. *Magn Reson Med* 32: 749-763.

Chapter 2

Underlying Sources of MRI Contrast and Signal Formation

I canna' change the laws of physics, Captain!
– Scottie, head engineer in *Star Trek*

To provide a brief background for the discussion of transverse relaxometry, LFS and QS mapping that follows, this chapter considers the fundamental sources of the MRI contrast and signal formation. It is partitioned into four sections. The first section describes the physics of MRI signal formation under the influence of a strong external magnetic field and radiofrequency (RF) pulse perturbations. The Bloch equations are then introduced as the mathematical model describing the time-evolution of the MRI signal. This is followed by a discussion of the basics of MR image reconstruction. Lastly, an introductory examination of susceptibility mapping provides a background for the phase processing pipeline presented in Chapter three.

2.1 Underlying sources of the MRI signal

In an external magnetic field such as the one produced by a superconducting MRI magnet, atomic nuclei can be treated as magnetic dipoles possessing a magnetic moment, μ, and an angular momentum, L. These two parameters are related accordingly (1):

$$\vec{\mu} = \gamma \vec{L} \qquad [2.1]$$

where γ is the gyromagnetic ratio which is specific to the nucleus of interest. The most common nucleus to be imaged in MRI is that of hydrogen bonded to oxygen in water. Hydrogen (H^1) has a gyromagnetic ratio of $\gamma = 267.51 \times 10^6$ radians/s/T and contains a single positively charged proton and a negatively charged electron bound by the Coulomb electromagnetic field (2). Under the influence of the external field of the MRI magnet, the proton experiences a torque (1),

$$\vec{T} = \vec{\mu} \times \vec{B} \qquad [2.2]$$

which can be related to the nuclear spin angular momentum by the equation (3):

$$\vec{T} = \frac{d\vec{L}}{dt} = \vec{\mu} \times \vec{B} \qquad [2.3]$$

Equation [2.3] describes the time evolution of the nuclear magnetization ($\vec{M}$) and forms the basis for the MRI Bloch equation - a first-order, linear differential equation describing the magnetization dynamics (3):

$$\frac{d\vec{M}}{dt} = \gamma \cdot \vec{M} \times \vec{B}_{ext} \qquad [2.4]$$

In equation [2.4], B_{ext} represents the combination of the static magnetic field and both the magnetic field gradients (G) and RF (B_1) fields (4):

$$\vec{B}_{ext} = B_0 \hat{k} + \gamma \vec{G} \cdot \vec{r} \hat{k} + B_{1x} \hat{i} + B_{1y} \hat{j} \qquad [2.5]$$

Typically, the Bloch equation is written with respect to a particular reference frame, the most familiar of which is the frame rotating in relation to the z-axis of the scanner coordinate system at the Larmor frequency. In this frame, the external magnetic field becomes (4):

$$\vec{B}_{rot} = \vec{B}_{ext} - B_0 \hat{k} = \gamma \vec{G} \cdot \vec{r} \hat{k} + B_{1x} \hat{i} + B_{1y} \hat{j} \qquad [2.6]$$

Evaluating the Bloch equations in this reference frame is equivalent to stopping the free precession of spins in order to isolate the dynamics of the magnetization caused by RF pulses and gradients. The rotating reference frame is described pictorially as follows:

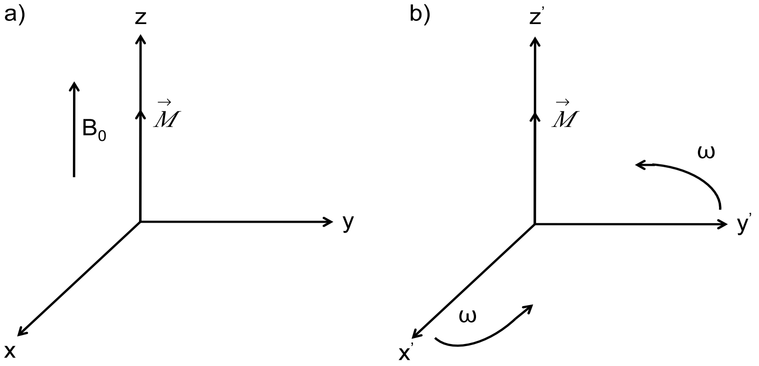

Figure 2.1: (a) Classical representation of the nuclear magnetization vector, aligned along the magnetic field in the static reference frame. (b) Schematic representation of the reference rotating about the z-axis at the Larmor resonance frequency, (ω), of on-resonant spins.

The primed coordinates (x′, y′ and z′) in figure 2.1 indicate the axes are rotating about the z-axis at the Larmor frequency. During an MRI experiment, for signal to be detected by a receiver coil, the magnetization vector must be rotated into the transverse (x′y′) plane (3). This is accomplished through the application of an RF pulse (B_1 field) which rotates the magnetization into the transverse plane by an angle $\theta = \gamma B_1 t$ (4):

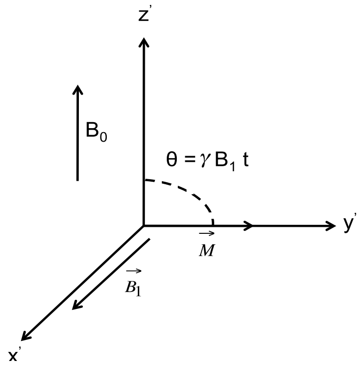

Figure 2.2: Application of an RF pulse with flip angle $\theta = \gamma B_1 t$ along the x′-axis. For such an RF-pulse the magnetization vector, **M**, is rotated down along the y′-axis.

For modeling any real MRI experiment, this simplified pictorial description must be extended further to include the effects of magnetic fields produced by nuclear spins whose Larmor frequency is different from that of water (off-resonance spins) (1, 3). The magnetic field of these off-resonance spins, B_{off}, is not rotated into the transverse plane but does result in spins experiencing an effective field (B_e) which is the vector sum of B_{off} and B_1 (4). This concept is illustrated below:

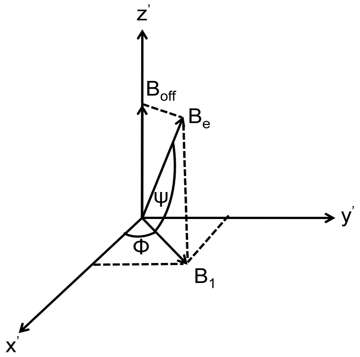

Figure 2.3: Schematic representation of the magnetic field vectors applied in the rotating frame of reference (x′, y′, z′). The B_1 magnetic field is applied at an angle ϕ relative to the x′-axis. Due to the presence of the magnetic field generated by off-resonance spins (B_{off}), the nuclear magnetization precesses around the effective magnetic field, B_e, rather than the B_1 field (1, 4, 5). The effective magnetic field is rotated away from the transverse plane by an angle ψ.

Under the additional influence of T_1 and T_2 relaxation, the Bloch equation describing the dynamics of the magnetization vector can be re-written as (6-8):

$$\frac{d\vec{M}}{dt} = \gamma \cdot \vec{M} \times \vec{B}_{rot} + \frac{M_0 - M_z}{T_1} + \frac{M_{xy}}{T_2} \qquad [2.7]$$

The first term on the right hand side of equation [2.7] accounts for the free precession of nuclei in the external magnetic field, as well as the effects of RF and gradient pulses. The second and third terms account for longitudinal recovery (T_1) and transverse decay (T_2)

respectively (8, 9). Equation [2.7] provides a phenomenological model of MRI spin precession and can be used to simulate the effects of an MRI pulse sequence numerically (10, 11). This is performed by inputting realistic values of T_1, T_2 and proton density and using standard numerical methods to express equation [2.7] in matrix form as follows:

$$\begin{bmatrix}\dot{M}_x\\ \dot{M}_y\\ \dot{M}_z\end{bmatrix} = \begin{bmatrix}0 & -\gamma\vec{G}\cdot\vec{r} & -\gamma B_{1xy}\cdot y\\ -\gamma\vec{G}\cdot\vec{r} & 0 & \gamma B_{1xy}\cdot x\\ \gamma B_{1xy}\cdot y & -\gamma B_{1xy}\cdot x & 0\end{bmatrix}\begin{bmatrix}M_x\\ M_y\\ M_z\end{bmatrix} + \begin{bmatrix}-1/T_2 & 0 & 0\\ 0 & -1/T_2 & 0\\ 0 & 0 & -1/T_1\end{bmatrix}\begin{bmatrix}M_x\\ M_y\\ M_z\end{bmatrix} + \begin{bmatrix}0\\ 0\\ -1/T_1\end{bmatrix}M_0 \qquad [2.8]$$

Equation [2.8], in discretized form, can be solved repeatedly for each repetition period in an MRI sequence by using a numerical simulation. Understanding the time-dependent changes in the nuclear magnetization vector plays a significant role in modeling the changes in both the magnitude and phase signal from white and gray matter in the brain – a major topic of discussion in this thesis.

2.2 Signal detection and Fourier domain representation of the MR imaging experiment

After the application of the RF pulse, the nuclear magnetization will precess in the transverse plane. The resultant time-varying magnetic field produced by the precessing magnetization generates a current in a receiver coil located in the vicinity of the sample. This current forms the basis for the MR image (3, 5). To more thoroughly understand this concept, consider the Fourier relationship between the time-varying current in the coil, *s(t)*, and the Larmor resonance frequency, ω, of nuclei:

$$S(\omega) = \int_{-\infty}^{\infty} s(t)\, e^{2\pi i\omega t}\, dt \qquad [2.9]$$

For the hypothetical case of a sample consisting of only pure water, ignoring the effects of nuclear relaxation, the Fourier relationship between the time-domain and Fourier domain signals can be visualized as follows:

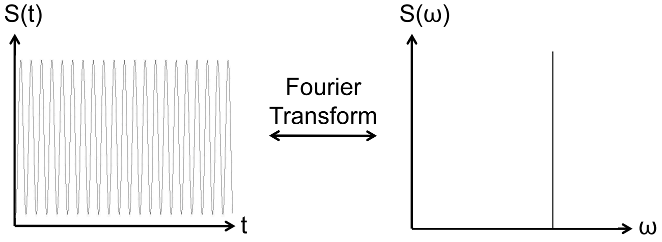

Figure 2.4: Ideal representation of the NMR signal for a sample containing pure water without T_2-relaxation.

The signal in the time domain oscillates at the Larmor frequency, while the corresponding frequency domain spectrum shows a peak at the Larmor frequency (5). In MRI of tissues in the human body, however, multiple chemical compounds exist in a single volume element (voxel) of the image. Each compound experiences a slightly different local magnetic field, resulting in a modified Fourier domain representation (9) that contains a spectrum of signals:

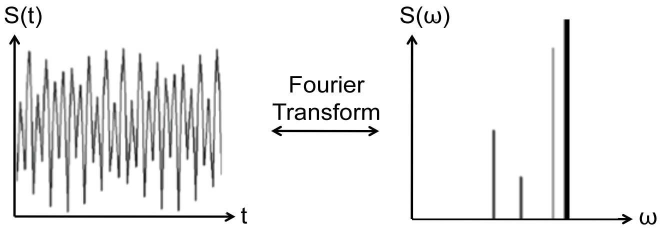

Figure 2.5: Representation of the NMR signal for a sample containing compounds whose protons experience different local magnetic fields (magnetic environments) without T_2-relaxation. The signal in the time domain is a composite sinusoid that oscillates at a frequency that is the sum of the frequencies of the nuclei in different chemical environments in the sample (3). The corresponding frequency domain spectrum displays multiple peaks – each of which represents a specific proton in a particular magnetic environment.

Furthermore, during any standard MRI pulse sequence, T_2-based nuclear relaxation occurs (1, 12), resulting in an exponential decay of the signal, S(t). Here the variable "t" denotes the time after the RF pulse. The exponential decay of the signal in the time domain corresponds to a line-broadening of the signal in the Fourier domain (1) as illustrated below:

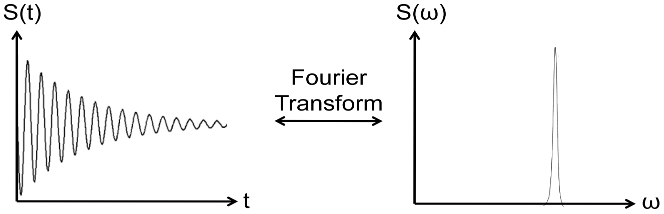

Figure 2.6: NMR signal for a sample of pure water subject to T_2-relaxation. This results in exponential decay of the time domain signal, S(t). The line shape of the frequency domain signal is broadened due to the exponential T_2-decay process. In the simplified representation above, the contributions of multiple resonating species with different Larmor frequencies are neglected.

To spatially discriminate the frequency domain signal, S(ω), at one voxel from other voxels in an image, MRI employs linear, magnetic field gradients to modulate the amplitude of the main magnetic field (1, 12, 13). Linear modulation of the main magnetic field (B_0) enables the assignment of a unique resonance frequency to each location in the image space. The magnetic gradient field, *G*, is generated by a current carrying wire wound into a solenoid which produces a linear magnetic field variation along the direction of the main field according to the following equation:

$$\vec{G} = \frac{\partial B_z}{\partial x}\hat{x} + \frac{\partial B_z}{\partial y}\hat{y} + \frac{\partial B_z}{\partial z}\hat{z} \qquad [2.10]$$

The application of this gradient results in the Larmor resonance frequency of spins becoming proportional to their spatial location:

$$\omega(\vec{r}) = \gamma B(\vec{r}) = \gamma(B_0 + \vec{G} \cdot \vec{r}) \qquad [2.11]$$

Through the linear relationship in equation [2.11] the desired amplitude of the gradient field, G, can be calculated for a particular pulse bandwidth, with Δω representing the range of frequencies excited by the RF pulse (1, 5, 13). For instance, for a gradient amplitude of G_z and a desired slice thickness, ΔZ , the relationship between the spatial location of a slice and its Larmor frequency is depicted as follows:

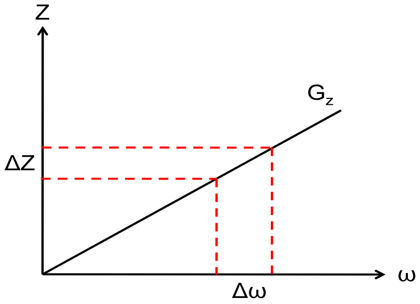

Figure 2.7: Linear relationship between z-dimension slice thickness (ΔZ) of an MRI pulse sequence and the bandwidth of the RF pulse (Δω).

The MRI signal detected at a time "t" after the radiofrequency excitation pulse in the presence of an imaging gradient is then related to the nuclear spin density by the following Fourier relationship (12):

$$S(t) = \int_{-\infty}^{\infty} \rho(\vec{r})\, e^{i\omega(\vec{r})t} d\vec{r} \qquad [2.12]$$

where $\rho(\vec{r})$ represents the spin density of nuclei at a particular location. In the rotating reference frame, where the Larmor frequency is removed from the signal, equation [2.12] is expressed as:

$$S(t) = \int_{-\infty}^{\infty} \rho(\vec{r})\, e^{i\gamma G \vec{r}\, t} d\vec{r} \qquad [2.13]$$

To express this equation in more compact form, the relationship in equation [2.13] can be

simplified (1, 5). The following change of variables is customary:

$$k = \frac{1}{2\pi}\gamma G\, t \qquad [2.14]$$

which, for the case of temporally-varying gradient waveforms, becomes:

$$k = \frac{1}{2\pi}\gamma \int_{0}^{t} G(t')\, dt' \qquad [2.15]$$

where equation [2.15] defines the signal in the spatial frequency domain (often referred to as k-space in MRI). The spatial frequency domain signal is related to the spin density (ρ(r)), which is the variable of interest in MRI, through the inverse Fourier transform operation:

$$\rho(\vec{r}) = \int_{-\infty}^{\infty} s(\vec{k}) e^{-2\pi i \vec{k}\cdot\vec{r}}\, d\vec{k} \qquad [2.16]$$

From equation [2.16], it is clear that the relationship between the frequency domain signal and MRI and the spatial domain spin density is through use of the inverse Fourier transform. This relationship is represented schematically below:

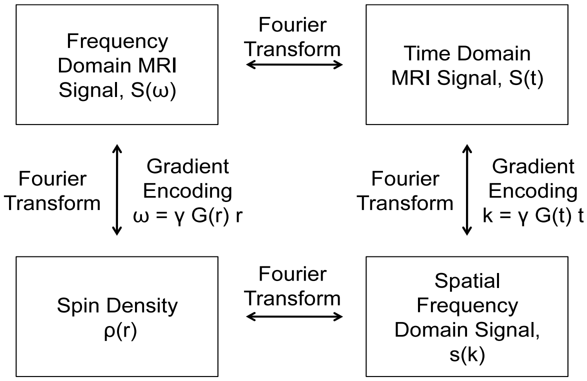

Figure 2.8: Fourier relationships between the frequency domain signal and the image space signal in MRI.

The position at each point in k-space is related to the degree of image contrast variation at a particular frequency (12). The center-most regions of k-space contain information about the low spatial frequency components of the image. The outer-most regions of k-space contain information about the high spatial frequency components of the image.

2.3 Gradient recalled echo imaging and T_2^* contrast

Gradient recalled echo (GRE) imaging is the preferred method for acquiring complex, T_2^*-weighted data used to isolate the image phase for LFS and QS mapping (14, 15). GRE methods encompass a relatively large class of MRI pulse sequences that do not use spin echoes (16). They include gradient-spoiled, RF-spoiled and balanced steady-state free precession (bSSFP) sequences (17). A standard, gradient-spoiled GRE sequence typically consists of an RF excitation, followed by imaging gradients and data acquisition. The sequence is repeated many times to acquire a full imaging volume.

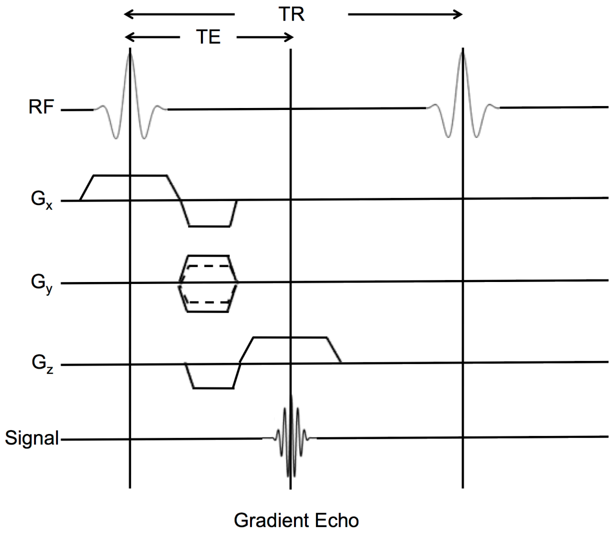

Figure 2.9: Pulse sequence diagram illustrating a typical gradient echo imaging sequence used in susceptibility mapping at UHF.

In figure 2.9, the echo time (TE) represents the time between the RF excitation and the middle of the readout gradient. The value of TE, along with the repetition interval (TR), flip angle and spoiling method, all influence the signal in a GRE sequence. The contrast is also influenced by the T_1, T_2 and T_2^* properties of the tissue (17). For example, when the TR period is reduced below approximately 2 × T_1, the spins do not regain complete longitudinal magnetization following the excitation pulse and a steady-state magnetization is reached (14, 18). In such a steady-state, the regrowth of the longitudinal magnetization is in equilibrium with the reduction in this magnetization caused by the RF pulse.

If GRE imaging is preferentially sensitized to the T_2^* relaxation rate ($R_2^* = 1/T_2^*$), an image is obtained which is dominated by two parameters:(i) the rate of apparent signal decay in an imaging voxel produced by spin-spin ($R_2 = 1/T_2$) dephasing of the transverse magnetization (M_{xy}) and (ii) local magnetic field inhomogeneities ($R_2' = 1/T_2'$) (19).

$$R_2^* = R_2 + R_2' \qquad [2.17]$$

Mathematically, the influence of R_2^* on the time-dependent MRI signal, *S(t)*, in a GRE experiment can be understood using the static dephasing regime theory (20). In this regime, self-diffusion of water molecules is neglected and the MRI signal, normalized to the voxel volume, is given by:

$$S(t) = \frac{1}{V} \cdot \rho \cdot \int_{V_0} d\vec{r} \cdot \exp(-t \cdot R_2(\vec{r})) \cdot \exp(-i \cdot \omega(\vec{r}) \cdot t) \qquad [2.18]$$

where ρ represents the combined effects of spin density, receiver coil sensitivity and RF excitation efficiency. The $\exp(-t \cdot R_2(\vec{r}))$ term is proportional to the influence of R_2 at a point $\vec{r}$ in the medium. The $\exp(-i \cdot \omega(\vec{r}) \cdot t)$ term is proportional to the influence of R_2' at a point $\vec{r}$ in the medium and is dependent upon the geometry of the microscopic perturbers (21). The value of the relaxation constant in a tissue can be derived from Eq. [2.18] by integrating over the volume of interest and performing a non-linear, least squares fit to the resulting function:

$$S(t) = S_0 \cdot e^{-R_2^* t} \qquad [2.19]$$

where S_0 represents the magnitude signal immediately after the RF pulse was applied and t represents the time from the centre of the RF pulse to the center of the readout window. This is schematically displayed in figure 2.10:

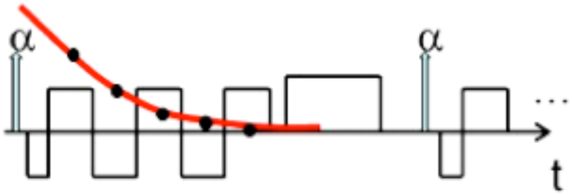

Figure 2.10: Schematic representation of a single repetition period for a multi-echo, GRE sequence. The α symbols denote the excitation pulses The fitted signal decay (red curve) corresponding to equation [2.19] and corresponding measurements points (black dots) are overlaid on the bipolar readout gradient diagram.

GRE methods are particularly useful for fast, whole brain imaging because they employ small RF pulse flip angles and shorter repetition times compared to conventional, spin-echo sequences. Shorter TR periods result in an overall reduced acquisition time for volumetric imaging. Additionally, at UHF, radiofrequency heating mitigates the amplitude of the RF pulses that can be used. The low flip angles used in GRE imaging allows for rapid, whole-brain imaging with UHF MRI without significant tissue heating effects.

2.4 Susceptibility imaging using gradient echo MRI at UHF

Having outlined the foundations of GRE imaging, a brief description of electromagnetic theory applied to susceptibility processing now follows. This section focuses on the basic physics of susceptibility contrast in MRI. A more detailed discussion of processing and reconstruction techniques for susceptibility mapping is presented in Chapter 3.

The human body contains a range of magnetic susceptibility values. Soft tissue and bone are diamagnetically (negatively) shifted relative to water, with susceptibility values ranging from 0 to -30 parts per billion (ppb) of the main magnetic field (22). In contrast, iron and air are paramagnetically shifted relative to water, with susceptibility values ranging from ~ 40 to 400 ppb. The exact susceptibility distribution in the brain, however, is not known a priori (23). It is a function of tissue myelin, iron and protein content, as well as chemical exchange and the microscopic compartmentalization/geometry of water and lipid protons (24, 25).

To determine the susceptibility distribution in tissue, Maxwell's equations are used. According to the theory of magnetostatics, a given susceptibility distribution, $\Delta\chi$, produces a shift in the static magnetic field according to the Laplace equation (26):

$$\Delta B = B_0\left(\frac{\Delta\chi}{3} - \frac{\partial^2 \chi}{\partial z^2}\right) \qquad [2.20]$$

The integral form of equation [2.20] can be written as:

$$\Delta B(\vec{r}) = B_0 \int_{r' \neq r} \chi(r') \frac{3\cos^2(\theta_{rr'}) - 1}{4\pi\left|\vec{r}' - \vec{r}\right|} d^3 r' \qquad [2.21]$$

where $\Delta B(\vec{r})$ denotes the magnetic field shift and $\theta_{rr'}$ is the angle produced by the projection of the long axis of the susceptibility inclusion onto the external magnetic field (27). For simple geometries, the solution to this convolution integral is obtained by using a Green's function expansion (28). From a practical standpoint, however, numerical computation of a solution to equation [2.21] is facilitated by transforming the integral relationship into the Fourier domain and implementing an iterative numerical solution (29). The resulting pointwise multiplication in the Fourier domain is given by:

$$F(\Delta B(\vec{r})) = F(\chi) \times (\frac{1}{3} - \frac{k_z^2}{k^2}) = F(\chi) \times F_d(\vec{k}) \qquad [2.22]$$

where F denotes the Fourier transform and $F_d(k)$ represents the Fourier transform of the dipole convolution kernel (27). Essentially, the Fourier multiplication outlined in equation [2.22] works by assigning a single dipole to each imaging voxel in the LFS map. This significantly reduces the time required for the matrix inversion. However, the value of the Fourier convolution kernel, $F_d(\vec{k}) = \frac{1}{3} - \frac{k_z^2}{k^2}$, is not defined for k = 0 (27, 29). The consequences of such a singularity, as well as methods for dealing with the coefficients where k = 0, are discussed further in Chapter 3.

Chapter 2 has focused on the fundamental concepts employed in QS mapping relevant to this thesis. Both QS mapping and the associated area of electromagnetic tissue properties mapping constitute relatively new areas of research having the potential for multiple future applications.

The development of a processing pipeline for multi-echo gradient-echo based quantification of tissue magnetic properties (R_2^*, LFS and $\Delta\chi$) is discussed in Chapter 3.

2.5 References

1. Haacke, E. M., R. W. Brown, M. R. Thompson, and R. Venkatesan. 1999. *Magnetic resonance imaging: physical principles and sequence design*. Wiley-Liss, New York.
2. Liang, Z.-P., and P. C. Lauterbur. 2000. *Principles of magnetic resonance imaging: a signal processing perspective*. SPIE Optical Engineering Press, New York.
3. Hornak, J. P. 1997. Basics of NMR.
4. De Graaf, R. A. 2008. *In vivo NMR spectroscopy: principles and techniques*. John Wiley & Sons, New Jersey.
5. Bernstein, M. A., K. F. King, and X. J. Zhou. 2004. *Handbook of MRI pulse sequences*. Elsevier Academic Press, Massachusetts.
6. Bloembergen, N., E. M. Purcell, and R. V. Pound. 1948. Relaxation effects in nuclear magnetic resonance absorption. *Physical Review* 73: 679.
7. Solomon, I. 1955. Relaxation processes in a system of two spins. *Physical Review* 99: 559.
8. Cowan, B. 2005. *Nuclear magnetic resonance and relaxation*. Cambridge University Press, Cambridge, United Kingdom.
9. Levitt, M. H. 2013. *Spin dynamics*. John Wiley & Sons, New Jersey.
10. Kwan, R. K.-S., A. C. Evans, and G. B. Pike. 1999. MRI simulation-based evaluation of image-processing and classification methods. *Medical Imaging, IEEE Transactions on* 18: 1085-1097.
11. Benoit-Cattin, H., F. Bellet, J. Montagnat, and C. Odet. 2003. Magnetic Resonance Imaging (MRI) simulation on a grid computing architecture. Cluster Computing and the Grid, 2003. Proceedings. CCGrid 2003. 3rd IEEE/ACM International Symposium on: 582-587.
12. Plewes, D. B., and W. Kucharczyk. 2012. Physics of MRI: a primer. *J Magn Reson Imaging* 35: 1038-1054.
13. Liang, Z.-P., and P. C. Lauterbur. 2000. *Principles of magnetic resonance imaging: a signal processing perspective*. SPIE Optical Engineering Press, New York.
14. Reichenbach, J. R., and E. M. Haacke. 2011. *Susceptibility Weighted Imaging in MRI: Basic Concepts and Clinical Applications*. John Wiley & Sons, New Jersey

15. Reichenbach, J. R. 2012. The future of susceptibility contrast for assessment of anatomy and function. *Neuroimage* 62: 1311-1315.
16. Haase, A., J. Frahm, D. Matthaei, W. Hanicke, and K.-D. Merboldt. 1986. FLASH imaging. Rapid NMR imaging using low flip-angle pulses. *Journal of Magnetic Resonance (1969)* 67: 258-266.
17. Hargreaves, B. 2012. Rapid gradient‐echo imaging. *Journal of Magnetic Resonance Imaging* 36: 1300-1313.
18. Haacke, E. M., and J. A. Tkach. 1990. Fast MR imaging: techniques and clinical applications. *AJR Am J Roentgenol* 155: 951-964.
19. Reichenbach, J. R., R. Venkatesan, D. A. Yablonskiy, M. R. Thompson, S. Lai, and E. M. Haacke. 1997. Theory and application of static field inhomogeneity effects in gradient‐echo imaging. *Journal of Magnetic Resonance Imaging* 7: 266-279.
20. Yablonskiy, D. A. 1998. Quantitation of intrinsic magnetic susceptibility‐related effects in a tissue matrix. Phantom study. *Magnetic resonance in medicine* 39: 417-428.
21. Yablonskiy, D. A. 1998. Quantitation of intrinsic magnetic susceptibility‐related effects in a tissue matrix. Phantom study. *Magnetic resonance in medicine* 39: 417-428.
22. Schenck, J. F. 1996. The role of magnetic susceptibility in magnetic resonance imaging: MRI magnetic compatibility of the first and second kinds. *Medical physics* 23: 815.
23. de Rochefort, L., R. Brown, M. R. Prince, and Y. Wang. 2008. Quantitative MR susceptibility mapping using piece-wise constant regularized inversion of the magnetic field. *Magn Reson Med* 60: 1003-1009.
24. Lee, J., K. Shmueli, M. Fukunaga, P. van Gelderen, H. Merkle, A. C. Silva, and J. H. Duyn. 2010. Sensitivity of MRI resonance frequency to the orientation of brain tissue microstructure. *Proceedings of the National Academy of Sciences* 107: 5130-5135.

25. Shmueli, K., S. J. Dodd, T. Q. Li, and J. H. Duyn. 2011. The contribution of chemical exchange to MRI frequency shifts in brain tissue. *Magn Reson Med* 65: 35-43.

26. Griffiths, D. J., and R. College. 1999. *Introduction to electrodynamics*. Prentice Hall, Upper Saddle River, NJ.

27. de Rochefort, L., T. Liu, B. Kressler, J. Liu, P. Spincemaille, V. Lebon, J. Wu, and Y. Wang. 2010. Quantitative susceptibility map reconstruction from MR phase data using bayesian regularization: validation and application to brain imaging. *Magn Reson Med* 63: 194-206.

28. Landau, L. D., E. M. Lifšic, J. B. Sykes, J. S. Bell, M. J. Kearsley, and L. P. Pitaevskii. 1960. *Electrodynamics of continuous media*. Pergamon Press, Oxford.

29. Schäfer, A., S. Wharton, P. Gowland, and R. Bowtell. 2009. Using magnetic field simulation to study susceptibility-related phase contrast in gradient echo MRI. *Neuroimage* 48: 126-137.

Chapter 3

Ultra-High Field MRI Susceptibility Processing

The answer to the Great Question … of Life, the Universe and Everything
… is Forty-two.
– Douglas Adams, *The Hitchhiker's Guide to the Galaxy*

3.1 Human brain tissue magnetic properties mapping using ultra-high field MRI

Bulk magnetic susceptibility has long been utilized in MRI as a clinically relevant biomarker in studies of venous vessel contrast (1) and functional magnetic resonance imaging (2). In conventional susceptibility-based MRI methods, magnetic field perturbers produce intra-voxel spin dephasing which leads to decreased signal in magnitude images (3, 4). Quantitative susceptibility mapping (QSM), as documented in this thesis, is an extension of these conventional methods. It uses both the local frequency shift (LFS – calculated from the image phase) and the image magnitude information to reconstruct maps of intrinsic tissue magnetic susceptibility (5, 6). QS maps are more specific to tissue properties than conventional susceptibility-weighted imaging (SWI) because they remove the confounding influence of non-local fields and directly measure the mean magnetic field in each voxel. This field is proportional to the concentration of biological perturbers (7, 8).

Calculation of QS maps requires accurate processing of the image phase from multi-echo, multi-channel data. In particular, it requires a pipeline that accounts for (i) channel-dependent phase offsets (9, 10), (ii) phase wraps (11), (iii) non-local background field contributions (6) and (iv) the inverse field to source problem of calculating magnetic susceptibility from LFS (5, 12). In this chapter, we outline the particular phase processing pipeline developed for QSM in this thesis. The pipeline also incorporates calculation of the apparent transverse relaxation rate (R_2^*).

3.2 Phase and susceptibility map processing theory

The first step in generating QS maps from UHF MRI data is calculation of the unwrapped image phase from the complex k-space signal. However, for an MRI coil consisting of multiple elements, it is first necessary to perform element combination in a phase-sensitive manner. This may be accomplished using a number of different methods which differ in how they calculate coil sensitivities and whether or not they incorporate these sensitivities into the combination (10). To achieve acceptable acquisition times for whole brain imaging, channel combination generally must also be performed in conjunction with parallel imaging (13). In the sections which follow, the theory of the gradient echo signal received by a multi-element RF coil array is described and the optimal, phase sensitive coil combination techniques used in this thesis are highlighted.

For a T_2^*-weighted gradient echo image, the magnitude of the signal (I_{mag}) decays exponentially as a function of the echo time (TE) and T_2^* (3, 4). The corresponding phase image, ϕ, is the sum of the global background phase offset, φ_{b0}, the phase term of the B_1^+ field, φ_{b1+}, and the local phase offset due to the susceptibility of tissue, φ_χ, where φ_χ is expressed as:

$$\phi_\chi = 2\pi \Delta f_\chi \mathrm{TE} \qquad [3.1]$$

The Δf_χ term represents the resonance frequency shift of tissue compared to that of pure water. When multi-element RF coils are employed, each coil-element simultaneously receives signal from all voxels weighted by the coil-sensitivity profile (14). In this scenario, for the m^{th} element in the coil array, the coil-sensitivity profile can be written as :

$$C_m = C_{mag,m} e^{i\phi_m} \qquad [3.2]$$

where $C_{mag,m}$ and φ_m represent the element-specific magnitude and phase profiles of the m^{th} element, respectively (15). The signal acquired by the m^{th} coil-element, $S_{m,j}$, is the product of C_m and the true complex image (I)

$$S_{m,j} = C_m I \qquad [3.3]$$

or

$$S_{m,j} = C_{mag,m} I_{mag} e^{i(\phi_{b0} + \phi_{b1} + \phi_m + \phi_\chi)} \qquad [3.4]$$

where φ_{b0} , φ_{b1} , φ_m and φ_χ respectively represent the phase contributions from B_0 inhomogeneities, B_1^+ transmit fields, element-specific phase offsets and tissue structure.

Element-wise coil combination based on Eq. [3.4] can be performed *with* or *without* estimation of coil sensitivity profiles (16). In the following section, the most common coil combination techniques are introduced and the methods used for the experiments in this thesis are highlighted.

3.3 Element combination with coil sensitivity map estimation

When coil sensitivity maps can be computed, combination generally proceeds using one of two techniques: (i) reference-based SENSE (ref-SENSE) (16) or (ii) self-calibrated SENSE (17). Reference-based SENSE requires two sets of images acquired with the same scan parameters. First an image is acquired with a standard volume coil. This is followed by a second image acquired using a multi-element coil. The sensitivity maps are then calculated by complex division of the individual coil element images by the image from the volume coil (16). Because the resulting sensitivity maps are affected by both noise and tissue contrast, they are usually smoothed before performing channel combination. The data from all coil elements is subsequently combined into a single image using least-squares optimization (14).

In self-calibrated SENSE, no volume coil image is necessary. The sensitivity profiles are derived from the complex data of each coil alone (17). The magnitude term of the coil sensitivity is obtained by using the root of sum of squares method (18). The phase term is then calculated either from the phase obtained from the complex sum of all coil-elements or by phase-matching (10). The combined complex image from all elements is then determined using least-squares optimization (17).

3.4 Element combination without coil sensitivity map estimation

At UHF, coil sensitivity profiles are generally not available because volume coils are not utilized for signal detection (10). The standard method for combining receivers when sensitivities are not available is to compute the square root of the sum of squares of the signal for each channel (16, 18). However, since this method discards the phase information, it is unsuitable for QSM. In this case, phase sensitive coil combination can be performed using either (i) simple global phase alignment (10), (ii) phase correction relative to a reference coil (19), or (iii) by referencing the phase in a multi-echo sequence to that of the first echo (Hermitian inner product method) (10). An alternative procedure, specific to multi-echo data, is to perform a singular value decomposition (SVD) of the complex signal (19, 20). This yields the best estimate, in the least squares sense, of both magnetization and coil sensitivity. The two techniques employed for phase sensitive coil combination in this thesis, the Hermitian inner product method and multi-echo SVD are outlined below.

In the Hermitian inner product coil combination, the first echo complex image is subtracted from all subsequent echoes. This is followed by the complex sum of the images for all coil elements (10) as well as for all echoes (denoted by the variable 'j'). In this manner, the φ_m and φ_{b1+} phase contributions are removed because they are static (unchanging with echo time):

$$\phi_{HP,j} = angle(\sum S_{m,j} \cdot S^*_{m,j}) \qquad [3.5]$$

In Eq. [3.5], $S^*_{m,j}$ is the complex conjugate of $S_{m,j}$ and the sum is taken across channels.

In the multi-echo SVD coil combination, the individual coil element magnetization and sensitivity profiles are simultaneously obtained using a point-by-point SVD in the complex image domain. The SVD assumes coil elements have equal and uncorrelated noise. For each point in the image, the coil sensitivity, **C**, is represented by an N × 1 vector where N is the number of coil elements. The magnetization vector, **G**, is represented by a 1 × M vector, with M representing the number of echoes.

Consequently, the signal, **S**, can then be written as an N × M matrix:

$$\mathbf{S} = \mathbf{CG} \qquad [3.6]$$

In reality, the signal received from most multi-channel receive coils is unequal and uncorrelated. Consequently, **S** must be transformed using an estimate of the noise covariance matrix, **V**, such that $\mathbf{S} = \mathbf{V}^{-1}\mathbf{S}$. The SVD is then be computed as follows:

$$\mathbf{S}^{-1} = \mathbf{U\Sigma V}^{\mathbf{H}} \qquad [3.7]$$

where **U** and **V** are orthogonal matrices and **Σ** represents a diagonal matrix of singular values (λ). The singular values in **Σ** are organized such that the largest values occur at the top left corner of the matrix. The first right eigenvector of **V** gives an estimate of the magnetization. An estimate of the coil sensitivity matrix, **C**, is obtained from the first left eigenector of **U**. The final magnetization vector, **G**, which is the main parameter of interest, is obtained by scaling the first right eigenvector of **V** by $\lambda_{1.}$

3.5 Calculating frequency maps from the image phase

Once the complex signal from multiple receiver coils has been combined into one data set, the phase must be unwrapped to remove discontinuities. The wrapped phase contains values that range between $-\pi$ and π and is not usable for QSM (3). Resolving the unwrapped phase involves adding or subtracting 2π from specific pixels located along the phase wrap boundaries (21). This may be performed temporally, if multi-echo data are available, or spatially if only a single-echo is acquired. In this thesis, the unwrapped phase was obtained using a combined spatial (21) and temporal domain unwrapping method (22, 23). The temporal unwrapping is initiated first and unwraps the phase errors across multiple echo times by correcting for jumps larger than ± π occuring from one echo to the next (22). In areas of reduced phase SNR or where open-ended fringe lines exist, temporal unwrapping is insufficient. As a result, in our processing, temporal unwrapping is followed by a 3D spatial domain unwrapping which is a quality-guided, path-based method that uses the wrapped phase image SNR to guide the unwrapping path (21). By unwrapping the highest quality pixels first and the lowest quality pixels last, this method prevents error propagation in the unwrapping process (11).

To obtain frequency maps from the resulting unwrapped phase, the phase is temporally fit to the echo time utilizing a weighted linear regression (24). The linear regression is weighted by the variance in the phase data to reduce noise. This variance can be determined from the complex data, according to (25):

$$\sigma^2(\phi) = \frac{\sigma^2(\mathrm{Re}\{\rho\})}{|\rho|^2} \qquad [3.8]$$

where ρ and ϕ are the magnitude and phase of the voxel and σ^2 denotes the variance operator. Equation [3.8] assumes the distribution of noise in the complex MRI data is zero-mean, Gaussian. The specific formula used for the weighted linear regression is as follows:

$$f_{tot} = \frac{(\Sigma|\rho_i|^2)(\Sigma|\rho_i|^2 t_i \varphi_i) - (\Sigma|\rho_i|^2 t_i)(\Sigma|\rho_i|^2 \varphi_i)}{(\Sigma|\rho_i|^2)(\Sigma|\rho_i|^2 t_i^{\,2}) - (\Sigma|\rho_i|^2 t_i)^2} \qquad [3.9]$$

where f_{tot} denotes the desired macroscopic frequency map and ρ_i and ϕ_i are the magnitude and phase of the voxel at time t_i (24). However, equation [3.9] does not hold for the case of single-echo, gradient echo acquisitions. In the case of single-echo acquisitions, the macroscopic frequency shift is obtained from the following equation:

$$f_{tot} = \frac{\varphi}{TE} \cdot \frac{TE}{\sigma^2(\phi)} \qquad [3.10]$$

where the second multiplicative term on the right side of the equation [3.10] denotes the variance weighting (3).

3.6 Background field removal

Once the macroscopic frequency maps have been reconstructed, it is necessary to remove the influence of frequency contributions arising from air-tissue interfaces, high-order shimming, and other sources of field perturbation existing outside the brain (5). To remove these background contributions, the macroscopic frequency variation is divided into frequency contributions originating from sources outside the brain (f_{ext}) and those originating from sources inside the brain (f_{int}) according to the Sophisticated Harmonic Artifact Reduction from Phase data (SHARP) method first proposed by Schweser et al. (6). Accordingly, the total frequency shift at a voxel (f_{tot}) is given by:

$$f_{tot} = f_{int} + f_{ext} \qquad [3.11]$$

Determination of f_{int} from f_{tot} is performed using the known physical properties of the internal and external frequency shifts. f_{ext} satisfies Laplace's equation because it results from sources existing outside the volume of interest (VOI):

$$\nabla^2 f_{ext} = 0 \qquad [3.12]$$

Consequently, applying the Laplacian operator to f_{tot} results in the following relationship:

$$\nabla^2 f_{tot} = \nabla^2 f_{\text{int}} \qquad [3.13]$$

The solution to Eq. [3.13] is calculated by applying the mean value property of harmonic functions (26, 27). According to this property, any harmonic function is preserved under convolution with a non-negative, radially symmetric, normalized function (26). As it applies to background field removal, a radially symmetric, normalized function *h(r)* can be multiplied into equation [3.11] and subtracted from the original total frequency shift, resulting in the following interim data set:

$$f_{interim} = f_{tot} - h(r) \otimes f_{tot} \qquad [3.14]$$

One example of the convolution function is a radially symmetric spherical kernel. An example of such a kernel for radii varying from 7 – 11 mm is illustrated below:

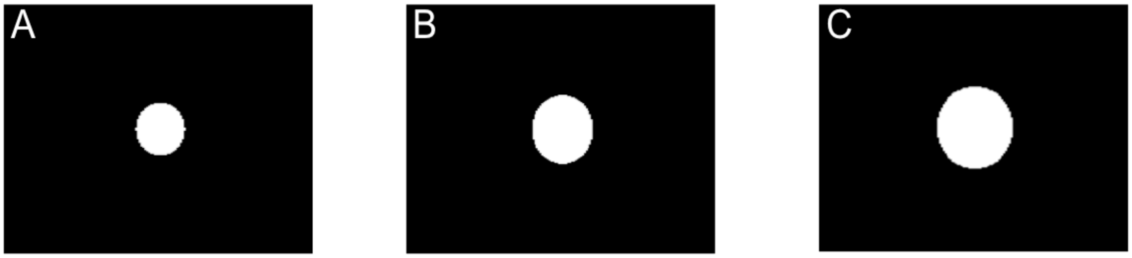

Figure 3.1: SHARP background filter convolution kernels with varying radii. **A - C** show spherical kernels with radii of 7, 9 and 11 mm respectively.

In our specific implementation of Eq. [3.14], the convolution function, *h(r)*, was a spherical kernel which extended over a radius of 7 – 11 mm. A larger spherical convolution kernel resulted in improved background field removal at the expense of increased erosion of pixels at the edge of the brain:

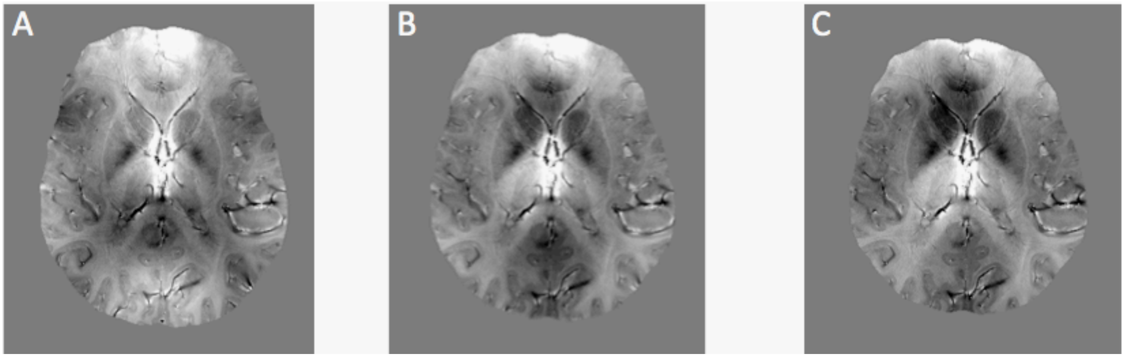

Figure 3.2: SHARP filtered LFS maps generated using an increasing spherical kernel radius. **A - C** show LFS maps generated with SHARP spherical kernels of 7, 9 and 11 mm respectively. In **C,** background field removal is more efficient at the center of the brain, while more regions at the edge of the brain are lost due to erosion.

Since f_{ext} obeys the harmonic mean value theorem, Eq. [3.14] can be reduced to:

$$f_{interim} = f_{int} - h(r) \otimes f_{int}$$

$$= (\sigma - h(r)) \otimes f_{int} \qquad [3.15]$$

where σ represents the Dirac delta function. As a result, Eq. [3.15] can be solved to isolate f_{int} using a deconvolution operation:

$$f_{int} = (\sigma - h(r)) \otimes^{-1} f_{interim} \qquad [3.16]$$

The values in $f_{interim}$ are corrupted at the edge of the VOI because the convolution is carried out using a kernel which extends into the region outside the brain. In order to compensate for this effect, the deconvolution of Eq. [3.16] must be limited to a region where non-zero values of $f_{interim}$ exist. This results in an erosion of the phase data at the edge of the brain by an amount equal to the radius of the convolution kernel function.

3.7 Calculating volume magnetic susceptibility from the LFS map

According to Maxwell's equations, the true susceptibility distribution in a tissue is related to the internal frequency shift by the following convolution:

$$\Delta B(\vec{r}) = B_0 \int_{r' \neq r} \chi(r') \frac{3\cos^2(\theta_{rr'}) - 1}{4\pi \left| \vec{r'} - \vec{r} \right|} d^3 r' \qquad [3.17]$$

where $\Delta B(r)$ denotes the magnetic field shift and $\theta_{rr'}$ is the angle produced by the projection of the long axis of the susceptibility inclusion onto the external magnetic field (28). The solution to this convolution integral over a volume is obtained in the spatial domain by using a Green's function expansion for simple geometries. However, in medical imaging both $\Delta B(r)$ and $\chi(r')$ are defined by large matrices. For practical computation, the inversion of Eq. [3.17] in the spatial domain requires tens to hundreds of gigabytes, if each matrix is formed explicitly (5). The computation of $\chi(r')$ from Eq. [3.17] can be performed more simply if the problem is formulated in the Fourier domain (29). With this approach, the magnetic susceptibility map can be numerically calculated from the the LFS utilizing a k-space based, regularized inversion with a conjugate gradient algorithm. By defining the k-space representation of f_L as f_L(k) and the k-space representation of $\Delta\chi$ as $\Delta\chi$(k), the local resonance frequency map is related to the volume magnetic susceptibility as follows (5):

$$f_L(k) = \left(\frac{1}{3} - \frac{k_z}{k^2} \right) \cdot \Delta\chi\,(k) \qquad [3.18]$$

Equation [3.18] can also be written in matrix form as:

$$\delta = C\mathrm{X} \qquad [3.19]$$

where δ denotes the k-space local frequency shift, *C* represents the Fourier domain dipole convolution kernel and the variable *X* denotes the Fourier domain susceptibility distribution of interest. A visual representation of the convolution function, C, in the axial plane is given below:

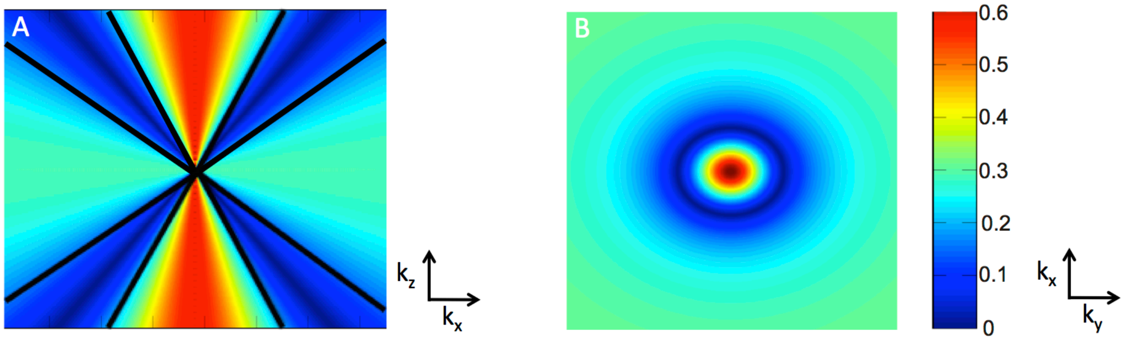

Figure 3.3: Numerically-generated dipole convolution kernel employed in QSM inversion. The kernel is displayed using: **(A)** a 2D view in the k_z-k_x (sagittal plane) and **(B)** a 2D view in the k_x-k_y plane (axial plane). The black lines in Fig. 3.3B denote regions of the Fourier domain where the convolution kernel has very small values. This property of the convolution kernel makes the inversion of equation [3.18] an ill-conditioned problem.

Calculation of QS maps from the LFS requires inversion of the linear system of equations represented by Eq. [3.19]. Theoretically, direct inversion can be used to yield *X*. However, since the dipole convolution function, *C*, has zeros on a conical surface defined by $2k_z^2 = k_x^2 + k_y^2$ (this is visually displayed by the black lines in Fig. 3.3B), a direct inversion is ill-conditioned in areas where *C* is small. A common method used for reconstruction of accurate susceptibility maps is quadratic minimization of a regularized least-squares objective function (5, 6). For this purpose, Eq. [3.19] can be written as a weighted least-squares problem with spatial priors:

$$\min_X \|W(C\mathrm{X}-\delta)\|_2^2 - \alpha^2\|W_0\mathrm{X}\|_2^2 + \beta^2\|W_1G\mathrm{X}\|_2^2 \qquad [3.20]$$

where W, W_0 and W_1 are weighting matrices (spatial prior information) defined as: a binary mask of the brain in the second echo magnitude image (W_0), the magnitude image itself (W) and the gradient norm of the magnitude image (W_1). These spatial priors for a gradient echo brain image obtained from 7 T MRI are displayed below:

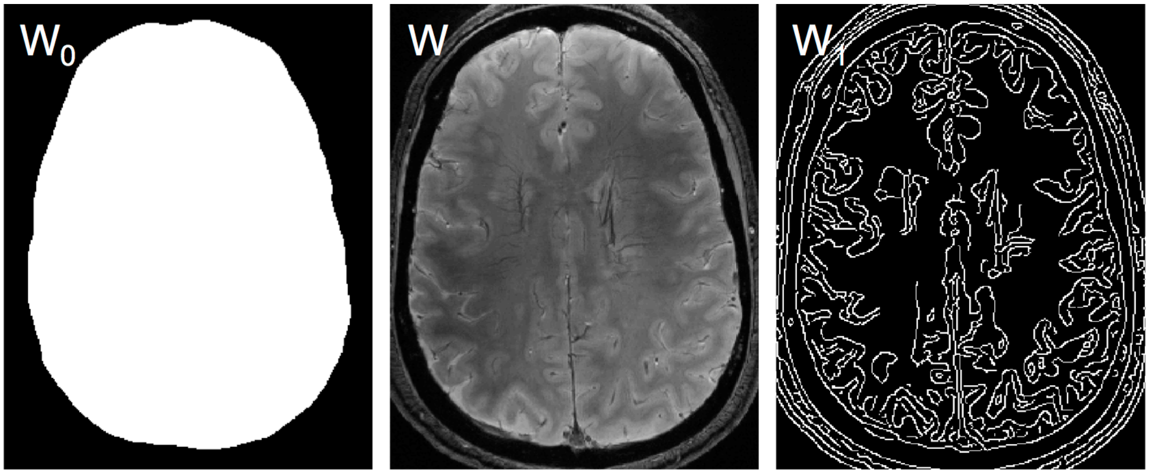

Figure 3.4: Spatial priors used in calculation of susceptibility maps from LFS maps.

A minimum quadratic form of Eq. [3.20] is solved using the conjugate gradient normal residual (CGNR) method in the numerical implementation of QSM (5):

$$C^*W^*WC\,\mathrm{X} - \alpha^2 W_0^* W_0\,\mathrm{X} + \beta^2 G^* W_1^* W_1 G\,\mathrm{X} = C^* W^* W\delta \qquad [3.21]$$

Previous work in our lab has revealed that optimum values of α^2 and $\beta^2 = 1 \times 10^4$ are appropriate for realistic reconstruction of susceptibility in human brain at 7 T. These values were chosen because they resulted in the smallest log residual at the transition point in the L-curve. They also reconstructed constant, realistic values for susceptibility over a range of iterative steps in the CGNR algorithm implemented in Matlab (R2013).

Accurate, reproducible QS mapping requires calculation of QS values relative to a common reference structure. In this study, the mean QS value calculated from bilateral ROIs in frontal deep white matter was used as a reference tissue. Frontal white matter has previously (12) been used effectively as a reference structure in high-resolution QS mapping at 7 T in healthy subjects.

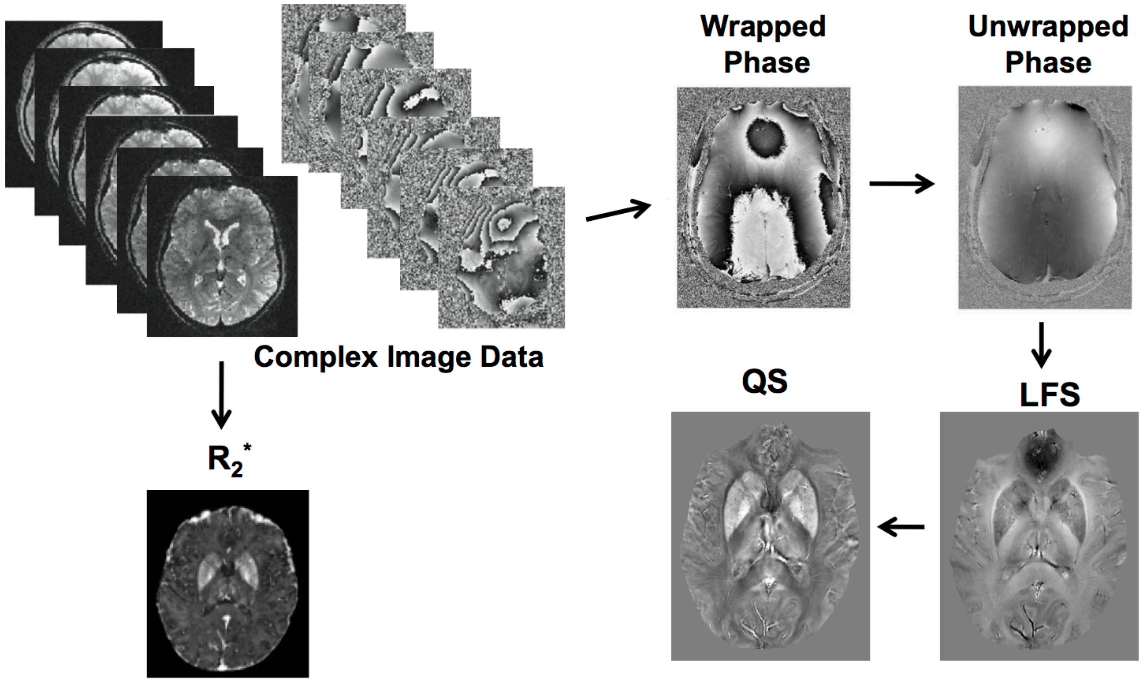

Figure 3.5: Full processing pipeline utilized in this thesis for channel combination, R_2^*, LFS and QS mapping.

3.8 R_2^* mapping

Exponential fitting of the MRI signal decay has been used extensively in MR research to perform quantitative T_2^* and T_2 mapping (30, 31). For example, nuclear-nuclear and nuclear-electron magnetic interactions give rise to the longitudinal (T_1) and transverse

(T_2) relaxation rates of water molecules used to characterize tissue properties in quantitative MRI (32). Another relaxation-based quantitative MRI parameter often employed to characterize tissue properties is the apparent transverse relaxation rate, $R_2^* = 1/T_2^*$ (3, 16). The variable $R_2^* = R_2 + R_2'$, with R_2' representing the contribution to the signal relaxation rate from local magnetic field inhomogeneities. R_2' is mediated by two major factors: (i) the difference in local magnetic field experienced by nuclei in different magnetic environments and (ii) nuclear spin diffusion through an inhomogeneous magnetic field (33).

If the MRI signal decay due to magnetic moment dephasing is faster than the rate of diffusion, the signal decay due to R_2^* is said to be in the "static dephasing regime" or "slow molecular motion regime" (33). In this case, the dominant contribution to R_2^* is the difference in local magnetic fields experienced by nuclei and the influence of diffusion may be neglected. In this thesis, the static dephasing regime is assumed when computing all the susceptibility-based qMRI metrics.

The signal properties of water protons relaxing under the influence of $R_2^* = 1/T_2^*$ decay can be modeled for a gradient echo acquisition using the following expression:

$$S(TE) = S_0 \cdot \exp(\frac{-TE}{T_2^*}) \qquad [3.22]$$

where TE represents the time between the RF excitation and the center of the data acquisition and S_0 identifies the magnitude signal intensity prior to any T_2^* decay (3). T_2^* can be calculated based on equation [3.22] by measuring the decay in a gradient echo acquisition at various time points after the RF excitation pulse. These measurements can then be fit assuming a mono-exponential decay curve (red line in figure 2.10 of Chapter

2). Acquisition of the decay curve at various time points is performed using either a 2D or 3D MRI sequence. Because of its higher SNR and shorter scan time for whole-brain imaging, 3D gradient echo imaging was employed in all work documented in this thesis.

Quantitative maps of the apparent transverse relaxation rate, R_2^*, were calculated using an interior-point, least-squares fitting routine for non-linear equations. For the data acquired in the MS imaging study, the following mono-exponential decay function:

$$S(TE) = S_0 \cdot \exp(\frac{TE}{T_2^*}) \cdot \left| sinc(\frac{\gamma \cdot \Delta B_z \cdot TE}{2}) \right| \qquad [3.23]$$

was fit to the magnitude data to account for the effects of B_0 field inhomogeneity in the R_2^* decay signal (34, 35). In equation [3.23], TE represents the echo time and S_0 represents the signal intensity at TE = 0 ms. ΔB_z represents the gradient of the magnetic field along the Z-direction. The ΔB_z term must be calculated independently for use in Eq. [3.23]. The sinc term in Eq. [3.23] is applied to model the effect of B_0 field inhomogeneity on the T_2^* decay curve (34).

The next chapter presents a fundamental research study using combined R_2^*, LFS and QS mapping with multi-echo, gradient echo MRI at high-field and ultra-high resolution.

3.9 References

1. Haacke, E. M., Y. Xu, Y. N. Cheng, and J. R. Reichenbach. 2004. Susceptibility weighted imaging (SWI). *Magnetic Resonance in Medicine* 52: 612-618.
2. Ogawa, S., T. M. Lee, A. R. Kay, and D. W. Tank. 1990. Brain magnetic resonance imaging with contrast dependent on blood oxygenation. *Proc Natl Acad Sci U S A* 87: 9868-9872.
3. Haacke, E. M., R. W. Brown, M. R. Thompson, and R. Venkatesan. 1999. *Magnetic resonance imaging: physical principles and sequence design*. Wiley-Liss New York:
4. Yablonskiy, D. A., and E. M. Haacke. 1994. Theory of NMR signal behavior in magnetically inhomogeneous tissues: the static dephasing regime. *Magnetic Resonance in Medicine* 32: 749-763.
5. de Rochefort, L., T. Liu, B. Kressler, J. Liu, P. Spincemaille, V. Lebon, J. Wu, and Y. Wang. 2010. Quantitative susceptibility map reconstruction from MR phase data using bayesian regularization: validation and application to brain imaging. *Magn Reson Med* 63: 194-206.
6. Schweser, F., A. Deistung, B. W. Lehr, and J. R. Reichenbach. 2011. Quantitative imaging of intrinsic magnetic tissue properties using MRI signal phase: an approach to in vivo brain iron metabolism? *Neuroimage* 54: 2789-2807.
7. Li, W., B. Wu, A. V. Avram, and C. Liu. 2012. Magnetic susceptibility anisotropy of human brain in vivo and its molecular underpinnings. *Neuroimage* 59: 2088-2097.
8. Liu, C., W. Li, G. A. Johnson, and B. Wu. 2011. High-field (9.4 T) MRI of brain dysmyelination by quantitative mapping of magnetic susceptibility. *Neuroimage* 56: 930-938.
9. Hammond, K. E., J. M. Lupo, D. Xu, M. Metcalf, D. A. Kelley, D. Pelletier, S. M. Chang, P. Mukherjee, D. B. Vigneron, and S. J. Nelson. 2008. Development of a robust method for generating 7.0 T multichannel phase images of the brain with application to normal volunteers and patients with neurological diseases. *Neuroimage* 39: 1682-1692.

10. Robinson, S., and J. Jovicich. 2011. B0 mapping with multi-channel RF coils at high field. *Magn Reson Med* 66: 976-988.
11. Rauscher, A., M. Barth, J. R. Reichenbach, R. Stollberger, and E. Moser. 2003. Automated unwrapping of MR phase images applied to BOLD MR-venography at 3 Tesla. *J Magn Reson Imaging* 18: 175-180.
12. Deistung, A., A. Schafer, F. Schweser, U. Biedermann, R. Turner, and J. R. Reichenbach. 2013. Toward in vivo histology: a comparison of quantitative susceptibility mapping (QSM) with magnitude-, phase-, and R2*-imaging at ultra-high magnetic field strength. *Neuroimage* 65: 299-314.
13. Reichenbach, J. R. 2012. The future of susceptibility contrast for assessment of anatomy and function. *Neuroimage* 62: 1311-1315.
14. Pruessmann, K. P., M. Weiger, M. B. Scheidegger, and P. Boesiger. 1999. SENSE: sensitivity encoding for fast MRI. *Magn Reson Med* 42: 952-962.
15. Bernstein, M. A., M. Grgic, T. J. Brosnan, and N. J. Pelc. 1994. Reconstructions of phase contrast, phased array multicoil data. *Magn Reson Med* 32: 330-334.
16. Bernstein, M. A., K. F. King, and X. J. Zhou. 2004. *Handbook of MRI pulse sequences*. Access Online via Elsevier,
17. Chen, Z., L. A. Johnston, D. H. Kwon, S. H. Oh, Z. H. Cho, and G. F. Egan. 2010. An optimised framework for reconstructing and processing MR phase images. *Neuroimage* 49: 1289-1300.
18. Roemer, P. B., W. A. Edelstein, C. E. Hayes, S. P. Souza, and O. M. Mueller. 1990. The NMR phased array. *Magn Reson Med* 16: 192-225.
19. Bydder, M., D. J. Larkman, and J. V. Hajnal. 2002. Combination of signals from array coils using image‐based estimation of coil sensitivity profiles. *Magnetic Resonance in Medicine* 47: 539-548.
20. Walsh, D. O., A. F. Gmitro, and M. W. Marcellin. 2000. Adaptive reconstruction of phased array MR imagery. *Magnetic Resonance in Medicine* 43: 682-690.
21. Abdul-Rahman, H. S., M. A. Gdeisat, D. R. Burton, M. J. Lalor, F. Lilley, and C. J. Moore. 2007. Fast and robust three-dimensional best path phase unwrapping algorithm. *Appl Opt* 46: 6623-6635.

22. Xiang, Q. 1995. Temporal phase unwrapping for CINE velocity imaging. *Journal of Magnetic Resonance Imaging* 5: 529-534.
23. Judge, T. R., and P. J. Bryanston-Cross. 1994. A review of phase unwrapping techniques in fringe analysis. *Optics and Lasers in Engineering* 21: 199-239.
24. Kressler, B., L. de Rochefort, T. Liu, P. Spincemaille, Q. Jiang, and Y. Wang. 2010. Nonlinear regularization for per voxel estimation of magnetic susceptibility distributions from MRI field maps. *IEEE Trans Med Imaging* 29: 273-281.
25. Conturo, T. E., and G. D. Smith. 1990. Signal‑to‑noise in phase angle reconstruction: Dynamic range extension using phase reference offsets. *Magnetic Resonance in Medicine* 15: 420-437.
26. Roy, K. K. 2008. *Potential theory in applied geophysics*. Springer,
27. Griffiths, D. J., and R. College. 1999. *Introduction to electrodynamics*. prentice Hall Upper Saddle River, NJ,
28. Jackson, J. D., and R. F. Fox. 1999. Classical electrodynamics. *American Journal of Physics* 67: 841.
29. Schäfer, A., S. Wharton, P. Gowland, and R. Bowtell. 2009. Using magnetic field simulation to study susceptibility-related phase contrast in gradient echo MRI. *Neuroimage* 48: 126-137.
30. Tofts, P. S., and E. P. G. H. Du Boulay. 1990. Towards quantitative measurements of relaxation times and other parameters in the brain. *Neuroradiology* 32: 407-415.
31. Tofts, P. 2005. *Quantitative MRI of the brain: measuring changes caused by disease*. Wiley. com,
32. Tofts, P. S., and E. P. G. H. Du Boulay. 1990. Towards quantitative measurements of relaxation times and other parameters in the brain. *Neuroradiology* 32: 407-415.
33. Yablonskiy, D. A., and E. M. Haacke. 1994. Theory of NMR signal behavior in magnetically inhomogeneous tissues: the static dephasing regime. *Magn Reson Med* 32: 749-763.
34. Peters, A. M., M. J. Brookes, F. G. Hoogenraad, P. A. Gowland, S. T. Francis, P. G. Morris, and R. Bowtell. 2007. T2* measurements in human brain at 1.5, 3 and 7 T. *Magn Reson Imaging* 25: 748-753.

35. Cohen-Adad, J., J. R. Polimeni, K. G. Helmer, T. Benner, J. A. McNab, L. L. Wald, B. R. Rosen, and C. Mainero. 2012. T(2)* mapping and B(0) orientation-dependence at 7 T reveal cyto- and myeloarchitecture organization of the human cortex. *Neuroimage* 60: 1006-1014.

Chapter 4

Origins of R_2^* Orientation Dependence in Gray and White Matter

Our brain – with its 100 billion neurons and quadrillion synapses, give or take a few billion here or there – is one of the most complex entities to demystify.

– Eric J. Tople, *The Creative Destruction of Medicine*

4.1 Introduction

In many neurological diseases such as multiple sclerosis, Alzheimer's and Parkinson's, and in conditions following traumatic brain injury, microstructural changes occur in gray and white matter (1-4). One method for quantifying these microstructural changes is mapping of the effective transverse relaxation rate (R_2^*). Along with T_1 and T_2, T_2^* (1/ R_2^*) has been viewed as a fundamental MRI tissue parameter, affected by several factors including myelin content (5, 6), endogenous ferritin-based (Fe^{3+}) iron (7, 8), tissue microstructure (6) and paramagnetic, blood deoxyhemoglobin (9). However, a number of recent studies have reported a somewhat surprising dependence of R_2^* on tissue orientation, at least in white matter (10-12). The purpose of this paper was to investigate the mechanisms that could contribute to this orientation dependence of R_2^* in both gray and white matter. Because R_2^* is influenced by magnetic field perturbations, we examined the role of the local Larmor frequency shift (f_L) and the quantitative magnetic susceptibility ($\Delta\chi$), parameters that relate field and frequency. Through this analysis we identified novel scaling relations that relate R_2' to the local Larmor frequency shift calculated after removal of macroscopic field inhomogeneities. Additionally, we compared for the first time, two methods for computing $\Delta\chi$ in gray and white matter: (i) fitting the Generalized Lorentzian (GL) Model of field perturbers (13) to f_L measured at multiple brain orientations and (ii) magnitude-regularized dipole inversion (14). The difference between these two estimates represents the local frequency shift due to a cylindrical, axon geometry and is a marker of axonal integrity.

Having modeled the orientation dependence, we next examined the effect of myelin and iron on both R_2^* and $\Delta\chi$. We demonstrated a linear correlation between these quantities and optical density (OD) derived from DAB-enhanced Perls stain (sensitive to ferritin-based iron) for cortical gray matter. Similarly, using OD derived from solochrome cyanine-R stained slides in rat brain major white matter fiber regions, we showed strong positive correlations between the transverse relaxation constants, R_2 and R_2', and myelin density. Taken together, our results demonstrate that observed R_2^* values in *ex vivo* brains can be explained by a sinusoidal dependence on tissue microstructure orientation in conjunction with a linear dependence on the myelin concentration in cortical gray and white matter. In deeper gray matter structures with no preferred symmetry axis, R_2^* does not have an orientation dependence but retains a linear dependence on iron concentration.

4.2 Theory

4.2.1 Orientation dependence of R_2^* white matter

Recently, Lee *et al.* (12) used a theoretical model developed by Yablonskiy and Haacke (15) to fit an orientation-dependence curve to R_2^* data from *ex vivo,* fixed human corpus callosum at 7 T. The model assumes that the orientation dependence of R_2^* in groups of close-packed, parallel white matter fibers can be approximated with the following equation:

$$R_2^*(\theta) = C_0 + C_1 \sin(2\theta + \psi_0) \qquad [4.1]$$

where C_0, C_1 and ψ_0 are constants and θ is the angle of the longitudinal axis of the fiber tract relative to the B_0 field. Eq. 4.1 is an extension of the standard relationship for R_2^* :

$$R_2^* = R_2 + R_2' \qquad [4.2]$$

The C_0 constant in Eq. 4.1 represents the conventional transverse relaxation rate, R_2, as well as any contributions to R_2' that are not angularly dependent (e.g. R_2' shifts due to endogenous ferritin-based iron). For white matter fiber bundles, the constant C_1 is defined as

$$C_1 = 2\pi\, \omega_0\, \zeta\, \Delta\chi \qquad [4.3]$$

where the variable ζ represents the volume fraction of field perturbers and Δχ represents the magnetic susceptibility difference between a fiber bundle and the medium surrounding the bundle. In this paper, we validated the orientation dependence model of Eq. 4.1 (specifically, the relation $C_1 = 2\pi\, \omega_0\, \zeta\, \Delta\chi$) by comparing the fitted parameters from the linear R_2^* model to the value of Δχ calculated from the Generalized Lorentzian model of field perturbers (further discussed in the next section of this paper). To perform this comparison, the OD of myelin obtained from histochemical staining and slide registration was used as a surrogate for the volume fraction (ζ). Throughout this paper we define the R_2' value as being the same as C_1. According to the original derivation (15), the true value of R_2' for a network of parallel fibers is $2\pi\, \omega_0\, \zeta\, \Delta\chi\, \sin(2\theta)$. Since we are explicitly modeling the orientation dependence of R_2', we use the constant C_1 to define the *amplitude* of the R_2' variation with fiber angle. Consequently, we treat C_1 as a surrogate measure of R_2'.

The orientation-dependence of the R_2^* signal has also been characterized with an alternative, second-order model of field-perturbers. This model postulates that two distinct components contribute to the orientation dependence of R_2^* in white matter: (i) an isotropic component associated with the cylindrical geometry of myelinated axons (13) and (ii) an anisotropic component associated with the phospholipid bilayer structure of myelin (12). The equation for the second-order model is

$$R_2^*(\theta) = C_0 + C_1 \sin(2\theta + \psi_0) + C_2 \sin(4\theta + 2\psi_0 - \frac{\pi}{2}) \qquad [4.4]$$

In this study, we compared the linear and second-order R_2^* models in rat brain major white matter fiber bundles.

4.2.2 Gray matter

Eq. 4.1 was also used to fit R_2^* orientation dependence in gray matter. The orientation of gray matter was defined as the angle between the normal to the cortical surface and B_0. This technique, previously employed by Cohen-Adad (16), is physically motivated by the fact that myelinated white matter tracts project into cortical gray matter where they synapse onto cortical neurons, conferring a preferred axis of symmetry in the cortical gray matter.

4.2.3 Orientation-dependence of f_L in white matter

The theoretical field shift around a susceptibility inclusion has conventionally been calculated in NMR using the Lorentzian sphere formalism. However, this approach has been questioned for modeling brain tissue structures such as axons that have non-spherical boundaries. Instead, an alternative Generalized Lorentzian Model (GL model) has been suggested by He and Yablonskiy (13) for modeling field perturbers in the static dephasing regime. This model, with application to external capsule white matter in rat brain, is discussed in detail in what follows.

The external capsule is a large white matter tract that extends longitudinally through the rat brain in the anterior-posterior direction. The local Larmor frequency shift of water molecules moving inside parallel axons of the external capsule bundle relative to the external gray matter can be calculated using the Lorentzian cylinder approximation of He and Yablonskiy (13). In this approximation, a model Lorentzian cylinder surrounds the white matter bundle and has a diameter larger than that of the bundle. The nuclei of water molecules inside the axon bundle experience a frequency shift that is the summation of the contributions from point magnetic dipoles which exist either (i) inside or (ii) outside a Lorentzian cylinder. The magnetic field experienced by nuclei due to dipoles existing inside the Lorentzian cylinder averages to zero because the average magnetic field around a point dipole is zero. Consequently, the frequency shifts of the nuclei inside the external capsule are influenced by point dipoles in the medium outside the cylinder of Lorentz.

Along the anterior-posterior direction, the external capsule bundle can be considered as an infinite circular cylinder with a length significantly larger than its diameter. In this regime, we can write the frequency shift for external capsule white matter as:

$$\frac{f_{L,WM}}{f_0} = -2\pi(\chi_{ae} - \chi_{WM}) \cdot (\cos^2\theta - \frac{1}{3}) \qquad [4.5]$$

where $f_{L,WM}$ is the local frequency shift in the white matter relative to the surrounding, isotropic gray matter medium, χ_{ae} (ppm) is the magnetic susceptibility of the isotropic medium surrounding the axon bundle, χ_{WM}= 0.067 ppm is the magnetic susceptibility of myelin in white matter (13) and θ is the orientation angle of an axon bundle relative to the B_0 field.

Throughout this chapter, $\Delta\chi$, calculated by fitting the GL model (Eq. 4.5) to f_L measured with varying brain orientations, is denoted as $\Delta\chi_{GLModel}$ to differentiate it from the magnetic susceptibility calculated using a regularized dipole inversion method ($\Delta\chi_{dipole}$) outlined below. All magnetic susceptibility values are written in SI units and are calculated relative to the average magnetic susceptibility in an adjacent cortical gray matter ROI.

4.2.4 Gray Matter

We also examined the orientation dependence of f_L in cortical gray matter. The presence of cortical fibers should, theoretically, give rise to an orientation dependence described by Eq. 4.5. We tested this hypothesis in cortical gray matter regions evenly distributed around the cortex. The $\Delta\chi = \chi_{ae} - \chi_{WM}$ term in Eq. 4.5 was replaced by $\Delta\chi = \chi_{ae} - \chi_{GM\_average}$

where $\chi_{GM\_average}$ is the average susceptibility of gray matter measured from multiple ROIs evenly distributed around the cortex.

4.2.5 Reconstruction of quantitative susceptibility maps from single-orientation f_L maps

According to Maxwell's equations, a volume magnetic susceptibility distribution, $\Delta\chi$ (ppb), produces an associated local frequency shift, f_L (Hz). Defining the k-space representation of f_L as f_L(k) and the k-space representation of $\Delta\chi$ as $\Delta\chi$(k), the local resonance frequency map is related to the volume magnetic susceptibility as follows (14, 17, 18):

$$f_L(k) = (\frac{1}{3} - \frac{k_z}{k^2}) \cdot \Delta\chi(k) \qquad [4.6]$$

Calculation of $\Delta\chi_{dipole}$ maps from the f_L requires inversion of Eq. 4.6. A common method used for this inversion is quadratic minimization of a regularized, least-squares objective function (14). The technique from (14) was employed for calculation of $\Delta\chi_{dipole}$ in this work by implementing a regularized CGNR algorithm in Matlab (R2008b, The MathWorks, Natwick, MA, USA). Calculation of magnetic susceptibility in this study was performed using a single-orientation.

4.3 Materials and Methods

4.3.1 Measuring the orientation dependence of R_2^* and f_L

The orientation dependence of R_2^* and f_L was experimentally measured in both hemispheres of the rat brain, in white matter fiber tracts and gray matter (n=3 brains, 2 hemispheres, 18 orientations). Each rat brain was scanned with the medial fissure of the brain oriented at 18 different sampling angles relative to the main field of the magnet.

Specifically, each brain was rotated to (i) eight unique angles of n × 45° (n = 1…8) about the y-axis shown in Fig. 4.1c, as well as (ii) 10 additional angles chosen to produce an even sampling of the unit sphere. Reproducible rotations were achieved by using the sample holder shown in Fig. 4.1.

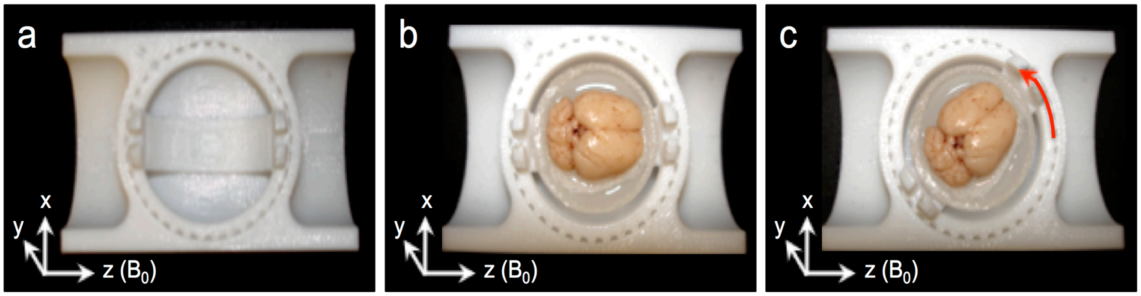

Figure 4.1: Custom-machined sample container/experimental setup for imaging. (a) Custom-machined sample container and (b,c) experimental setup illustrating rat brain immersed in MRI invisible, fluorinated fluid. Each increment on the sample container represents a ten degree rotation about the y-axis.

To improve SNR, five contiguous, 100 μm slices in each R_2^* and f_L map were averaged. An average R_2^* and f_L was measured in each ROI specified in Fig. 4.2a (white matter) and 2e,i (gray matter). The orientation of cortical fibers in each gray matter ROI was determined by referencing to a penetrating cortical vein adjacent to, but not included in, the ROI. These veins conveniently define the normal to the cortical surface.

Data from multiple ROIs in each sample are displayed together in Fig. 4.2(b-l). The minimum point of each sinusoidal, orientation-dependence curve from each ROI was phase shifted so that the vector that defined the initial orientation was effectively aligned with the B_0 field. Once the sinusoidal curves were aligned, R_2^* and f_L data for each ROI was averaged for the three animals.

4.3.2 Preparation of rat brain tissue samples

Three adult, male Sprague-Dawley rats (n=3; 250-300 g) were purchased from Charles River Laboratories (Sherbrooke, Quebec, Canada). Rat brains were excised and fixed in 4% formalin solution for two weeks prior to imaging. Fixation preserves biological tissues from decay by preventing autolysis and halting chemical reactions. It also increases mechanical strength of tissue in preparation for chemical staining. All animal protocols were undertaken in accordance with Animal Care Guidelines, with approval from the Animal Use Subcommittee of Western University.

For imaging, the brains were placed inside a 2.5 cm diameter plastic sphere filled with an MR-invisible, fluorinated solution (Lubrication Technology, Inc**.,** Franklin Furnace, OH). A custom-machined, spherical sample holder allowed accurate rotation of the brain in order to image the sample at different angles relative to the field (Fig. 4.1a-c), while the fluorinated solution minimized the formation of susceptibility-based edge effects in and around the brain because it has a susceptibility which is similar to that of cortical grey matter.

4.3.3 MRI protocol

Imaging was performed on a 9.4 T, 31 cm horizontal bore animal MRI scanner (Agilent Technologies, Santa Clara, California). An in-house designed B_0 field mapping sequence, RASTAMAP (19), was utilized to perform automated higher-order shimming before imaging. The RF coil used for all data collection was a 4 cm diameter millipede coil (Agilent Technologies, Santa Clara, California).

A 3D multi-echo gradient echo acquisition with an imaging field of view of $25.6 \times 25.6 \times 25.6$ mm^3 and an isotropic resolution of 100 μm was used for imaging all brain orientations. The scan parameters were: TR = 50 ms, TE_1 = 3.84 ms, echo spacing = 5.56 ms and 6 echoes.

4.3.4 MR image post-processing and data analysis

From the multi-echo gradient echo magnitude data, mono-exponential R_2^* maps were generated using a Levenberg-Marquardt weighted least squares fitting routine. The variance in the magnitude images was employed as a weighting term in the least-squares fitting.

To correct for the influence of B_0 field inhomogeneity, the voxel spread function (VSF) approach was used as described in (20). The VSF method accounts for the combined effects of both through-plane and in-plane field inhomogeneities, as well as signal leakage from neighbouring voxels.

For registration of the data acquired with different brain orientations, the magnitude image corresponding to the second echo at each brain orientation was co-registered to the volume acquired with the medial fissure of the brain aligned at 0° relative to the B_0 field. This was performed utilizing the FSL FLIRT tool for rigid body affine transformations (21).

For phase processing, raw phase images were unwrapped in three-dimensions using a region-growing algorithm (22). A Fourier filtering process was then applied to remove background fields. First, a 3D, Gaussian, low-pass filter was applied to the Fourier transform of the unwrapped phase data (23). The Gaussian filter had the following functional form:

$$G(k_x,k_y,k_z) = e^{-(k_x^2+k_y^2+k_z^2)/2\sigma^2} \qquad [4.7]$$

The value of σ for the convolution kernel was set to 0.007 m^{-1}. This value was chosen to sufficiently remove background field contributions, while still preserving local frequency contrast between gray and white matter. A 3D inverse Fourier transform was then applied to the result of the Fourier domain multiplication to generate low-pass filtered, spatial domain data. Subtraction of this low pass filtered data from the original, unwrapped phase data produced a high pass filtered phase image.

After background filtering, the phase maps were fit using a weighted linear regression to yield the off-resonance frequency at each voxel, i.e. f_L (24). The linear regression was weighted by the phase noise variances.

4.3.5 Histological staining

For histological staining, brains were prepared for sectioning using a Leica RM2255 Microtome (Cryostat Microsystems, Wetzlar, Germany) in accordance with previously published methods (25). Sections were cut at a thickness of 5 μm and de-paraffinized before staining by heating at 50 °C. Every second slice was then stained with solochrome cyanine R (ScR) for myelin detection (25). The remaining slices were stained for iron using diaminobenzidine (DAB)-enhanced Perls stain (26).

The microscopy slides were digitized using a Zeiss Axio Optical Imager (Carl Zeiss AG, Jena, Germany) at 40× magnification. The digital images were then co-registered to the R_2^* maps using the FSL FLIRT registration tool (21). Subsequently, a value for optical density, $OD = -\log_{10}(I/I_o)$, was computed at each pixel, where I represents the image intensity for light passing through tissue and I_o represents the image intensity for light passing through a region of the slide where only the background level of staining was observed.

4.4 Results and Discussion

4.4.1 Imaging setup

Each of three rat brain samples was imaged using a multi-echo, gradient echo sequence with the medial fissure of the brain oriented at 18 different sampling angles relative to the main field of the magnet. Specifically, the brains were rotated to (i) eight unique angles of $n \times 45°$ ($n = 1 \ldots 8$) about the y-axis shown in Fig. 4.1c, as well as (ii) 10 additional angles chosen to produce an even sampling of the unit sphere. Reproducible rotations were achieved by using the sample holder shown in Fig. 4.1.

4.4.2 Orientation dependence of R_2^* in white matter

Fig. 4.2b illustrates the change in R_2^* as a function of the orientation of the four ROIs in the external capsule. Statistically significant changes in the white matter R_2^* for different brain orientations were observed at the confidence level of $p < 0.01$. This significance level was computed using a balanced one-way ANOVA for comparing independent samples containing mutually independent observations. The orientation-dependence of R_2^* was well fit by a $\sin(2\theta + \psi_0)$ relationship, with an average peak-to-peak variation of $\Delta R_2^* = 3.11 \pm 0.62\ s^{-1}$ (averaged across all external capsule ROIs in both hemispheres).

The linear and second-order R_2^* models of Eq. 4.1 and 4.4 were both fit to the R_2^* data in white matter. From fitting of the linear model, three parameters, C_1, C_0 and ψ_0, related to tissue composition (12) were then calculated. The full set of derived parameters for all rat brains are listed in Table 4.1. To generate those values, the linear model was fit to the data in each ROI of Fig. 4.2a for each brain sample. The fitted values for external capsule ROIs in the same hemisphere for the same sample were then averaged. A C_0

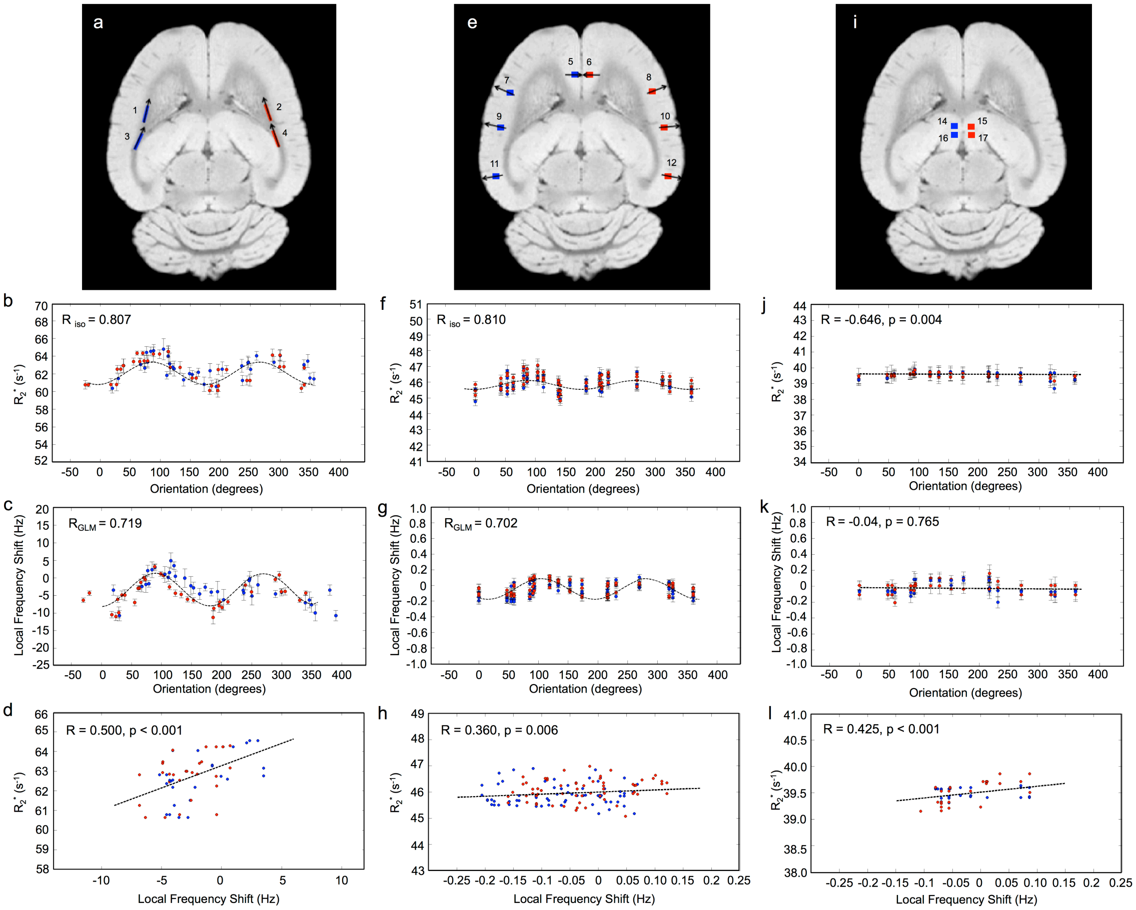

Figure 4.2: R$_2^*$ and f_L changes observed in gray and white matter as a function of fiber orientation relative to B$_0$ (for white matter) and surface normal orientation relative to B$_0$ (for gray matter). The regions of interest (ROIs) used for this analysis are displayed in Fig. 4.2 a, e and i. The ROIs used for analysis are overlaid on the second echo magnitude image with the medial fissure of the brain oriented parallel to B$_0$. The linear R$_2^*$ model is overlaid on Fig. 4.2b and f. The GL model fit is overlaid on Fig. 4.2c and g. Fig. 4.2j and k demonstrate the R$_2^*$ and f_L changes observed in the basal ganglia structures (lateral habenular nuclei) as a function of brain orientation. Fig. 4.2d, h and l demonstrate the linear relationships between the orientation dependence of R$_2^*$ and f_L in white and gray matter.

Table 4.1: Parameters derived from fitting the linear R_2^* model in external capsule white matter. Data is shown for each of the three brain samples (e.g. S1 = brain sample 1). Pearson correlation coefficients (r) are given in the right-most column of the table.

ROI Location	C_0 (s^{-1})	C_1 (s^{-1})	ψ_0 (°)	r
Left Brain, S1	59.89 ± 0.27	2.47 ± 0.37	11.74 ± 9.28	0.849
Right Brain, S1	59.36 ± 0.16	1.05 ± 0.23	32.58 ± 11.93	0.750
Left Brain, S2	64.23 ± 0.11	1.53 ± 0.11	22.84 ± 5.23	0.926
Right Brain, S2	64.71 ± 0.23	1.83 ± 0.32	21.73 ± 10.36	0.833
Left Brain, S3	62.14 ± 0.26	1.23 ± 0.39	15.23 ± 16.82	0.633
Right Brain, S3	62.47 ± 0.24	1.21 ± 0.32	21.39 ± 16.53	0.702

value of 62.13 ± 0.54 s^{-1} was observed when all external capsule white matter ROIs were averaged (n=3). A two-tailed Welch's t-test revealed no statistically significant difference ($p < 0.05$) between C_0 computed in the left and right brain external capsule.

The second-order model (Eq. 4.4) was also fit to the R_2^* orientation data in external capsule white matter. The derived parameters are listed in Table 4.2. The correlation coefficients in Table 4.2 demonstrate that the second-order model did not provide significantly improved fitting. For this reason, no further analysis was conducted with this higher-order model. Application of the higher-order model is difficult due to the confounding contributions of residual background fields (which may also have a $\sin(4\theta)$ dependence). In previous studies, SNR considerations revealed that large ROIs are necessary for observing the $\sin(4\theta)$ component. Such large ROIs are prone to introducing error in the measured R_2^* orientation dependence because the mean value of R_2^*

Table 4.2: Parameters derived from fitting the higher-order R_2^* model in external capsule white matter. Data is shown for each of the three brain samples (e.g. S1 = brain sample 1). Pearson correlation coefficients (r) are given in the right-most column of the table.

ROI Location	C_0 (s^{-1})	C_1 (s^{-1})	C_2 (s^{-1})	ψ_0 (°)	r
Left Brain, S1	59.90 ± 0.23	2.70 ± 0.33	0.88 ± 0.32	11.92 ± 5.08	0.825
Right Brain, S1	59.44 ± 0.16	1.52 ± 0.34	1.32 ± 0.52	6.56 ± 3.09	0.814
Left Brain, S2	64.45 ± 0.11	1.42 ± 0.17	-0.35 ± 0.14	13.10 ± 5.45	0.642
Right Brain, S2	64.69 ± 0.23	1.82 ± 0.31	-0.55 ± 0.45	22.64 ± 8.30	0.739
Left Brain, S3	63.02 ± 0.25	1.20 ± 0.38	0.51 ± 0.33	19.84 ± 14.32	0.885
Right Brain, S3	62.47 ± 0.24	1.18 ± 0.33	0.50 ± 0.44	11.50 ± 13.03	0.742

calculated from a large ROI is more sensitive to background fields. Such fields may vary over the length scale of the ROIs (12). Moreover, ROI-based analysis precludes voxel-wise interpretation of the anisotropic component, which is the ultimate goal of fitting the proposed second-order model.

4.4.3 Gray matter

Fig. 4.2f displays the changes in R_2^* of cortical gray matter as the brain was rotated. Gray matter R_2^* varied sinusoidally with surface normal orientation and was well fit by the linear model. The average trough-to-peak R_2^* variation in the cortex was $\Delta R_2^* = 0.94 \pm 0.32$ s^{-1} (averaged across all gray matter ROIs in both hemispheres). The parameters derived from fitting the linear model in gray matter are listed in Table 4.3.

Table 4.3: Results of the linear model fit to R_2^* in gray matter. Data is shown for each of the three brain samples (e.g. S1 = brain sample 1). Pearson correlation coefficients (r) are given in the right-most column of the table.

ROI Location	C_0 (s^{-1})	C_1 (s^{-1})	ψ_0 (°)	r
Left Brain, S1	46.36 ± 0.16	0.41 ± 0.16	18.02 ± 7.89	0.718
Right Brain, S1	45.10 ± 0.08	0.56 ± 0.07	20.50 ± 4.09	0.810
Left Brain, S2	46.88 ± 0.18	0.62 ± 0.15	13.52 ± 10.06	0.659
Right Brain, S2	47.11 ± 0.22	0.45 ± 0.27	24.19 ± 23.98	0.514
Left Brain, S3	46.68 ± 0.11	0.34 ± 0.10	31.85 ± 9.07	0.745
Right Brain, S3	46.57 ± 0.12	0.41 ± 0.09	43.16 ± 6.27	0.796

The parameter C_1 was used to estimate the trough-to-peak change in R_2^* R_2^* of sub-cortical gray matter did not display significant changes with brain orientation (Fig. 4.2i and j). The ROIs for this analysis were chosen in the sub-cortical, lateral-habenular nucleus. The notable difference between Fig. 4.2f (cortical gray matter) and j (deep gray matter) supports the premise that the orientation of penetrating cortical white matter fibers affects estimates of mono-exponential R_2^* in gray matter. Further, it identifies that changes in R_2^* with brain orientation in the largely isotropic structures (e.g. glial cells and astrocytes) of the basal ganglia are insignificant. It is not possible to completely exclude the contribution of coherently oriented microvasculature structures from the orientation-dependent R_2^* in cortical gray matter. Further work is necessary to more completely evaluate the quantitative contribution of cortical microvasculature to the orientation-dependent R_2^* signal.

4.4.4 Orientation-dependence of f_L in white matter

The relationship between f_L and white matter fiber orientation is illustrated in Fig. 4.2c. The mean trough-to-peak amplitude of the f_L shift was 7.2 ± 3.8 Hz. Fibers oriented perpendicular to the B_0 field had a positive frequency shift compared to those oriented parallel to the field. This trend is characteristic of any substance that is less diamagnetic than water. For instance, when myelin becomes less diamagnetic than water due to the fixation process (27, 28), this trend is observed. The results are consistent with previously observed effects of fixation on the magnetic susceptibility of myelin. The average $\Delta\chi_{GLModel}$ measured in external capsule white matter was 24.9 ± 2.25 ppb. This compares very well to previous values of 26 ppb in mouse white matter (6).

Fig. 4.2d identifies a linear relationship between the orientation dependencies of R_2^* and f_L in the oriented white matter fibers of the external capsule. The specific linear relation is given by $R_2^* = 0.23 \cdot f_L + 65.28$. The influence of R_2 is represented by the vertical offset term (65.28 s^{-1}), while a scaling constant which relates R_2' to f_L is given by the slope of the line (0.23). R_2' is influenced by the local frequency shift in a voxel for each tissue geometry and tissue composition (15). Breaking down the respective contributions of R_2 and R_2' in this manner may be useful in identifying subtle changes occurring in gray and white matter in the course of disease development. For instance, the early stages of demyelination which occur prior to removal of myelin debris in multiple sclerosis may preferentially effect R_2', while leaving R_2 unchanged.

4.4.5 Gray Matter

The relationship between cortical gray matter f_L and cortical fiber orientation is illustrated in Fig. 4.2g. The data was well fit by the GL model of Eq. 4.3 The average amplitude of gray matter f_L variation was 0.56 ± 0.13 Hz. Table 4.4 (right-most columns) shows the values of $\Delta\chi$ calculated from the GL model fit. The average $\Delta\chi_{GLModel}$ measured in gray matter was 4.5 ± 1.39 ppb. Since this represents the first attempt to measure susceptibility of gray matter using the GL model, there are no literature values with which to compare this measurement . However, the $\Delta\chi_{GLModel}$ can be compared to $\Delta\chi_{dipole}$, as performed in the section which follows. The ROIs used for this analysis of f_L orientation-dependence in cortical gray matter were chosen *with reference to* an adjacent intracortical vein but *not including* this vein. The ROIs were specifically selected using f_L maps to avoid including local fields from large intracortical veins which can modulate f_L (29).

Table 4.4: Parameters calculated from the GL model fit of f_L vs. cortical surface normal orientation (for gray matter) and f_L vs. principal fiber orientation (for white matter). The susceptibility values are referenced to the average susceptibility of surrounding gray matter. Data is shown for each of the three brain samples (e.g. S1 = brain sample 1). Pearson correlation coefficients (r) are given in the right-most column of the table.

	Gray Matter		**White Matter**	
ROI Location	**$\Delta\chi$ (ppb)**	**r**	**$\Delta\chi$ (ppb)**	**r**
Left Brain, S1	2.55 ± 1.60	0.871	25.13 ± 3.77	0.780
Right Brain, S1	4.04 ± 1.96	0.734	20.11 ± 2.64	0.759
Left Brain, S2	4.46 ± 2.91	0.736	31.40 ± 5.03	0.654
Right Brain, S2	6.92 ± 2.18	0.940	27.60 ± 7.03	0.783
Left Brain, S3	3.05 ± 2.28	0.670	23.88 ± 2.89	0.895
Right Brain, S3	5.94 ± 1.89	0.840	21.36 ± 8.80	0.601

The influence of capillary veins can also modulate an orientation-dependent f_L contrast in cortical gray matter (9). In (9) the influence of capillary deoxyhemoglobin on f_L in rat brain *in-vivo* was carefully measured and found to be negligible relative to the bulk gray/white f_L contrast (maximum Δf_L = 0.02 Hz for realistic values of oxygen saturation, Y = 0.7, and hematocrit, Hct = 0.4, in rat brain capillary). Close examination of our myelin-stained slides (see e.g. Fig. 4.5a) in the cortical ROIs, revealed the presence of striated myelin variation across the length of the cortex but no clear evidence of larger capillary veins. For these reasons, we believe that capillary-mediated f_L shifts negligibly contributed to the cortical gray matter orientation-dependent f_L variations observed in this study.

The orientation dependence of f_L was also evaluated in sub-cortical gray matter. Four ROIs were chosen in the left and right brain lateral habenular nuclei (Fig. 4.2i). No distinct orientation dependence for f_L (Fig. 4.2k) was observed. This result is similar to the orientation dependence of R_2^* in sub-cortical gray matter and distinct from f_L of *cortical gray matter* which does show a subtle orientation dependence (Fig. 4.2g). This indicates the local frequency shift is sensitive to cellular architectural differences in different gray matter regions.

Fig. 4.2h and l identify linear relationships between the orientation dependencies of R_2^* and f_L for cortical and sub-cortical gray matter. For cortical gray matter, $R_2^* = 0.82 \cdot f_L + 49.27$, while for sub-cortical gray matter, $R_2^* = 1.10 \cdot f_L + 39.51$. These linear relations identify the contribution of the local frequency shift to R_2^* through the R_2' value. Two scaling relations were found: $R_2' = 0.82 \cdot f_L$ for cortical gray matter and $R_2' = 1.10 \cdot f_L$ for sub-cortical gray matter. The scaling constant relating R_2' to f_L in cortical gray matter

(0.82) was 3.57 times larger than that of white matter (0.23). However, the mean amplitude of the f_L variation in white matter is approximately 20 times larger than that of cortical gray matter (Δf_L = 4 Hz for white matter, compared to Δf_L = 0.2 Hz for gray matter). Together, these factors indicate that the orientation-dependent, reversible component of the transverse relaxation rate ($R_2' = \text{constant} \cdot f_L$) is approximately 5.60 times larger in white matter as compared to gray matter (for the case of this fixed rat brain tissue). This R_2' difference is a function of the tissue microstructure because it is a function of both axonal density and fiber orientation dispersion inside a voxel (15).

The measurement of local frequency shift through unwrapping the phase, then, serves as an approximate alternative for measuring the orientation-dependent part of R_2' in gray matter. This may be useful for probing changes in microstructure of gray matter associated with disease.

4.4.6 Comparison of $\Delta\chi_{GLModel}$ to $\Delta\chi_{dipole}$ in white matter

The histograms in Fig. 4.3a and 3b compare $\Delta\chi_{GLModel}$ to $\Delta\chi_{dipole}$ for each sample in each hemisphere. Table 4.4 shows the white matter susceptibility values calculated from fitting the GL model and associated Pearson correlation values. A Welch's two-tailed t-test revealed that the GL model-derived and the inversion-calculated values of magnetic susceptibility in the external capsule were different ($p < 0.05$) in all cases, except for the right hemisphere of sample 3, where the mean value of $\Delta\chi_{GLModel}$ is still larger than that of $\Delta\chi_{dipole}$. The difference between these two measurements was, on average, 12.73 ± 2.91 ppb. This difference results from the fact that the GL model accounts for the geometry-induced frequency shift of cylindrical axons, whereas dipole fitting does not.

The magnitude of the isotropic component of the frequency shift in white matter is affected by formalin fixation. Recent research (30) conducted using excised rat brain

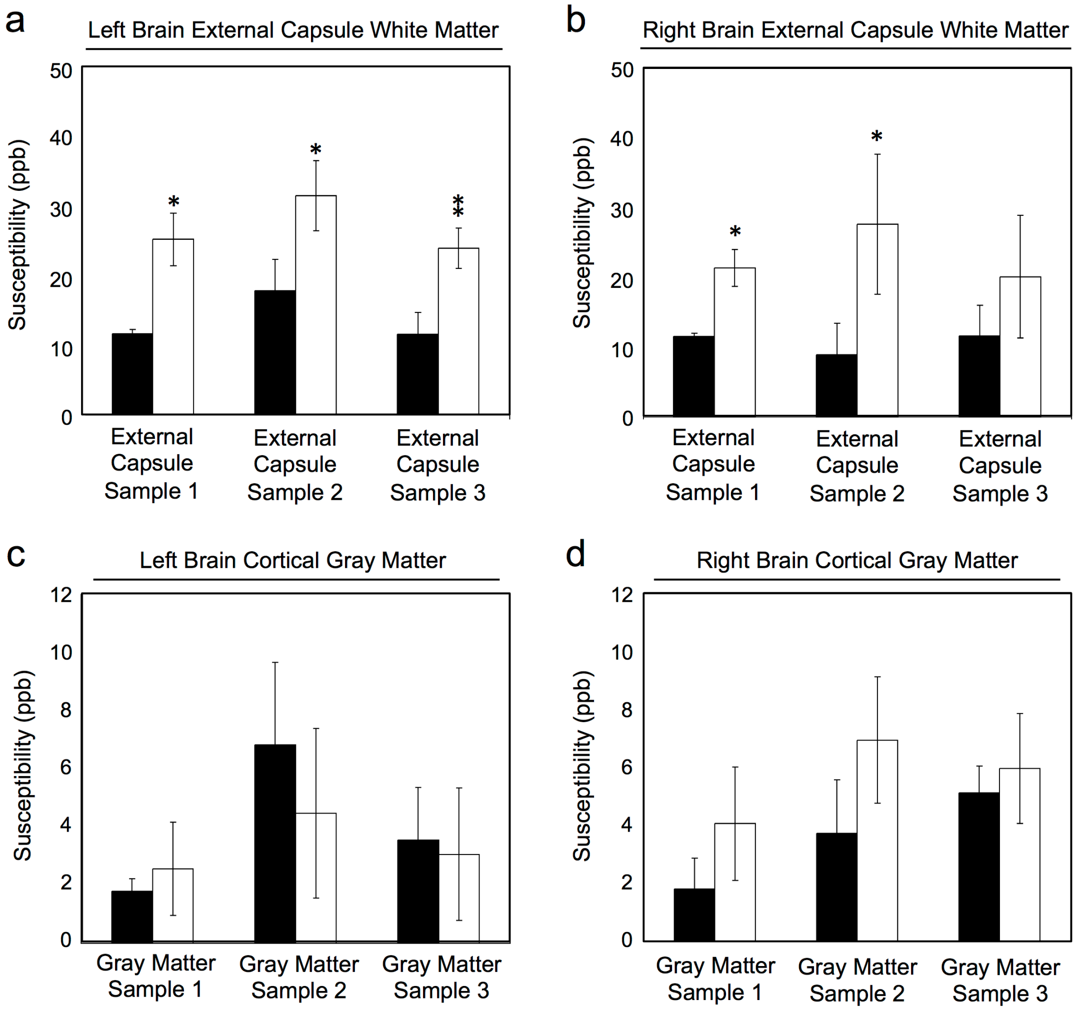

Figure 4.3: Comparison of $\Delta\chi_{dipole}$ (black bars) to $\Delta\chi_{GLModel}$ (white bars) for both white matter (Fig. 4.3a and b) and gray matter (Fig. 4.3c and d). All susceptibility values are in SI units of parts-per-billion (ppb) and have been referenced to the susceptibility of gray matter in an adjacent ROI. Separate comparisons were performed for left and right brain hemispheres. Error bars represent standard error of the mean. Statistical significance levels are defined as: * $p < 0.05$ and ** $p < 0.001$.

optic nerve embedded in water suggests that the *amplitude* of this isotropic frequency shift is increased (this is a diamagnetic shift) by a factor of approximately two, due to fixation. For this reason, the isotropic frequency shifts reported in our paper may be larger than those observed in fresh rat brain tissue.

The GL model does not account for susceptibility variations in white matter due to either chemical exchange or myelin bilayer anisotropy. Nevertheless, it is a useful model that can improve estimates of susceptibility, provided the fiber angle relative to B_0 is known. Interestingly, the difference of 12.73 ± 2.91 ppb between $\Delta\chi_{GLModel}$ and $\Delta\chi_{dipole}$ is on the order of the isotropic magnetic susceptibility of white matter recently calculated in mouse brain using susceptibility tensor imaging (13 ppb reported in reference (6)). These convergent results suggest that fitting the GL model to f_L measured at multiple brain orientations is a robust technique for quantifying the *isotropic, geometry-derived* component of susceptibility in white matter.

4.4.7 Gray matter

The histograms in Fig. 4.3c and d compare $\Delta\chi_{GLModel}$ to $\Delta\chi_{dipole}$ for gray matter in each rat brain hemisphere. The values computed for $\Delta\chi_{GLModel}$ and the associated Pearson correlation coefficients are listed in Table 4.4. A Welch's two-tailed t-test showed that $\Delta\chi_{GLModel}$ and $\Delta\chi_{dipole}$ are the same in all ROIs ($p > 0.05$ in all cases). This is not unexpected, since the observed variation in f_L with cortical fiber orientation in this study is very subtle (average amplitude of 0.56 ± 0.13 Hz for all ROIs examined).

From the above result, it can be inferred that, when gray matter susceptibility information is reconstructed using dipole inversion at standard clinical field strengths and resolutions of 1 mm^3 isotropic, it is unlikely the effects of cortical fiber geometry on $\Delta\chi$

will be significant. But this may not always be true for small animal studies. As susceptibility mapping methods improve and the achievable spatial resolution increases, the $\Delta\chi_{GLModel}$ value could serve as a standard for measurements of $\Delta\chi_{dipole}$ in cortical gray matter. Such a target value would facilitate analysis of convergence in regularized dipole inversion methods of quantitative susceptibility mapping.

4.4.8 Correlative Histology of MRI and Non-Haeme Iron in Rat Brain Basal Ganglia

Histological staining was performed to investigate the relationship between iron concentrations in rat brain tissue and the susceptibility contrast parameters (R_2^* and $\Delta\chi_{dipole}$). Currently, there is significant interest in using a combination of R_2^* and $\Delta\chi_{dipole}$ to assess none-haeme iron variations in human brain tissue (7, 26, 31). However, to date, most studies have performed correlations between MRI susceptibility parameters *in-vivo* and *ex-vivo* iron concentrations derived from literature (7). The quantitative relationship between iron concentration, as derived from OD of iron-stained slides, and both R_2^* and $\Delta\chi_{dipole}$ in the *same* tissue structure has not been examined.

To isolate the influence of iron on R_2^* and $\Delta\chi_{dipole,}$ ROIs were chosen in rat basal ganglia regions containing high iron concentration and low myelin content. The ROIs were centered on the left lateral-habenular and medio-dorsal nuclei (black boxes in Fig. 4.4a). A positive correlation ($R = 0.637$, $p < 0.001$, Fig. 4.4d) between R_2^* and iron OD was observed according to the linear relation $R_2^* = 158.05 \cdot OD + 36.72$. This relation is specific to the field strength used in this study (9.4 T) due to the dependence of R_2^* on field strength. A similar positive correlation was found between $\Delta\chi_{dipole}$ and iron OD ($R = 0.465$, $p < 0.001$, Fig. 4.4f) with the linear regression fit: $\Delta\chi_{dipole} = 674.05 \cdot OD - 79.3$. R_2^* was also plotted against corresponding $\Delta\chi_{dipole}$ on a voxel-by-voxel basis (Fig. 4.4b) to

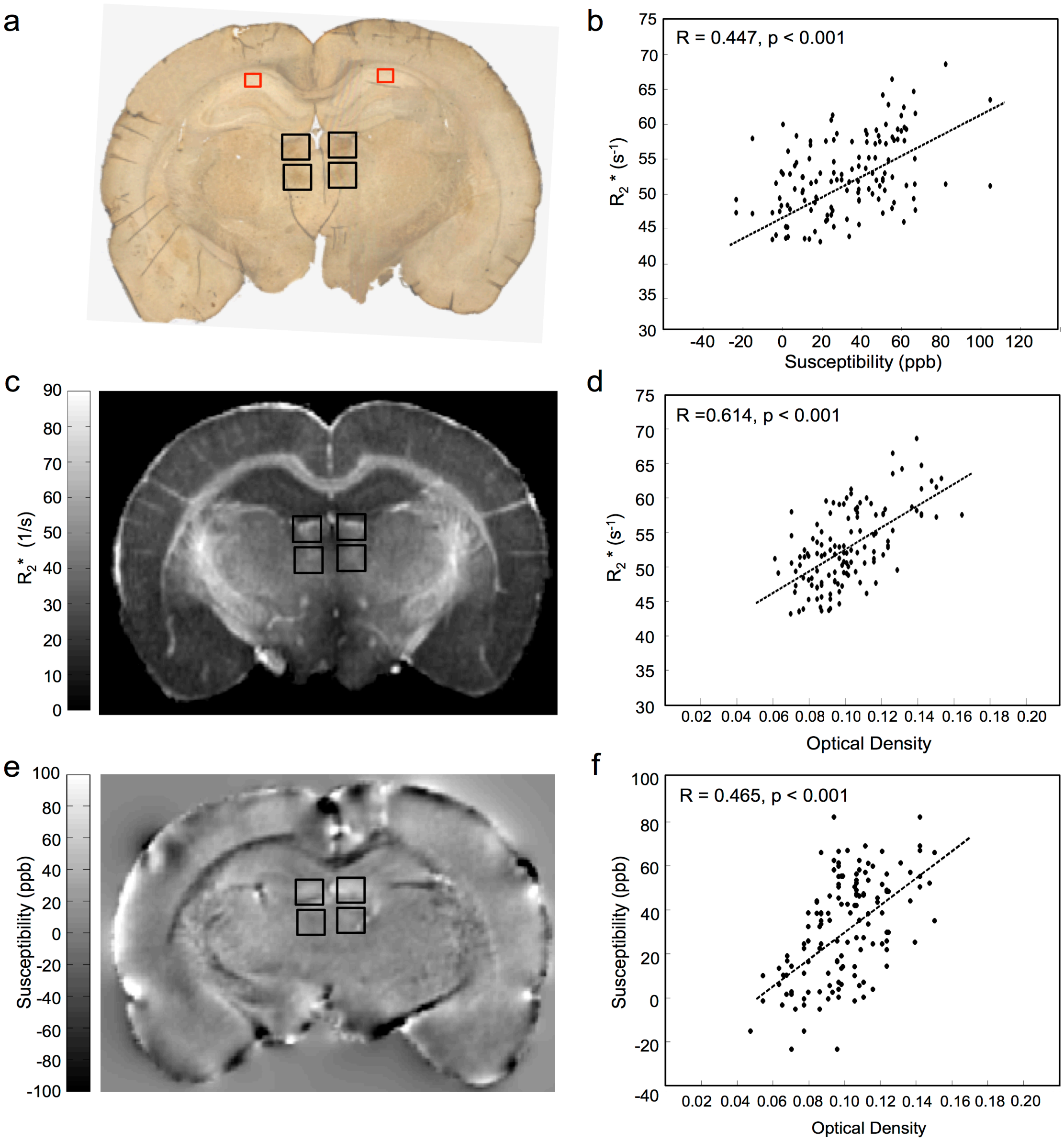

Figure 4.4: R_2^* and quantitative susceptibility values in the lateral-habenular and medio-dorsal nuclei (deep brain basal ganglia structures) of the rat brain positively correlate with Fe^{3+} density from DAB-enhanced Perls staining. (a) A representative coronal section of a rat brain stained with DAB-enhanced Perls is shown. Black boxes indicate the ROIs in which OD and quantitative MRI values were measured. ROIs include the right and left lateral-habenular nuclei and the right and left medio-dorsal nuclei. The corresponding coronal MRI sections of a rat brain are displayed in (c) for R_2^* (in units of 1/s) and (e) for quantitative susceptibility (in units of ppb). Figure 4b displays a positive linear correlation between R_2^* and $\Delta\chi_{dipole}$ in the rat basal ganglia. The correlation of R_2^* (d) or

$\Delta\chi_{dipole}$ (f) with OD measurements are also shown. Each data point represents a voxel from the chosen ROIs. The black dotted lines indicate the linear regression fit to the data. R and p values are indicated in the top left corner of the correlation plots.

derive a relationship between these parameters for Fe^{3+} iron at 9.4 T. The linear relation between R_2^* and $\Delta\chi_{dipole}$ was $R_2^* = 0.10 \cdot \Delta\chi_{dipole} + 49.59$, with $R = 0.447$ and $p < 0.001$. We observed a linear correlation between R_2^* and $\Delta\chi_{dipole}$ in the rat basal ganglia (Fig. 4.4b). In general, these two parameters need not be correlated (32); thus, this observation sheds some light on the underlying mechanisms governing these two quantities. Inter-voxel susceptibility differences can result in a positive or negative frequency shift between voxels without contributing to the R_2^* of these voxels, while increased intra-voxel susceptibility variation can lead to incoherent dephasing and increased R_2^* in a voxel. For the case of the basal ganglia, our data suggests that punctate non-haeme iron concentrations in the brain are accompanied by magnetic field inhomogeneities on the scale of the voxel, thus affecting both R_2^* and $\Delta\chi_{dipole}$.

4.4.9 Correlative Histology of MRI and Myelin Density in Rat Brain Major White Matter Regions

In Fig. 4.5, the effect of myelin density on C_0 and C_1 was examined. The specific ROIs used for this analysis are given by the black boxes in Fig. 4.5a and b. They include dense white matter regions of the corpus callosum, external capsule and internal capsule. C_0 and C_1 showed strong positive correlations with myelin OD (Fig. 4.5c and e). C_0 was correlated with myelin OD according to the relation $C_0 = 64.96 \cdot OD + 37.84$, with $R = 0.905$ and $p < 0.001$ (Fig. 4.5c). C_1 was correlated with myelin OD according to the relation $C_1 = 1.62 \cdot OD + 0.94$, with $R = 0.456$ and $p < 0.001$ (Fig. 4.5e). C_0 and C_1 were

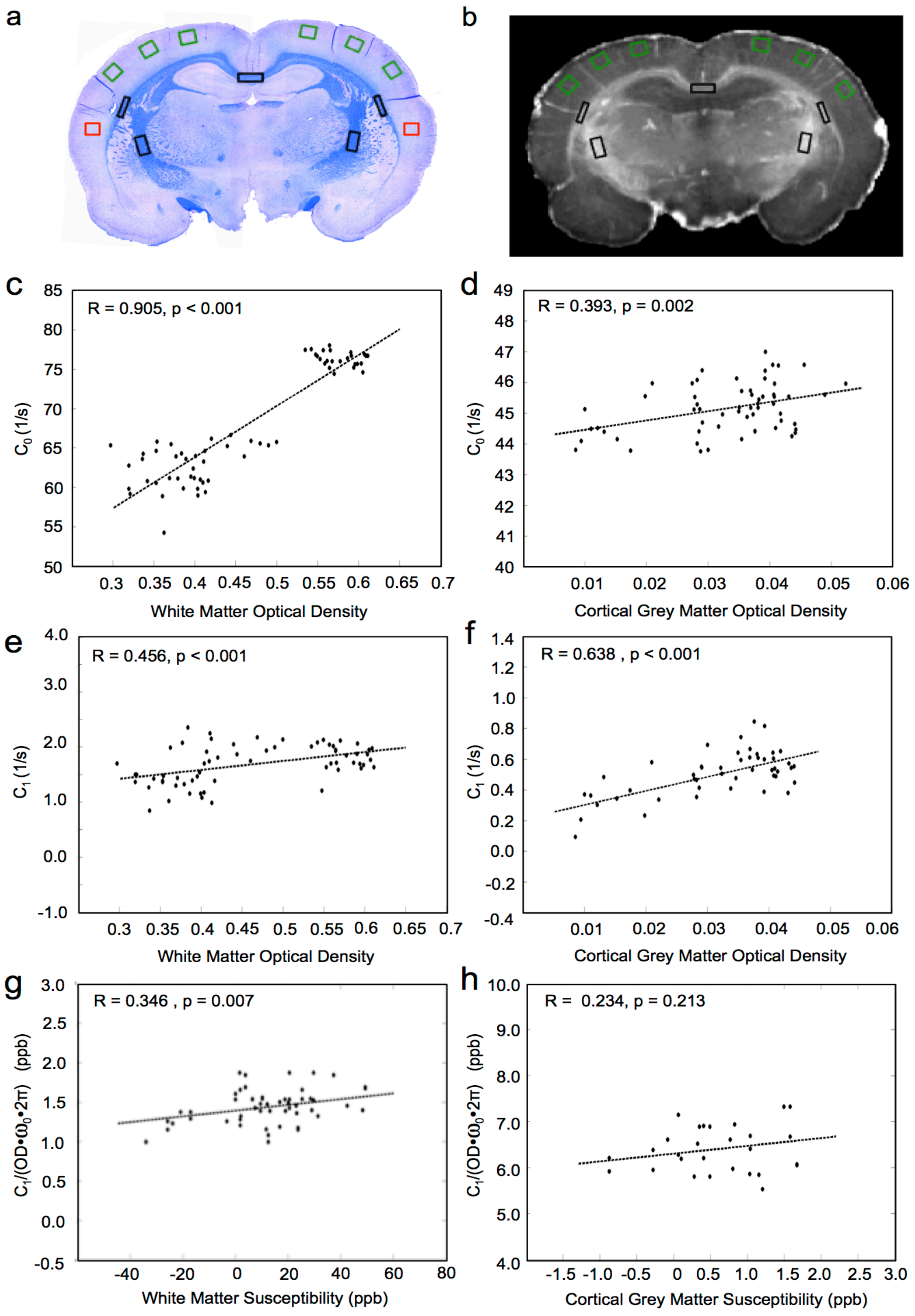

Figure 4.5: The constants, C_0 and C_1, derived from the linear R_2^* orientation model correlate positively with OD of solochrome cyanine-R staining for myelin in both major white matter tracts and cortical gray matter. (a) A representative coronal section of the rat brain stained for myelin. (b) R_2^* map corresponding to the myelin stain. Black boxes indicate the ROIs in which the OD of myelin, C_0 and C_1 were measured in white matter.

Green boxes indicate the ROIs in which the OD of myelin, C_0 and C_1 were measured in cortical gray matter. C_0 (c,d) and C_1 (e,f) correlated positively with the myelin OD in major white matter tracts and cortical gray matter. Each data point represents a voxel from the chosen ROIs. (g,h) Linear relations between the value of C_1, calculated from fitting the linear R_2^* model, and $\Delta\chi$, calculated from the GL model for both white (g) and gray (h) matter. C_1 and $\Delta\chi$ are related through Eq. 4.3. The OD was used as a surrogate for the volume fraction (ζ) of perturbers in these plots.

also computed in six ROIs lining the cortex (green boxes in Fig. 4.5a and b). C_0 and C_1 both demonstrated strong positive correlations with myelin OD in these regions (Fig. 4.5d and f). This supports our hypothesis that an orientation dependent R_2^* exists in the cortex and the source of this dependence is associated with cortical fibers.

It is noteworthy that R_2 (C_o) and R_2' (C_1) are affected in different ways by changes in myelin density. R_2 is governed by spin-spin interactions between neighbouring hydrogen atoms, while R_2' is mediated by mesoscopic magnetic field gradients both inside and between voxels. The linear relations derived from the plots in Fig. 4.5 can be used to independently estimate myelin concentration given either R_2 or R_2'. As well, they support the concept that myelin density and axonal geometry are two major factors governing R_2^* changes observed with changes in fiber orientation.

According to Eq. 4.3, the constant C_1, derived from fitting the linear model to the R_2^* orientation data, is a linear function of $\Delta\chi$. To test the validity of this model in both white and cortical gray matter, a value of $\Delta\chi$ was calculated in the black and green ROIs shown in Fig. 4.5a and b, using the GL model. The parameters C_1 and OD were then calculated in these ROIs. The OD value calculated in the ROIs was used as a measure of

C_1 and $\Delta\chi$. In white matter a significant linear correlation was observed, verifying that OD can serve as a surrogate marker for perturber volume fraction. However, in cortical gray matter the correlation was not significant, likely due to the poorer fitting of the GL model on a voxel-by-voxel basis in gray matter (as opposed to the case of a single mean value from an ROI shown in Fig. 4.2g). To the best of our knowledge, this is the first demonstration of the use of OD as a surrogate marker for volume fraction in white matter microstructure analysis, as well as the first demonstration of a relationship between R_2^* and $\Delta\chi$ based on the isotropic perturber model. These results suggest that, for white matter, the combined use of R_2^*, $\Delta\chi$ and OD derived from histochemical staining can enhance knowledge of underlying tissue composition.

4.5 Conclusion

This study demonstrates a significant orientation-dependence of R_2^* in both white and cortical gray matter that is a sinusoidal function of tissue orientation and a linear function of perturber volume fraction. The fitting coefficients, C_0 and C_1, calculated using the R_2^* cylindrical field perturber model, are linearly related to myelin density. For white matter, the isotropic perturber fraction, C_1 , is a linear function of the white matter susceptibility difference ($\Delta\chi$) relative to gray matter. This finding supports the premise that a major underlying source of the orientation dependence of R_2^* is the axonal geometry-derived susceptibility shift.

A comparative analysis of the orientation dependencies of R_2^* and f_L in matched tissue locations throughout the rat brains allowed calculation of scaling relations which quantify R_2' given f_L. Using these relations, the orientation-dependent, reversible component of the transverse relaxation rate ($R_2' =$ constant $\cdot f_L$) was found to be approximately 5.60 times larger in white matter compared to gray matter. Measuring such differences in R_2' in different brain tissues is a potential method for probing tissue microstructure, since R_2' is a function of the geometry-derived, frequency dispersion within a voxel. Equally relevant, the identification of optical density of myelin staining as a realistic surrogate for volume fraction in white and cortical gray matter may complement future studies relating biophysical models of the MRI signal to true underlying tissue composition.

The next chapter highlights a 7 T imaging study using whole-brain, quantitative $\Delta\chi$ and R_2^* mapping for simultaneous monitoring of iron deposition and demyelinating processes in MS patients.

4.6 References

1. Bouras, C., P. Giannakopoulos, P. F. Good, A. Hsu, P. R. Hof, and D. P. Perl. 1997. A laser microprobe mass analysis of brain aluminum and iron in dementia pugilistica: comparison with Alzheimer's disease. *Eur Neurol* 38: 53-58.
2. Chen, J. C., P. A. Hardy, W. Kucharczyk, M. Clauberg, J. G. Joshi, A. Vourlas, M. Dhar, and R. M. Henkelman. 1993. MR of human postmortem brain tissue: correlative study between T2 and assays of iron and ferritin in Parkinson and Huntington disease. *AJNR Am J Neuroradiol* 14: 275-281.
3. LeVine, S. M., M. J. Wulser, and S. G. Lynch. 1998. Iron quantification in cerebrospinal fluid. *Anal Biochem* 265: 74-78.
4. Sivanandam, T. M., and M. K. Thakur. 2012. Traumatic brain injury: a risk factor for Alzheimer's disease. *Neurosci Biobehav Rev* 36: 1376-1381.
5. Liu, C. 2010. Susceptibility tensor imaging. *Magn Reson Med* 63: 1471-1477.
6. Li, W., B. Wu, A. V. Avram, and C. Liu. 2012. Magnetic susceptibility anisotropy of human brain in vivo and its molecular underpinnings. *Neuroimage* 59: 2088-2097.
7. Schweser, F., K. Sommer, A. Deistung, and J. R. Reichenbach. 2012. Quantitative susceptibility mapping for investigating subtle susceptibility variations in the human brain. *Neuroimage* 62: 2083-2100.
8. Li, T. Q., P. van Gelderen, H. Merkle, L. Talagala, A. P. Koretsky, and J. Duyn. 2006. Extensive heterogeneity in white matter intensity in high-resolution T2*-weighted MRI of the human brain at 7.0 T. *Neuroimage* 32: 1032-1040.
9. Lee, J., Y. Hirano, M. Fukunaga, A. C. Silva, and J. H. Duyn. 2010. On the contribution of deoxy-hemoglobin to MRI gray-white matter phase contrast at high field. *Neuroimage* 49: 193-198.
10. Bender, B., and U. Klose. 2010. The in vivo influence of white matter fiber orientation towards B(0) on T2* in the human brain. *NMR Biomed* 23: 1071-1076.
11. Denk, C., E. Hernandez Torres, A. MacKay, and A. Rauscher. 2011. The influence of white matter fibre orientation on MR signal phase and decay. *NMR Biomed* 24: 246-252.

12. Lee, J., P. van Gelderen, L. W. Kuo, H. Merkle, A. C. Silva, and J. H. Duyn. 2011. T2*-based fiber orientation mapping. *Neuroimage* 57: 225-234.
13. He, X., and D. A. Yablonskiy. 2009. Biophysical mechanisms of phase contrast in gradient echo MRI. *Proc Natl Acad Sci U S A* 106: 13558-13563.
14. de Rochefort, L., T. Liu, B. Kressler, J. Liu, P. Spincemaille, V. Lebon, J. Wu, and Y. Wang. 2010. Quantitative susceptibility map reconstruction from MR phase data using bayesian regularization: validation and application to brain imaging. *Magn Reson Med* 63: 194-206.
15. Yablonskiy, D. A., and E. M. Haacke. 1994. Theory of NMR signal behavior in magnetically inhomogeneous tissues: the static dephasing regime. *Magn Reson Med* 32: 749-763.
16. Cohen-Adad, J., J. R. Polimeni, K. G. Helmer, T. Benner, J. A. McNab, L. L. Wald, B. R. Rosen, and C. Mainero. 2012. T(2)* mapping and B(0) orientation-dependence at 7 T reveal cyto- and myeloarchitecture organization of the human cortex. *Neuroimage* 60: 1006-1014.
17. Li, L., and J. S. Leigh. 2004. Quantifying arbitrary magnetic susceptibility distributions with MR. *Magn Reson Med* 51: 1077-1082.
18. de Rochefort, L., R. Brown, M. R. Prince, and Y. Wang. 2008. Quantitative MR susceptibility mapping using piece-wise constant regularized inversion of the magnetic field. *Magn Reson Med* 60: 1003-1009.
19. Klassen, L. M., and R. S. Menon. 2004. Robust automated shimming technique using arbitrary mapping acquisition parameters (RASTAMAP). *Magn Reson Med* 51: 881-887.
20. Yablonskiy, D. A., A. L. Sukstanskii, J. Luo, and X. Wang. 2012. Voxel spread function method for correction of magnetic field inhomogeneity effects in quantitative gradient-echo-based MRI. *Magn Reson Med*
21. Jenkinson, M., and S. Smith. 2001. A global optimisation method for robust affine registration of brain images. *Med Image Anal* 5: 143-156.
22. Abdul-Rahman, H. S., M. A. Gdeisat, D. R. Burton, M. J. Lalor, F. Lilley, and C. J. Moore. 2007. Fast and robust three-dimensional best path phase unwrapping algorithm. *Appl Opt* 46: 6623-6635.

23. Rauscher, A., M. Barth, J. R. Reichenbach, R. Stollberger, and E. Moser. 2003. Automated unwrapping of MR phase images applied to BOLD MR-venography at 3 Tesla. *J Magn Reson Imaging* 18: 175-180.
24. Kressler, B., L. de Rochefort, T. Liu, P. Spincemaille, Q. Jiang, and Y. Wang. 2010. Nonlinear regularization for per voxel estimation of magnetic susceptibility distributions from MRI field maps. *IEEE Trans Med Imaging* 29: 273-281.
25. Roscoe, W. A., M. E. Welsh, D. E. Carter, and S. J. Karlik. 2009. VEGF and angiogenesis in acute and chronic MOG((35-55)) peptide induced EAE. *J Neuroimmunol* 209: 6-15.
26. Fukunaga, M., T. Q. Li, P. van Gelderen, J. A. de Zwart, K. Shmueli, B. Yao, J. Lee, D. Maric, M. A. Aronova, G. Zhang, R. D. Leapman, J. F. Schenck, H. Merkle, and J. H. Duyn. 2010. Layer-specific variation of iron content in cerebral cortex as a source of MRI contrast. *Proc Natl Acad Sci U S A* 107: 3834-3839.
27. Liu, C., W. Li, G. A. Johnson, and B. Wu. 2011. High-field (9.4 T) MRI of brain dysmyelination by quantitative mapping of magnetic susceptibility. *Neuroimage* 56: 930-938.
28. Shepherd, T. M., P. E. Thelwall, G. J. Stanisz, and S. J. Blackband. 2009. Aldehyde fixative solutions alter the water relaxation and diffusion properties of nervous tissue. *Magn Reson Med* 62: 26-34.
29. Ogawa, S., T. M. Lee, A. R. Kay, and D. W. Tank. 1990. Brain magnetic resonance imaging with contrast dependent on blood oxygenation. *Proc Natl Acad Sci U S A* 87: 9868-9872.
30. Luo, J., X. He, and D. A. Yablonskiy. 2013. Magnetic susceptibility induced white matter MR signal frequency shifts-experimental comparison between Lorentzian sphere and generalized Lorentzian approaches. *Magn Reson Med*
31. Yao, B., T. Q. Li, P. Gelderen, K. Shmueli, J. A. de Zwart, and J. H. Duyn. 2009. Susceptibility contrast in high field MRI of human brain as a function of tissue iron content. *Neuroimage* 44: 1259-1266.
32. Deistung, A., A. Schafer, F. Schweser, U. Biedermann, R. Turner, and J. R. Reichenbach. 2013. Toward in vivo histology: a comparison of quantitative

susceptibility mapping (QSM) with magnitude-, phase-, and R2*-imaging at ultra-high magnetic field strength. *Neuroimage* 65: 299-314.

Chapter 5

Improved Identification of MS Disease-Relevant Changes in Gray and White Matter using Susceptibility-Based High Field MRI

To make a discovery is not necessarily the same as to understand a discovery.

– Abraham Pais, *Inward Bound: of Matter and Forces in the Physical World.*

5.1 Introduction

Conventional magnetic resonance imaging (MRI) measures of MS disease status, using the number and location of lesions in white matter (WM), have not correlated well with clinical symptoms (1) or demonstrated significant predictive power for determining disease progression (2). On the other hand, neuropathological studies have identified the following features as being strongly related to MS etiology and neurodegeneration: (i) changes in the chemical composition of myelin, (ii) axonal loss and (iii) accumulation of iron in brain regions affected by MS (3). Unfortunately, it has been difficult to quantify such neuropathological markers *in vivo* using standard MRI contrasts. The goal of this study was to explore the use of *quantitative susceptibility-based MRI* at 7T to identify characteristic regions suggestive of demyelination and increased iron deposition in MS patients and relate these measurements to patient disability.

For the purposes of this research, *quantitative susceptibility-based MRI* consists of the measurement of the apparent transverse relaxation rate ($R_2^* = 1/T_2^*$) and local Larmor frequency shift (LFS) using a straightforward multi-echo gradient echo (GRE) sequence. In brain tissue of MS patients, R_2^* values are affected by focal accumulation of iron, as well as by transient demyelination and remyelination (4, 5). For this reason, R_2^* has been proposed as a surrogate biomarker of disease severity (4). However, R_2^* maps can be inaccurate at tissue interfaces where steep magnetic field gradients exist (6). Additionally, elevated concentrations of iron and myelin both increase R_2^*. This makes it difficult to attribute R_2^* increases to either iron accumulation or re-myelination alone. Disentangling the contributions of myelin and iron to the R_2^* signal would make it more valuable for understanding MS pathophysiology.

Quantitative susceptibility (QS) mapping (7-9) is an MRI technique complementary to R_2^* mapping that calculates tissue volume magnetic susceptibility from the LFS. It advantageously removes the effects of confounding non-local magnetic fields created by tissue boundaries. It is also differentially sensitive to myelin and iron (8). Increases in myelin content (e.g. due to re-myelination) negatively shift the absolute QS value because myelin is diamagnetic, while increases in iron content positively shift QS because iron is paramagnetic (8). Because of this differential sensitivity, QS has the potential to more precisely monitor disease-related changes in MS. Accordingly, the combined use of QS and R_2^* obtained from multi-echo GRE MRI has been advocated as a comprehensive method for studying brain tissue composition due to the differing sensitivities of QS and R_2^* to iron and myelin (10, 11).

In this work, we used QS mapping in conjunction with mono-exponential, R_2^*-based relaxometry to evaluate voxel-wise WM changes associated with MS disease severity. Such a multi-parametric comparison in white matter has not previously been performed. As a natural extension of the WM analysis, QS and R_2^* were also used for monitoring iron accumulation in sub-cortical gray matter. Localization and quantification of sub-cortical iron has the potential to enhance our understanding of the progressive loss of neuronal function, motor deficits and cognitive impairment which accompany MS disease progression (12).

In summary, the purpose of this study was to evaluate the potential of quantitative susceptibility (QS) and apparent transverse relaxation rate (R_2^*) mapping as surrogate biomarkers of clinically relevant, age-adjusted demyelination and iron deposition in MS patients.

5.2 Materials and Methods

5.2.1 Imaging Protocol

Informed consent was obtained from a population of 25 patients with either CIS (four patients) or RRMS (21 patients), as well as from 15 healthy, age and gender-matched volunteers. The research was approved by the Research Ethics Board of the University of Western Ontario. All subjects gave written consent. The mean age of patients was 37.3, with ages ranging from 21 to 45. Patients had Kurtze Extended Disability Status Scale scores (EDSS scores) extending from 0 to 6. All CIS patients had an EDSS of 0. Further information characterizing the patient cohort is listed in Table 5.1 on the following page.

Imaging was performed on a 7 T neuro-specialized MRI scanner (Agilent Technologies, Santa Clara, California) using 16 parallel transmit channels and either 16 or 23 channel receive coils. Main external magnetic field (B_0) (13) and radiofrequency transmit field (B_1^+) shimming (14) were performed on each subject prior to acquisition of the following sequences: (i) a 3D multi-echo GRE sequence ($0.5 \times 0.5 \times 1.25$ mm^3 resolution) to obtain susceptibility-based images (ii) a T_2-weighted, magnetization-prepared (MP)-FLAIR sequence ($1.0 \times 1.0 \times 1.0$ mm^3 resolution) for lesion delineation

Table 5.1: Demographic and Clinical Data. Demographic and clinical data for study cohort. All data showing error estimates represent mean ± standard deviation. P-values were computed using a Wilcoxon rank-sum test.

Variable	Controls	Patients	p-value
Number of Participants	15	25	Not applicable
Gender, M/F	3/15	7/25	Not applicable
Age	36.4 ± 6.42	37.3 ± 6.10	0.58 (Not significant)
EDSS score *	Not applicable	1.70 (0 – 6)	Not applicable

* Data in parentheses represent range of EDSS scores for all patients.

(total scan time = 12 minutes and 1 second) and (iii) a T_1-weighted, MPRAGE acquisition ($1.0 \times 1.0 \times 1.0$ mm^3 resolution) for anatomical reference and use in tissue segmentation (total scan time = 5 minutes and 45 seconds). The multi-echo GRE sequence used the following pulse sequence parameters: axial orientation, TR=40 ms, TE_1=3.77 ms, number of echoes=6, echo spacing=4.09 ms, flip angle=13°, matrix dimensions=380×340× 102, GRAPPA acceleration factor R=2 along the first phase encode direction, in-plane resolution=0.5x0.5 mm^2, slice thickness=1.25 mm, field of view=190×170×128 mm^3, total scan time=15 minutes and 55 seconds.

5.2.2 Calculation of R_2^*, LFS and QS maps

From the multi-echo GRE magnitude data, mono-exponential R_2^* maps were generated using an interior-point, least squares fitting routine in Matlab (R2013, The MathWorks, Natwick, MA, USA). To compensate for the influence of confounding background field gradients, T_2^*-weighted magnitude data was corrected prior to least squares fitting according to the method outlined in references (6, 15).

For QS map calculation, raw phase images were temporally unwrapped along the echo train. Residual phase wraps were then removed in three-dimensions using a region-growing algorithm (16). Background field contributions were subsequently removed by employing the sophisticated harmonic artifact reduction for phase data method (SHARP) (8) with a spherical kernel radius of 7 mm to generate an LFS map. The QS map was calculated from the LFS map by employing a k-space based, regularized inversion (7) in Matlab. Accurate and reproducible QS mapping requires calculation of QS values relative to a common reference structure. In this study, bilateral regions of interest (ROIs) in frontal deep WM were used as a reference tissue (10).

5.2.3 Voxel-Wise Statistical Analysis

Voxel-wise statistical analysis was performed by registering the calculated R_2^* and QS maps to the MNI-1 mm template using a non-linear registration with the FNIRT tool in FSL (17). A general, additive linear model (GLM) was then applied to evaluate statistically significant changes in both R_2^* and QS on the voxel level. Age was included as a covariate in the linear model. No interactions between covariates or between groups were modeled. This was done because the inclusion of interactions in the GLM did not result in improved fitting of the model to the data. All resulting Z-score maps were corrected for multiple comparisons using the false-detection-rate technique (18) and thresholded to include Z-scores with $|Z| > 1.0$. This threshold was applied to allow for the visualization of both trends and statistically significant regions in the Z-score maps. The GLM analysis was also performed with WM lesions removed in order to identify statistically significant reductions in QS and R_2^* in the *normal-appearing white matter (NAWM)* of MS patients. All image analysis was performed by MRI physics researchers experienced in neuroimaging and blinded to the clinical information (D.R. and R.S.M., with 5 and 33 years respectively, of experience in clinical neuroimaging).

To investigate the correspondence between damaged WM in the Z-score maps and MS clinical disease status, the volume of damaged WM satisfying a $Z<-2.0$ criterion for both QS and R_2^* was correlated with three MS clinical metrics: extended disability status scale (EDSS), time since CIS diagnosis (TSCIS) and time since MS diagnosis (TSMS). This correlation analysis was performed with and without lesions. The $Z<-2.0$ criterion has recently been used in the segmentation of "diseased-appearing white matter" from 2D, T_2-weighted FLAIR images of MS patients acquired at 1.5T (19). Also, to explore possible associations between volume of tissue with elevated iron content and MS clinical status, the volume of sub-cortical gray matter with $Z>2.0$ was correlated with the three MS clinical metrics.

As well as using VBM, we evaluated changes in *mean value* of R_2^* and QS in four sub-cortical GM structures (caudate nucleus, putamen, globus pallidus and thalamus). Specifically, the strength of univariate correlations between the R_2^* and QS signals and the three MS clinical metrics were quantified. To account for age-dependent increases in these parameters, the effect of age was subtracted from R_2^* and QS data by calculating the slope in a regression of both R_2^* and QS as a function of age for the controls. All sub-cortical gray matter segmentation masks were calculated using the FSL FIRST tool (17) applied to the bias-field corrected, T_1-weighted magnitude images.

5.3 Results

5.3.1 Representative 7 T Image Contrasts and Template Registration Examples

Representative images from a 45-year old, female RRMS patient with an EDSS score of 1.0 are displayed in Figure 5.1 on the following page. The top row (A-C) shows the anatomical contrasts: (A) T_1-weighted MPRAGE, (B) T_2-weighted MP-FLAIR and (C) T_2^*-weighted magnitude image. The bottom row (D-F) presents susceptibility-based MRI contrasts of the same slice: (D) R_2^*, (E) LFS and (F) QS maps. Magnified views of a periventricular WM lesion are displayed in red boxes in the top right hand corner of each figure. The magnified views of the lesion in Figure 5.1D - F identify deoxyhemoglobin-bearing vessels, hyperintense on the R_2^*-map and hypointense on the LFS map. These are not visible on the T_1- or T_2-weighted contrasts. Also visible within the lesion are uniquely heterogeneous regions of decreased R_2^* and increased LFS, representing possible edema or demyelination.

Examples of group-averaged, R_2^*, LFS and QS maps registered to the MNI-1 mm template space are presented in Figure 5.2 on page 94. The yellow arrows in Figures 5.2A and B point to slices through the caudate and globus pallidus where increased R_2^* is visible in the group-averaged patient maps compared to corresponding control maps. The red arrows in Figures 5.2E and F identify areas with reduced absolute values of QS in the optic radiations of the group-averaged control maps compared to corresponding slices in MS patients.

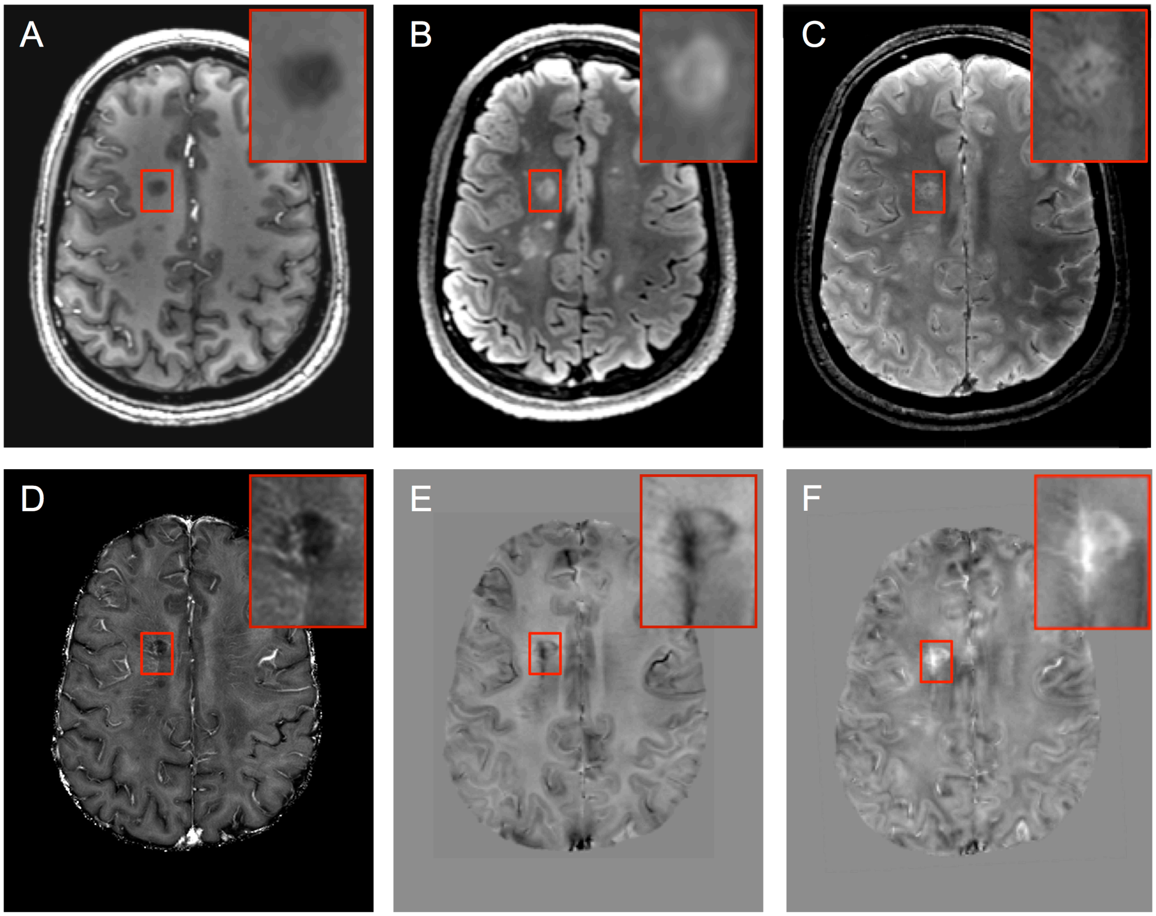

Figure 5.1: Representative MR image contrasts employed in this study. MR images corresponding to one slice from a 45-year old RRMS patient with an EDSS score of 1.0. Top row: (A) T_1-weighted MPRAGE, (B) T_2-weighted MP-FLAIR contrasts and (C) a T_2^*-weighted magnitude image. Bottom row: (D) R_2^*, (E) LFS and (F) QS maps. Magnified views of a lesion in the periventricular white matter are shown in the red boxes (top right hand corner of each figure).

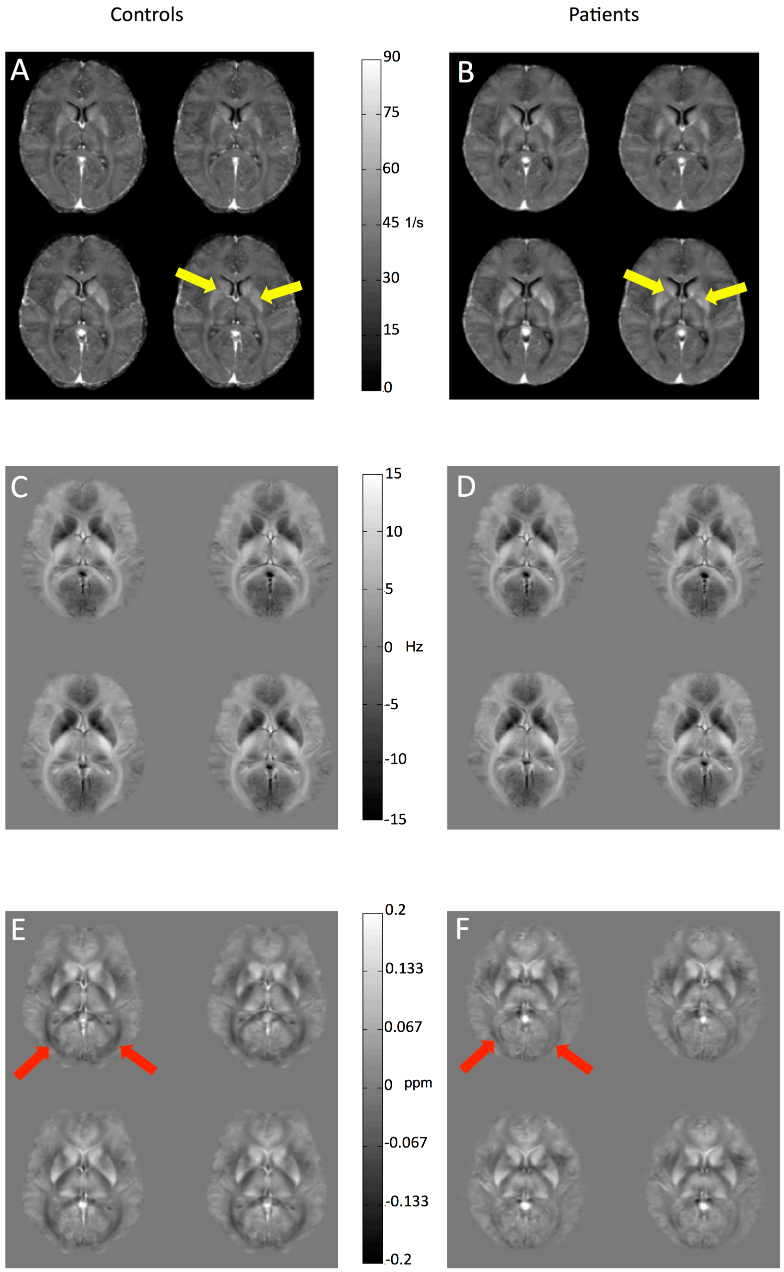

Figure 5.2: Standard space, susceptibility-based MRI contrasts. Examples of non-linearly registered R_2^* (Figure 5.2A and B), LFS (Figure 5.2C and D) and QS (Figure 5.2E and F) group-averaged maps in the MNI-1 mm template space. Yellow arrows in Figure 5.2A and B identify regions of the caudate nucleus and globus pallidus of MS patients with increased R_2^*. Red arrows in Figure 5.2E and F display regions with reduced absolute values of QS in the optic radiations of the group-averaged control maps compared to corresponding slices in MS patients.

5.3.2 ROI-based analysis of R_2^* and QS in sub-cortical gray matter structures

Representative sub-cortical nuclei segmentations overlaid on the T_1-weighted image are displayed in figure 5.3. Figure 5.4 on the following page illustrates that, in all the segmented sub-cortical gray matter structures, both age-corrected R_2^* and QS showed very strong positive correlations ($p<0.01$) with EDSS. The mean R_2^* value in the thalamus and caudate displayed the strongest linear correlations (R=0.57). For QS mapping, the globus pallidus exhibited the strongest linear correlation with EDSS (R=0.70). Each data point in Figure 5.4 represents the mean value of R_2^* or QS in a particular sub-cortical gray matter structure. Separate data points are plotted for the left and right brain hemispheres, while the red crosses correspond to the mean values of the control group.

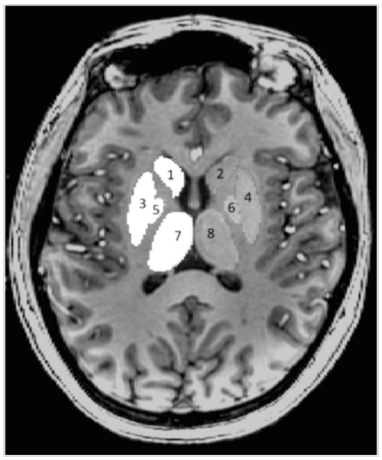

Figure 5.3: Sub-cortical nuclei segmentations overlaid on the T_1-weighted image. Labels for the left side of the brain are coloured white, while labels for the right side are coloured gray. Segmentation masks are shown for left and right brain caudate (1 and 2), putamen (3 and 4), globus pallidus (5 and 6), and thalamus (7 and 8). Segmentation masks which bled into the ventricles were removed by thresholding of R_2^* and QS maps.

Table 5.2 on page 97 compares group mean values of R_2^* and QS in sub-cortical gray matter to those of controls. The mean R_2^* of patients increased relative to controls in all structures, with the exception of the globus pallidus. The most significant increase in R_2^* was observed in the putamen ($p<0.001$, $\Delta R_2^* = 3.80 \pm 0.74$ 1/s). The mean QS value was also increased compared to controls at the level $p<0.008$ and below.

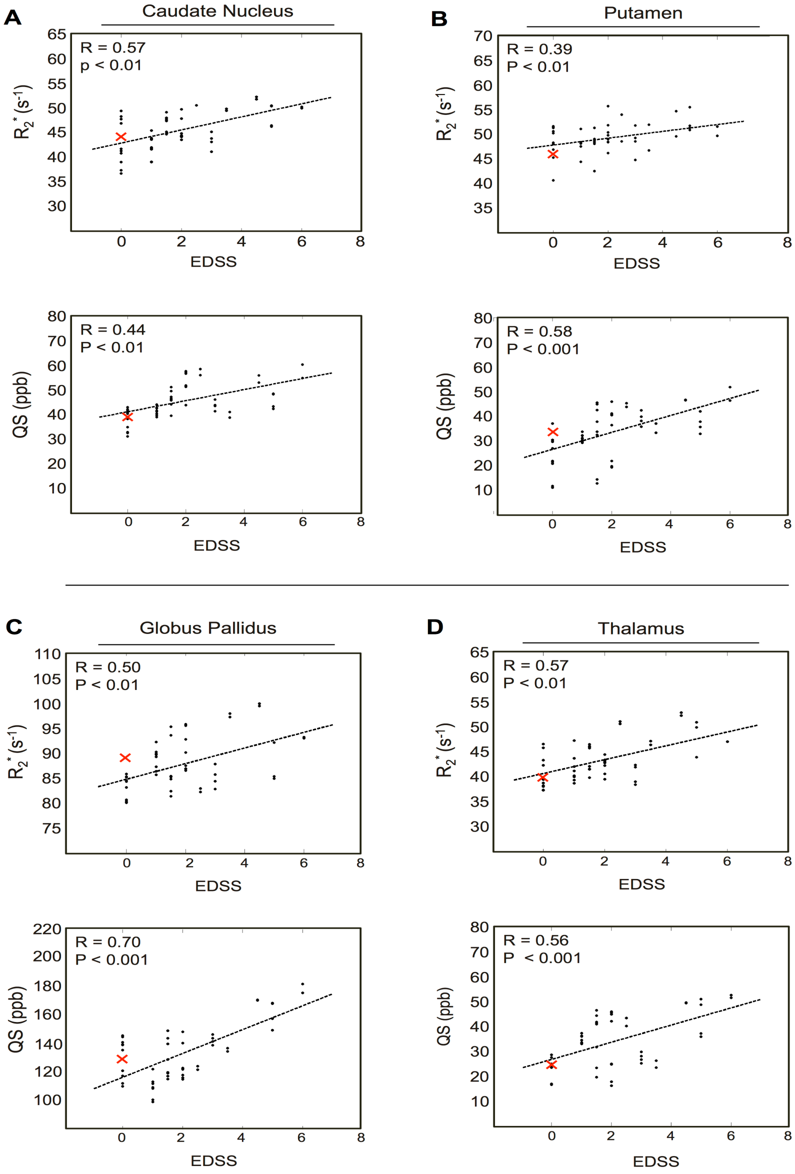

Figure 5.4: Scatter plots of R_2^* and quantitative volume magnetic susceptibility in MS patients with respect to Expanded Disability Status Scale (EDSS). Each data point represents the mean value of the quantitative MRI parameter inside one of the following structures: (A) caudate nucleus, (B) putamen , (C) globus pallidus and (D)

thalamus. A separate data point is displayed for each hemisphere in each patient. The red lines represent the mean values of the control group.

The most significant increases in sub-cortical QS were found in the thalamus ($p<0.001$, $\Delta QS = 11.47 \pm 4.54$ ppb) and globus pallidus ($p<0.001$, $\Delta QS = 13.02 \pm 5.09$ ppb).

Table 5.3 on page 100 compares the strength of univariate correlations between sub-cortical R_2^* and QS and the three MS clinical metrics (EDSS, TSCIS and TSMS). Sub-cortical gray matter R_2^* and QS most strongly predicted EDSS. However, associations with TSCIS were found for R_2^* of the caudate ($R=0.40$, $p<0.01$) and globus pallidus ($R=0.47$, $p<0.001$), as well as for QS in the putamen ($R=0.38$, $p<0.01$) , globus pallidus ($R=0.42$, $p<0.01$) and thalamus ($R=0.47$, $p<0.031$). TSMS was independently predicted by R_2^* of the globus pallidus ($R=0.39$, $p<0.01$), as well as by QS of the putamen ($R=0.35$, $p=0.01$) and thalamus ($R=0.30$, $p=0.04$).

Table 5.2: Sub-Cortical Gray Matter Mean Values of Susceptibility-Based MRI Parameters Compared to Controls. Mean quantitative R_2^* and susceptibility in the sub-cortical GM regions of MS patients compared to healthy, age and gender-matched controls. All values are mean ± standard error.

Sub-cortical GM Structure	Controls	Patients	p-value
Caudate R_2^* (1/s)	44.52 ± 2.30	46.93 ± 0.79	0.001
Putamen R_2^* (1/s)	46.31 ± 0.43	50.11 ± 0.60	< 0.001
Globus Pallidus R_2^* (1/s)	89.88 ± 1.47	90.65 ± 1.18	0.31
Thalamus R_2^* (1/s)	39.32 ± 1.73	43.55 ± 0.81	0.004
Caudate QS (ppb)	39.71 ± 2.36	45.43 ± 1.44	0.003
Putamen QS (ppb)	33.65 ± 1.01	42.14 ± 2.07	0.008
Globus Pallidus QS (ppb)	128.49 ± 2.73	141.51 ± 4.30	< 0.001
Thalamus QS (ppb)	25.85 ± 4.03	37.32 ± 2.10	< 0.001

5.3.3 Voxel-wise analysis for evaluating differences in QS and R_2^* in MS patients compared to controls

Figure 5.5 on the following page displays axial-plane, R_2^*-based, Z-score maps at the level of the sub-cortical gray matter (Figure 5.5A-C), supratentorial brain (Figure 5.5D-F) and cortical WM (Figure 5.5G-I). Positive Z-scores (orange/red/yellow areas) in sub-cortical gray matter suggest elevated non-haeme iron in patients compared to controls (10, 20). Blue colours represent brain regions with significantly ($Z<-1.0$) reduced R_2^* in white matter lesions. Green colours represent brain regions of patient NAWM with significantly reduced R_2^* suggestive of pre-lesional demyelination. Reduced R_2^* in WM could also be caused by decreased non-haeme iron in glial cells (21) or by a reduced overall metabolic demand for oxygen in the capillaries of damaged WM (22). If present, either of these effects would lead to a slight overestimation of the demyelination response we observed in our R_2^*-based Z-score maps. An alternative hypothesis, which is supported by recent MRI studies of reduced cerebral blood flow in MS (23, 24), is that slower blood flow and concomitantly increased oxygen exchange in capillaries could result in increased R_2^* in WM. If this effect were present, the demyelination effect we observe would be underestimated (section 5.3.3 is continued on page 100).

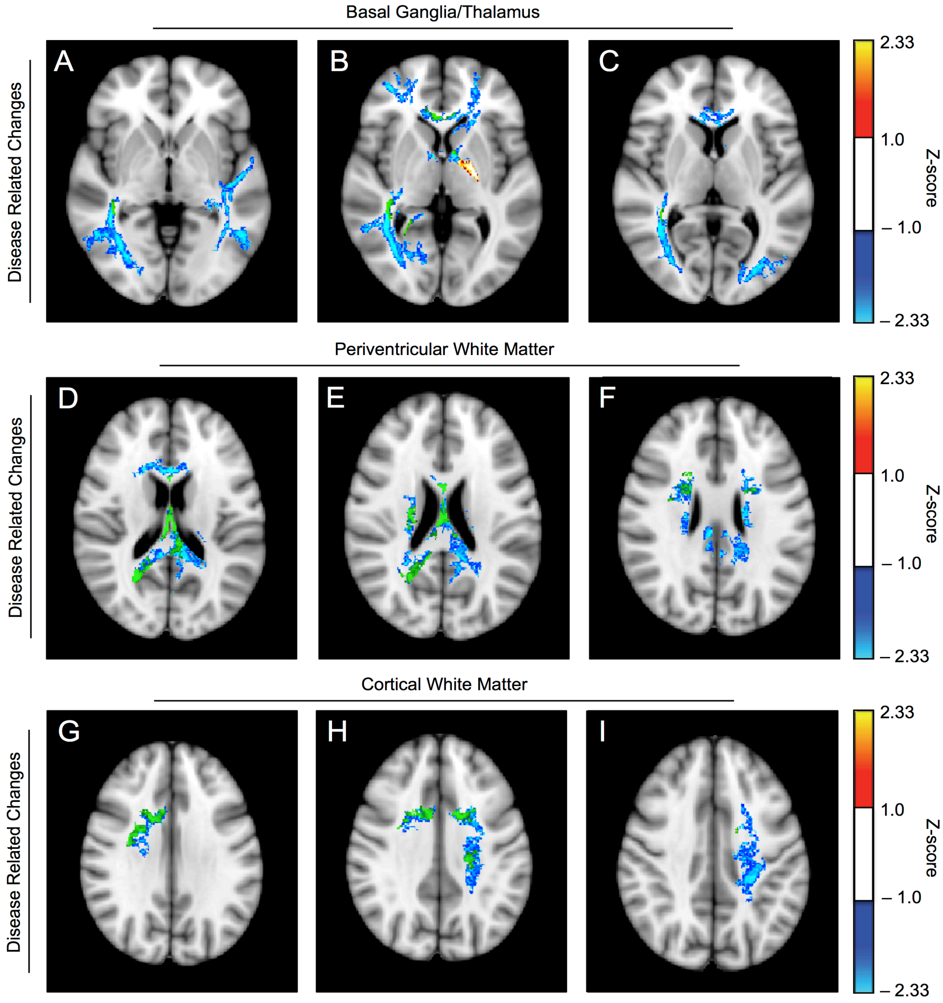

Figure 5.5: R_2^*-based, axial Z-score maps. R_2^*-based, axial Z-score maps derived from generalized linear model analysis of 25 patients compared to 15 age-matched controls. Blue colours represent brain regions with significantly reduced R_2^* ($Z<-2.0$) in lesioned tissue of patients compared to controls. Green colours represent brain regions of patient normal-appearing white matter (NAWM) with significantly reduced R_2^* ($Z<-2.0$) compared to controls. Red/orange areas with positive Z-scores indicate brain regions where patients have higher R_2^* ($Z > 2.0$) than age-matched controls. (**A-C)** are three representative slices through the sub-cortical GM, **(D-F)** are three representative slices through the periventricular white matter and **(G-I)** are three representative slices through the cortical white matter. All Z-score maps were corrected for multiple comparisons using the false-detection-rate technique with a significance threshold of 0.1.

Table 5.3: Correlations between susceptibility-based MRI parameters and clinical metrics. Pearson linear correlation between *mean* MRI-derived susceptibility parameters in sub-cortical gray matter and MS clinical metrics (time since CIS diagnosis = TSCIS, time since MS diagnosis = TSMS). The MRI susceptibility parameters were corrected for age-related increases in iron. Data in parentheses are P values.

MRI-Derived Parameter	EDSS	TSCIS	TSMS	Age
Caudate R_2^* (1/s)	0.57 (< 0.01)	0.40 (< 0.01)	0.19 (0.18)	0.37 (0.05)
Putamen R_2^* (1/s)	0.39 (< 0.01)	0.21 (0.14)	0.03 (0.86)	0.48 (0.01)
Globus Pallidus R_2^* (1/s)	0.50 (< 0.01)	0.47 (< 0.001)	0.39 (< 0.01)	0.52 (< 0.01)
Thalamus R_2^* (1/s)	0.57 (< 0.01)	0.20 (0.15)	0.06 (0.69)	0.25 (0.21)
Caudate QS (ppb)	0.44 (< 0.01)	0.17 (0.24)	0.06 (0.70)	0.19 (0.32)
Putamen QS (ppb)	0.58 (< 0.001)	0.38 (< 0.01)	0.35 (0.01)	0.39 (0.03)
Globus Pallidus QS (ppb)	0.70 (< 0.001)	0.42 (< 0.01)	0.21 (0.14)	0.59 (< 0.001)
Thalamus QS (ppb)	0.56 (< 0.001)	0.47 (< 0.001)	0.30 (0.04)	0.28 (0.23)

Due to the somewhat conflicting findings in the literature, it is not entirely clear which direction the white matter venous R_2^* should shift in MS due to the BOLD effect. However, we can make an informed estimate of the *amplitude* of the BOLD-mediated R_2^* changes by referring to the work of Jochimsen et al. (25). Using Monte-Carlo simulations to model T_2^* relaxation in cerebral venous vasculature, Jochminsen demonstrated that, for typical white matter vessels with radii of 4 – 32 μm, R_2^* changes due to hypercapnia (which approximates the 'hypometabolic' state observed in MS) are expected to be on the order of 0.2 s^{-1}. Such changes are very small compared to the average R_2^* difference in white matter we observed between MS patients and controls (5.95 ± 0.73 s^{-1} ; including lesions). Based on this estimate, the BOLD-mediated venous R_2^* changes are not believed to have significantly affected our results.

Two additional factors, derived from the existing literature, suggest the changes we observed in the R_2^*-based Z-score maps can be attributed to demyelination. First, the patterns of negative Z-scores follow the major WM bundles in the same manner as voxel-wise maps obtained from myelin-water fraction (MWF) (19, 26) and diffusion-weighted fractional anisotropy (FA) (27) measurements in MS patients. Since MWF and FA are principally sensitive to myelin structure in WM (not iron), these similar patterns point to myelin as the major biological source of the reduced R_2^*. Secondly, there is mounting evidence from post-mortem histochemical staining of both healthy (28) and MS NAWM (29) that phospholipid bilayer components are the major source of disseminated signal decreases observed on transverse relaxometry-based (R_2^* and R_2) MRI.

The damage to NAWM (green areas) occupies a subset of the total (lesion + NAWM) WM damage. It is localized to the genu, body and splenium of the corpus callosum, as well as to the optic radiations and periventricular WM. NAWM damage is also clearly observed in the cortical WM. Although age was included as a covariate, no significant, voxel-level age effects for R_2^* were observed at a false-detection rate threshold of 0.1.

Figure 5.6 demonstrates axial-plane, QS-based Z-score maps through the mid-brain (Figure 5.6A-C), supratentorial brain (Figure 5.6D-F) and cortical WM (Figure 5.6G-I). Since myelin is a diamagnetic perturber which negatively shifts raw QS values (i.e. heavily myelinated tracts are more diamagnetic), demyelination results in a decrease in the QS values relative to frontal WM. Blue areas in Figure 5.6 represent lesioned tissue, while green areas represent damage to NAWM. In Figure 5.6D and E, significantly ($Z<-1.0$) reduced Z-scores are visible in the genu and splenium of the corpus callosum adjacent to the ventricles. In the superior cortical WM (Figure 5.6G-I), disseminated regions of reduced Z-score are identified along the midline of the brain. As was the case for the R_2^*-based Z-score maps, the NAWM damage highlighted in green occupies a subset of the total damage. The total volume of NAWM damage with Z<-2.0 for QS was significantly larger than that observed for R_2^*: the mean (per patient) NAWM damaged volume from QS was 2126 mm^3 but only 175 mm^3 from R_2^*. This suggests that, for our chosen gradient echo scan parameters, QS may be more sensitive to the full extent of NAWM damage which precedes lesion formation in MS patients.

Bilateral, statistically significant *increases* in the QS of patients were observed at the level Z>2.0 in the globus pallidus and putamen in Figure 5.6A and B. Such increases were not seen on the corresponding R_2^*-based maps, suggesting QS was prefentially sensitive to MS pathology-related iron accumulation in these areas. Figure 5.6B and C also reveal evidence of statistically significant increases in QS values in the thalamus, with a particular localization of high Z scores in the pulvinar nucleus.

Figure 5.7 shows axial-plane, Z-score maps illustrating the change in QS as a function of *patient age*. Blue areas indicate regions of significant QS *decrease* as a function of age, while orange/red areas represent regions of significant QS *increase* as a function of age. WM lesions were not found to be co-localized with age-dependent QS reductions. Figure 5.7A-C demonstrate that QS increases significantly (Z>2.0) with age in the anterior portion of the globus pallidus in MS patients. Increases in QS with age are visible in the anterior section of the putamen. Figure 5.7D-I also delineate bilateral decreases in QS with age in the periventricular WM of the centrum semiovale in MS patients.

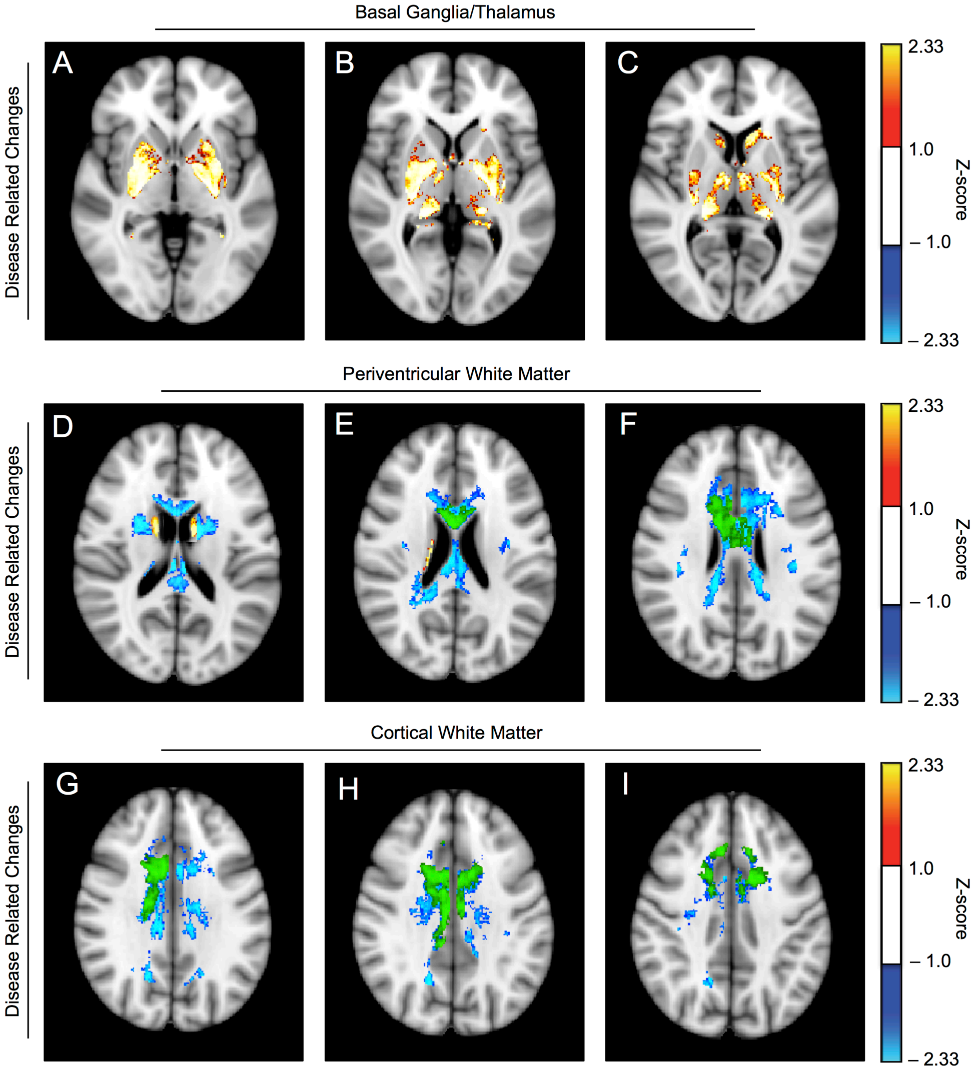

Figure 5.6: QS-based, axial Z-score maps. QS-based, axial Z-score maps derived from generalized linear model analysis of 25 patients compared to 15 age-matched controls. Blue colours represent regions of significantly reduced QS ($Z<-2.0$) in lesioned tissue of patients compared to controls. Green colours represent regions of patient NAWM with significantly reduced QS ($Z<-2.0$) compared to controls. Red/orange areas with positive Z-scores indicate brain regions where patients have higher QS ($Z > 2.0$) compared to age-matched controls. **(A-C)** shows increased Z-scores in the sub-cortical GM structures. **(D-F)** display reduced Z-scores in the periventricular white matter. G-I displays decreased QS in cortical white matter (blue colours).

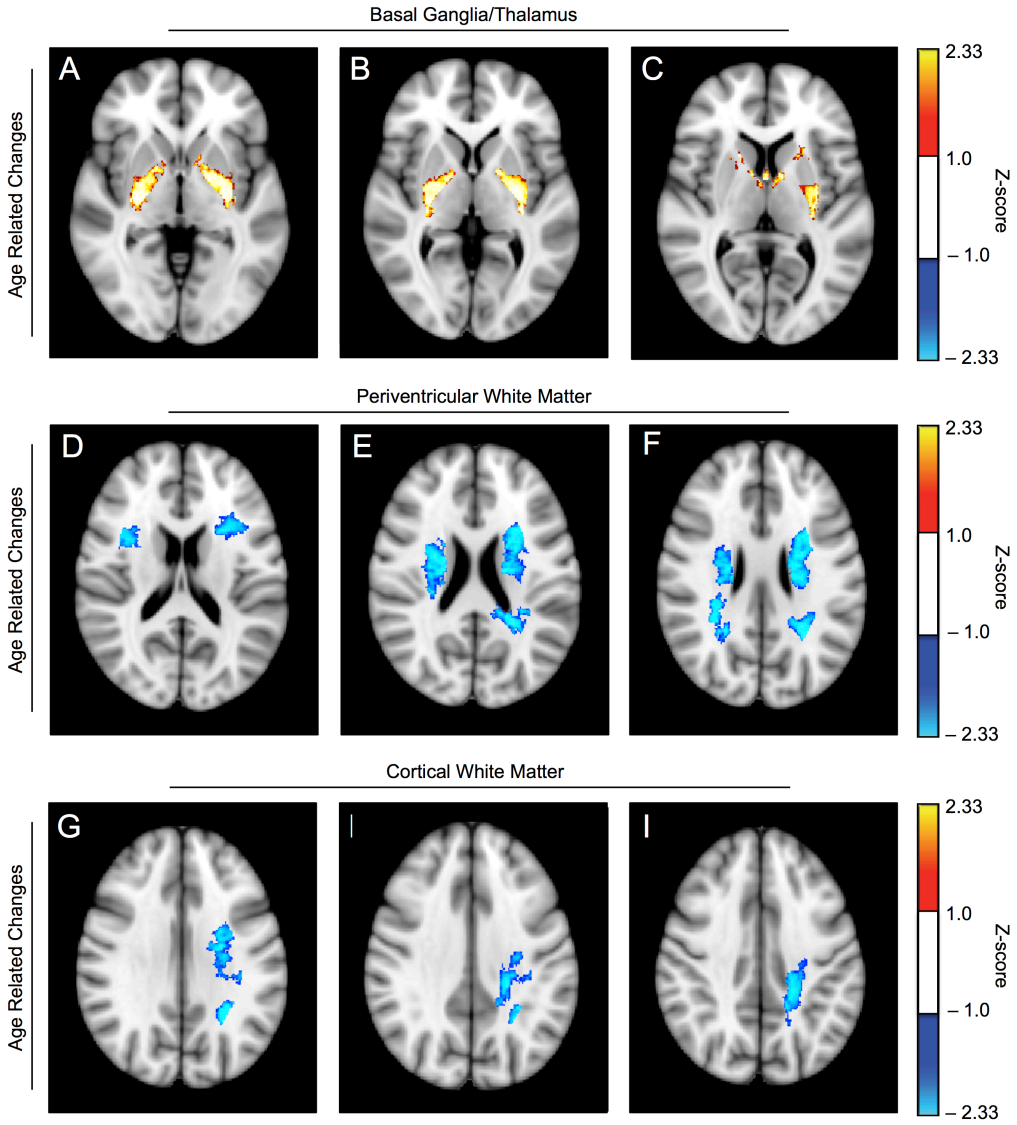

Figure 5.7: Changes in relative magnetic susceptibility *as a function of age*. These Z-score maps were derived by including age as a covariate in the generalized linear model statistical analysis. Blue colours represent brain regions with significantly reduced QS ($Z<-2.0$) in NAWM of patients as a function of age. Red/orange colours represent brain regions with significantly increased QS ($Z > 2.0$) in patients as a function of age. (**A-C**) are three representative slices through the sub-cortical GM, **(D-F)** are three representative slices through the periventricular white matter and **(G-I)** are three representative slices through the cortical white matter.

5.3.4 Relationships Between QS and R_2^*–Based Z-score Maps and Clinical Disability

The strength of univariate correlation between the volume of damaged WM (defined by a $Z<-2.0$ criterion) and EDSS is presented in Figure 5.8 and the corresponding list of correlations with clinical metrics is recorded in Table 5.4 on page 107. Each data point in Figure 5.8 represents a single patient, while red and blue points represent R_2^* and QS-based Z-score correlations respectively. Figure 5.8A displays the correlation between total damaged WM volume (lesional + NAWM with $Z<-2.0$) and EDSS. QS damaged WM volume correlated with EDSS at the level $p=0.02$ with $R=0.46$. However, R_2^* damaged WM volume did not increase with higher EDSS ($R=0.04$, $p>0.01$). Figure 5.8B shows the same correlations with WM lesions removed. The volume of QS damaged WM again correlated with EDSS ($R=0.39$, $p=0.05$) but the corresponding volume for R_2^* ($R=0.12$, $p>0.01$) did not. The volume of damaged WM did not correlate with TSCIS or TSMS for either QS and R_2^*. However, the EDSS score was independently predicted by the volume of sub-cortical gray matter tissue in QS-based Z-score maps with $Z>2.0$.

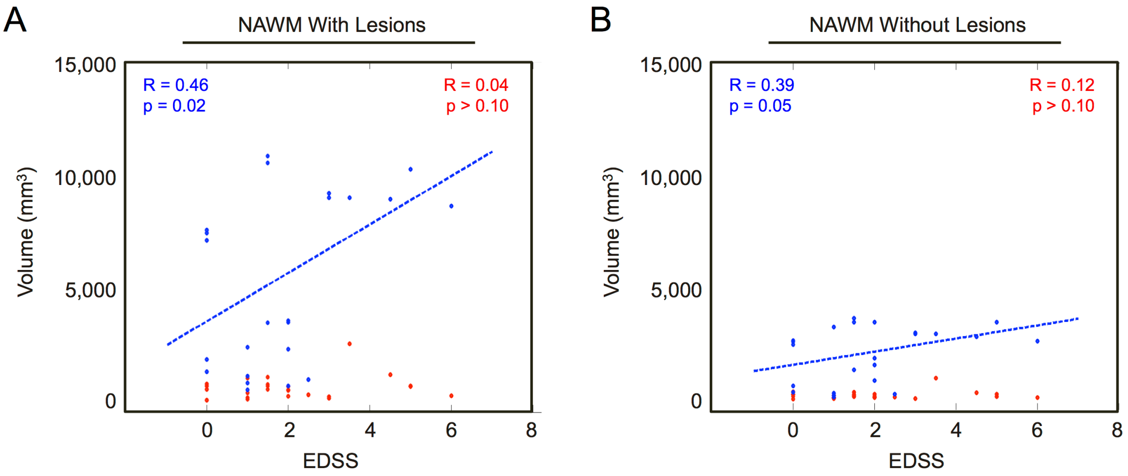

Figure 5.8: Relationship between volume occupied by significant negative Z-scores and EDSS. Relationship between the volume occupied by significant negative Z-scores (as defined by a Z<-2.0 criterion) and EDSS. Each point represents a single MS patient. Data is shown with lesions **(A)** and without lesions **(B)**. Red and blue points represent R_2^* and QS-based Z-score correlations with EDSS respectively. Only the number of significant voxels measured by QS correlated with EDSS.

5.4 Discussion

In this paper we examined both R_2^* and QS mapping of whole brain MS patient white matter compared to age and gender matched controls using voxel-wise analysis in a standard template space. By doing so, we demonstrated that computation of the susceptibility contrasts obtained with gradient echo MRI is an effective method for quantifying demyelination-related changes in NAWM of MS patient brain. A significant feature of combined R_2^* and QS mapping is that a single scan can be used to simultaneously identify iron accumulation in sub-cortical gray matter and demyelination in major white matter areas. The 'clinico-radiological' paradox associated with MS (30) suggests that lesion number and total lesion volume in white matter obtained from standard imaging are not predictive of clinical disease status. However in this work, with

QS-based Z score maps, EDSS was independently predicted using the volume of damaged white matter analysis. We also identified clinically relevant correlations between mean QS and R_2^* in individual sub-cortical gray matter structures of MS patients and EDSS, TSMS and TSCIS. The finding that group-averaged, mean sub-cortical QS values exhibited more pronounced statistical differences compared to R_2^* maps for the iron-bearing globus pallidus and putamen supports the specific use of QS as an improved surrogate biomarker of iron accumulation in MS.

Table 5.4: Relationships between volume of tissue occupied by significant voxels in R_2^* and QS-based Z-score maps and clinical metrics. Pearson linear correlation between the tissue volume occupied by significant Z-score voxels (either significantly positive, $Z > 2.0$, for sub-cortical gray matter or significantly negative, $Z<-2.0$, for white matter) and clinical metrics of MS. Data in parentheses are P values, time since MS diagnosis is abbreviated as TSMS, time since CIS diagnosis is abbreviated as TSCIS.

Volume of Significantly Affected MS Tissue	**EDSS**	**TSCIS**	**TSMS**	**Age**
Sub-Cortical Gray Matter, R_2^*	0.26 (0.22)	0.01 (0.99)	-0.18 (0.39)	0.27 (0.18)
White Matter R_2^*	0.04 (0.84)	0.21 (0.32)	-0.08 (0.67)	-0.13 (0.53)
White Matter R_2^* Without Lesions	0.12 (0.56)	0.22 (0.29)	-0.05 (0.81)	-0.10 (0.64)
Sub-Cortical Gray Matter QS	0.52 (< 0.01)	0.26 (0.19)	0.22 (0.29)	0.50 (0.01)
White Matter QS	0.46 (0.02)	0.23 (0.27)	0.21 (0.32)	0.30 (0.14)
White Matter QS Without Lesions	0.39 (0.05)	0.16 (0.43)	0.18 (0.39)	0.25 (0.23)
T_2 Lesion Load	0.17 (0.61)	0.65 (0.03)	0.09 (0.79)	-0.11 (0.74)

In white matter, the correlation of QS negative Z-score volume (R=0.46, p=0.02, blue dots) with EDSS contrasted with the lack of correlation for R_2^* (R=0.04 , p>0.10, red dots). This may reflect a greater specificity of QS to WM damage. One possible source of this increased specificity is that QS is more directly related to myelin composition because it reflects the degree to which myelin becomes magnetized when exposed to the main field. In contrast, increased *intra-voxel* susceptibility variation leads to incoherent dephasing which constitutes the main source of increased R_2^*.

In a previous study, Langkammer et al. (31) demonstrated that QS was more sensitive than R_2^* in monitoring iron accumulation in sub-cortical nuclei of patients with CIS and MS. Elevated iron levels were also observed in clinically-definite MS patients compared to those with CIS. However, voxel-wise analysis was not performed. Nor did the aforementioned study examine clinical correlations with TSMS and TSCIS. In population studies, voxel-wise analysis can be very useful in assessing differences in specific brain locations between patients and controls. For this reason, we believe our findings have identified a new, viable analysis avenue for QS mapping of MS. For example, our results showed high positive Z-scores in the QS-based maps in the thalamus, with notably high values in the pulvinar nucleus. This result supports findings of a previous study by Lebel et al. (32) which noted the pulvinar demonstrated the largest percent change of all sub-cortical gray matter structures in MRI phase measurements. It further suggests iron accumulation in the thalamus is visible at the voxel level when using group analysis with 7T susceptibility mapping. The accumulation of iron in the thalamus may play a significant role in thalamic atrophy which has recently been associated with conversion to clinically definite MS (33).

The patterns of reduced R_2^* in our Z-score maps are consistent with a previous voxel-wise analysis which applied MWF to visualize pathological demyelination in

NAWM of primary progressive MS (PPMS) patients (26). The asymmetric decreases in the R_2^*-based Z-score maps in the left hemisphere optic radiations are consistent with asymmetric patterns of demyelination in the optic tract observed in CIS (30), MS (34) and in related demyelinating disorders such as progressive multifocal leukoencephalopathy (35). The particular pattern of the asymmetric negative Z-scores we observed, however, is likely a group-average effect specific to our limited patient cohort. It is not believed to be a common trend across all MS disease sub-types and patient cohorts. The voxel-level, *age-related* decreases in our QS-based Z-score maps have not been previously reported and were not observed in controls. Larger-scale clinical studies of MS have independently confirmed that age, as well as duration of disease, correlate with worsening clinical symptoms (36-38). Our voxel-wise QS results, combined with the aforementioned clinical data, suggest there is a meaningful contribution of age to demyelination. With this in mind, *age-adjusted* EDSS or *age-adjusted* TSMS as proposed in reference (36) may constitute more precise metrics for monitoring MS progression compared to the standard, non age-adjusted measures. The detection of age-related demyelination using QS, but not R_2^*, implies age-related myelin loss is more closely linked to magnetic susceptibility properties which govern QS (39) than to nuclear relaxation of hydrogen nuclei probed by R_2^*.

There are several limitations associated with our study. First, no MRI data was collected from the spinal cord because the 7T neuroimaging scanner employed for this work does not permit spinal cord imaging. Quantitative MRI of the spinal cord using magnetization transfer ratio and diffusion-weighted MRI has previously identified correlations with disability that reflect underlying damage to the central nervous system

(40). It follows that a future direction for related research should involve correlating susceptibility-based changes observed in the spinal cord at 1.5 or 3T with those observed in the brain at 7T. Additionally, the underlying biophysical sources of the combined QS and R_2^* contrast in MS still require further investigation using combined MRI and post-mortem histopathological validation. Our results and the work of others (36-38) seem to support myelin as the dominant contributor to the QS signal in NAWM. However, further research is necessary to quantify the additional influence of iron dysregulation due to oligodendrocyte apoptosis and macrophage activation (21, 39) on the susceptibility contrasts in MS NAWM.

The relatively small size of our patient cohort is another limitation to this study. The statistically significant differences in the quantitative MRI parameters reported here should be verified in future work using a larger cohort of MS patients. Overall, our findings suggest susceptibility-based MRI would be useful for longitudinal monitoring of demyelination and remyelination in RRMS.

5.5 Conclusion

QS and R_2^* maps acquired using standard GRE MRI identify demyelination and iron accumulation in MS which correlate strongly with clinical disability. Using this information may allow earlier administration of therapies and monitoring of MS pathology *in-vivo*. Voxel-wise QS, rather than R_2^*, was preferentially sensitive to monitoring NAWM demyelination and sub-cortical iron accumulation *in-vivo*. The volume of damaged white matter tissue identified by QS was predictive of EDSS. The sensitivity of both QS and R_2^* mapping to *total white matter* (lesions + NAWM) damage suggests these quantitative contrasts may be useful for long term monitoring of demyelination and remyelination in MS.

The sixth and final chapter briefly summarizes the research carried out for this thesis. It also suggests ways of extending this research, emphasizing both technical developments and clinical applications.

5.6 References

1. Rudick RA, Lee JC, Nakamura K, Fisher E. Gray matter atrophy correlates with MS disability progression measured with MSFC but not EDSS. J Neurol Sci. 2009;282:106-111.
2. Moraal B, Pohl C, Uitdehaag BM et al. Magnetic resonance imaging predictors of conversion to multiple sclerosis in the BENEFIT study. Arch Neurol. 2009;66:1345-1352.
3. LeVine SM. Iron deposits in multiple sclerosis and Alzheimer's disease brains. Brain Res. 1997;760:298-303.
4. Khalil M, Langkammer C, Ropele S et al. Determinants of brain iron in multiple sclerosis: a quantitative 3T MRI study. Neurology. 2011;77:1691-1697.
5. Khalil M, Enzinger C, Langkammer C et al. Quantitative assessment of brain iron by R2* relaxometry in patients with clinically isolated syndrome and relapsing–remitting multiple sclerosis. Multiple Sclerosis. 2009;15:1048-1054.
6. Fernandez-Seara MA, Wehrli FW. Postprocessing technique to correct for background gradients in image-based R*(2) measurements. Magn Reson Med. 2000;44:358-366.
7. de Rochefort L, Liu T, Kressler B et al. Quantitative susceptibility map reconstruction from MR phase data using bayesian regularization: validation and application to brain imaging. Magn Reson Med. 2010;63:194-206.
8. Schweser F, Deistung A, Lehr BW, Reichenbach JR. Quantitative imaging of intrinsic magnetic tissue properties using MRI signal phase: an approach to in vivo brain iron metabolism? Neuroimage. 2011;54:2789-2807.
9. Schweser F, Sommer K, Deistung A, Reichenbach JR. Quantitative susceptibility mapping for investigating subtle susceptibility variations in the human brain. Neuroimage. 2012;62:2083-2100.
10. Deistung A, Schafer A, Schweser F, Biedermann U, Turner R, Reichenbach JR. Toward in vivo histology: a comparison of quantitative susceptibility mapping (QSM) with magnitude-, phase-, and R2*-imaging at ultra-high magnetic field strength. Neuroimage. 2013;65:299-314.

11. Wu B, Li W, Avram AV, Gho SM, Liu C. Fast and tissue-optimized mapping of magnetic susceptibility and T2* with multi-echo and multi-shot spirals. Neuroimage. 2012;59:297-305.
12. Walsh AJ, Blevins G, Lebel RM, Seres P, Emery DJ, Wilman AH. Longitudinal MR Imaging of Iron in Multiple Sclerosis: An Imaging Marker of Disease. Radiology. 2013
13. Klassen LM, Menon RS. Robust automated shimming technique using arbitrary mapping acquisition parameters (RASTAMAP). Magn Reson Med. 2004;51:881-887.
14. Curtis AT, Gilbert KM, Klassen LM, Gati JS, Menon RS. Slice-by-slice B1+ shimming at 7 T. Magn Reson Med. 2012;68:1109-1116.
15. Peters AM, Brookes MJ, Hoogenraad FG et al. T2* measurements in human brain at 1.5, 3 and 7 T. Magn Reson Imaging. 2007;25:748-753.
16. Abdul-Rahman HS, Gdeisat MA, Burton DR, Lalor MJ, Lilley F, Moore CJ. Fast and robust three-dimensional best path phase unwrapping algorithm. Appl Opt. 2007;46:6623-6635.
17. Jenkinson M, Beckmann CF, Behrens TE, Woolrich MW, Smith SM. FSL. Neuroimage. 2012;62:782-790.
18. Benjamini Y, Yekutieli D. The control of the false discovery rate in multiple testing under dependency. Annals of statistics. 2001;1165-1188.
19. Kitzler HH, Su J, Zeineh M et al. Deficient MWF mapping in multiple sclerosis using 3D whole-brain multi-component relaxation MRI. Neuroimage. 2012;59:2670-2677.
20. HALLGREN B, SOURANDER P. The effect of age on the non-haemin iron in the human brain. J Neurochem. 1958;3:41-51.
21. Dowling P, Husar W, Menonna J, Donnenfeld H, Cook S, Sidhu M. Cell death and birth in multiple sclerosis brain. J Neurol Sci. 1997;149:1-11.
22. Ge Y, Zohrabian VM, Osa EO et al. Diminished visibility of cerebral venous vasculature in multiple sclerosis by susceptibility-weighted imaging at 3.0 Tesla. J Magn Reson Imaging. 2009;29:1190-1194.

23. Law M, Saindane AM, Ge Y et al. Microvascular abnormality in relapsing-remitting multiple sclerosis: perfusion MR imaging findings in normal-appearing white matter. Radiology. 2004;231:645-652.
24. Wuerfel J, Bellmann-Strobl J, Brunecker P et al. Changes in cerebral perfusion precede plaque formation in multiple sclerosis: a longitudinal perfusion MRI study. Brain. 2004;127:111-119.
25. Jochimsen TH, Ivanov D, Ott DV et al. Whole-brain mapping of venous vessel size in humans using the hypercapnia-induced BOLD effect. Neuroimage. 2010;51:765-774.
26. Kolind S, Matthews L, Johansen-Berg H et al. Myelin water imaging reflects clinical variability in multiple sclerosis. Neuroimage. 2012;60:263-270.
27. Aliotta R, Cox JL, Donohue K et al. Tract-based spatial statistics analysis of diffusion-tensor imaging data in pediatric- and adult-onset multiple sclerosis. Hum Brain Mapp. 2014;35:53-60.
28. Li TQ, van Gelderen P, Merkle H, Talagala L, Koretsky AP, Duyn J. Extensive heterogeneity in white matter intensity in high-resolution T2*-weighted MRI of the human brain at 7.0 T. Neuroimage. 2006;32:1032-1040.
29. Laule C, Vavasour IM, Leung E et al. Pathological basis of diffusely abnormal white matter: insights from magnetic resonance imaging and histology. Mult Scler. 2011;17:144-150.
30. Barkhof F. The clinico-radiological paradox in multiple sclerosis revisited. Curr Opin Neurol. 2002;15:239-245.
31. Langkammer C, Liu T, Khalil M et al. Quantitative susceptibility mapping in multiple sclerosis. Radiology. 2013;267:551-559.
32. Lebel RM, Eissa A, Seres P, Blevins G, Wilman AH. Quantitative high-field imaging of sub-cortical gray matter in multiple sclerosis. Mult Scler. 2012;18:433-441.
33. Zivadinov R, Havrdova E, Bergsland N et al. Thalamic atrophy is associated with development of clinically definite multiple sclerosis. Radiology. 2013;268:831-841.
34. Love S. Demyelinating diseases. J Clin Pathol. 2006;59:1151-1159.

35. Behbehani R. Clinical approach to optic neuropathies. Clin Ophthalmol. 2007;1:233-246.
36. Li W, Wu B, Liu C. Quantitative susceptibility mapping of human brain reflects spatial variation in tissue composition. Neuroimage. 2011;55:1645-1656.
37. Li W, Wu B, Avram AV, Liu C. Magnetic susceptibility anisotropy of human brain in vivo and its molecular underpinnings. Neuroimage. 2012;59:2088-2097.
38. Lee J, Shmueli K, Kang B-T et al. The contribution of myelin to magnetic susceptibility-weighted contrasts in high-field MRI of the brain. Neuroimage. 2012;59:3967-3975.
39. Bagnato F, Hametner S, Yao B et al. Tracking iron in multiple sclerosis: a combined imaging and histopathological study at 7 Tesla. Brain. 2011;134:3602-3615.

Chapter 6

Conclusion and Future Directions

The Journey is the Reward.

– Steve Jobs, *iSteve*

MRI is capable of producing images revealing a vast array of different tissue parameters (1, 2). Currently, for instance, MRI contrast can be preferentially sensitized to tissue relaxation properties (T_1, T_2 and T_2^*), microstructure (diffusion and susceptibility-based MRI) and motional properties (blood flow and water diffusion) (3). The work presented in this thesis has investigated the fundamental relationship between the susceptibility contrast parameters (R_2^*, LFS and $\Delta\chi$) and underlying tissue structure. The research was carried out using biophysical modeling and correlation with quantitative histology. For the first time, multiple biophysical modeling schemes were compared in both gray and white matter for excised rat brain tissue. Additionally, scaling relations were derived for calculating the reversible, mesoscopic magnetic field component, R_2', of the apparent transverse relaxation rate from the orientation dependence in gray and white matter.

An optimal susceptibility processing pipeline was also developed and applied to the calculation of phase-combined LFS and QS maps obtained using ultra-high field (UHF) MRI. The processing pipeline was then utilized to monitor myelin and iron changes in MS patients compared to healthy, age and gender-matched controls by employing voxel-wise analysis in a standard template space. With the use of QS and R_2^* mapping, evidence of statistically significant increases in iron deposition in sub-cortical gray matter structures, as well as myelin degeneration along the white matter skeleton, were identified in MS patients. Equally relevant, the 7 T MS study itself represents the first use of voxel-wise morphometry in both MS white matter and sub-cortical gray matter using R_2^* and QS.

In the ensuing section, we identify future directions for the research documented in this thesis, with an emphasis on both technical developments and clinical applications. Two areas of technological development which have the potential for significant methodological advances in magnetic properties mapping-based MRI are discussed: (i) the use of susceptibility tensor-based white matter anisotropy assessment (4) and (ii) combined electric and magnetic properties brain tissue mapping (5). Refinement of these methodologies could result in an enhanced understanding of brain tissue compositional changes in vivo. This is directly applicable to quantitative monitoring of demyelination and remyelination in MS. In terms of clinical applications, some recent results from our longitudinal MS study are presented which focus on the use of susceptibility-based UHF MRI contrasts.

6.1 Future directions: Technical Developments

6.1.1 Susceptibility tensor-based MRI as an alternative to diffusion MRI for monitoring microstructure in MS

Diffusion tensor imaging (DTI) is now a standard method for investigating the architecture and integrity of white matter pathways in the human central nervous system (6). DTI uses time-varying, pulsed magnetic field gradients applied at different orientations to probe the principal direction of water self-diffusion in axons (7, 8). In doing so, it provides *in vivo* information concerning pathological processes that can occur in white matter. For instance, in MS, it has allowed for detection of changes in water diffusion directionality in both lesions and normal-appearing white matter (9-11). However, acquisition of DTI data places considerable demands on MRI gradient hardware and data interpretation is challenging. In particular, the lower SNR of DTI scans generally results in significantly lower spatial resolution compared to the high-resolution, T_1 or T_2-weighted images conventionally used in MS diagnosis. DTI scans on clinical scanners use spatial resolutions of 2 - 3 mm. This is a substantial disadvantage when monitoring the cellular and sub-cellular environment of MS brain tissue. A larger voxel integrates processes from multiple biological environments, resulting in difficulty interpreting data. To date, high resolution DTI has only been performed: (i) in ex-vivo specimens (12, 13), (ii) using thick slices which sacrifice spatial resolution along the slice axis of the image acquisition (14) or (iii) by employing increased angular sampling (15, 16).

Susceptibility-tensor imaging (STI) may offer an alternative to DTI in cases where high resolution and short scan time are required. STI is performed using a standard, short TR, gradient echo acquisition and relies on the magnetic susceptibility anisotropy (MSA) of white matter axons, believed to be mediated by the phospholipid molecules in the myelin sheath (17). A critical assumption of STI, as it pertains to white matter imaging of the brain, is that the principal axis of the MSA is parallel to the long axis of axons. With this assumption, the magnetic susceptibility tensor of white matter can be decomposed into three eigenvalues and their associated eigenvectors, utilizing a simple matrix eigenvalue decomposition (18). The corresponding eigenvalues can then be used to estimate susceptibility anisotropy and thus probe myelination. In addition, by applying conventional line search-based tracking algorithms from DTI to the STI model, fiber pathways can be reconstructed.

Currently, only one study conducted in perfusion-fixed, mouse brains at 7 T, has demonstrated ST images comparable to that achieved with DTI (18). In that study, STI demonstrated reliable anisotropy assessment and fiber tracking in the corpus callosum, hippocampal commissure and anterior commissure major white matter fiber bundles. STI tracts appeared smoother at the edge of the fiber bundles while the major tracking direction was determined by the eigenvalue with the least diamagnetic susceptibility (18). However, the STI procedure has not been extended to human scanning. Such an extension would require improvements in the regularization model applied with the STI matrix inversion, as well as improvements to the pulse sequence and B_0 shimming used in data acquisition.

Sample rotation also poses a fundamental constraint on STI reconstruction. Alternative methods have recently been suggested allowing either (i) STI reconstruction using a small number of head rotations with a cylindrically symmetric susceptibility tensor (CSST) (19) or (ii) STI reconstruction from a single orientation utilizing a multipole expansion of the image phase in terms of higher-order moments (20). During preliminary investigations, the protocols have shown promise but require further refinement from both an acquisition and mathematical analysis standpoint.

DTI has evolved considerably since its first demonstration nearly fifteen years ago by Mori et al. (7). With continued improvement in both rapid image acquisition and B_0 shimming and the computational processing of higher-order phase data, STI-based techniques (18, 19, 21) have the potential to provide significant complementary information to DTI fiber tracking.

6.1.2 Combined magnetic and electric tissue properties mapping

Electromagnetic properties tissue mapping (EPTM), which includes susceptibility, conductivity and permittivity imaging, forms the basis of a new contrast in high-field MRI which is uniquely sensitive to subtle changes in the microstructure of myelin and the concentration of ferritin iron (5, 22, 23). A more refined understanding of the electromagnetic properties of brain tissue, particularly how they change in pathological conditions such as MS, could allow for more informed diagnosis and treatment. Presently, work in the high-field MRI community has focused on the concise mathematical and computational understanding of susceptibility properties that can be derived from the image phase. A principal area of focus has centered around coupling standard gradient-echo acquisitions with advanced processing methods to isolate the volume magnetic susceptibility of tissue from the signal phase (17, 20, 22, 24).

Electric properties tissue mapping (EPTM) is an emerging related field which focuses on the reconstruction of images depicting both tissue conductivity (σ) and permittivity (ε) (25, 26). The reconstruction of quantitative conductivity maps has been given the acronym QCM (5). Its diagnostic utility has been cited in studies monitoring: (i) heart muscle viability after myocardial infarction (27), (ii) brain tissue changes in response to stroke (28) and (iii) differences between healthy and malignant tissue in cancer (29). EPTM methods are also central to MRI RF safety, particularly in high field MRI where heating can become a concern (25, 30).

Through Maxwell's equations, a relationship exists between the conductivity of a biological tissue (σ) in a strong external magnetic field under the influence of RF excitation and the complex-valued B_1 transmit field (B_1^+) (25, 26, 31). Initially, it was believed accurate conductivity estimates were only available when using both the *magnitude and phase* of the B_1^+ field (31). A disadvantage of this is its requiring two separate scans: (i) a gradient echo, actual flip angle imaging (AFI) sequence to measure the magnitude of the B_1^+ field (32) and (ii) a spin echo sequence to sensitively measure the B_1^+ phase (31). Acquiring two separate scans in this manner lengthened the acquisition time and resulted in two images having different geometric and point-spread function-based distortions. To circumvent this difficulty, recent work has identified the conditions under which it is possible to reconstruct images of tissue conductivity using only the phase of the $B_1{}^+$ distribution (5, 25, 26). Assuming local transmit field homogeneity, the tissue conductivity can be derived from an appropriate re-arrangement of the Helmholtz wave equation :

$$\sigma = \frac{\nabla^2 e^{i\angle f(B_1^+)}}{\mu\omega e^{i\angle f(B_1^+)}} \qquad [6.1]$$

where f represents a filter used to improve SNR in the conductivity map reconstruction, μ is permeability of the sample, ω represents the Larmor frequency of the tissue and $\angle B_1^+$ is the phase of the RF transmit field (33). For a single channel, quadrature head coil, the phase of the B_1^+ field can be approximated by taking half of the phase value acquired at an echo time of TE = 0 (26). This is advantageous because it simplifies the solution to equation [6.1] and suggests that *both conductivity and susceptibility* can be measured in a single scan utilizing a multi-echo, gradient echo sequence (5).

Provided the magnitude of the B_1^+ field is also known from AFI mapping, permittivity (ε) is an additional parameter that can be calculated using EPTM (26, 34). Although both permittivity and conductivity offer complementary information to QS maps, the specific relationship between these variables in human brain has not been explored. One significant area of interest involves the combined mapping of QCM and QSM in white matter fibers of the human brain. For a myelinated axon, there is an approximate phenomenological relation between the radius of the axon and the thickness of the myelin bilayer (35). If the approximate rate of conduction of an action potential along an axon bundle is known from QCM, it may be possible to combine this with QSM to estimate myelin concentration. Further, measurement of co-registered QSM and QCM maps with minimal image distortion would allow correction of QS maps for spurious conductivity-induced B_1^+ phase signal (5). This would result in more accurate determination of QS in white matter and, ultimately, more accurate determination of axonal myelination.

6.2 Future directions: Clinical Applications

Applying the existing magnetic properties mapping methods outlined in this thesis to longitudinal MS imaging and assessment of cortical demyelination patterns could facilitate detection of more subtle abnormalities preceding gross lesion formation and brain atrophy. In this section a representative preliminary analysis of serial scan data from our ongoing longitudinal 7 T MS study is presented. It focuses on: (i) the quantitative patterns of R_2^* and LFS changes in white matter lesions over approximately one year in four representative patients and (ii) the patterns of decreased pial R_2^* in MS patients compared to age and gender-matched controls based on data from the cross-sectional study documented in Chapter 5 of this thesis.

6.2.1 Longitudinal Analysis of Magnetic Properties of MS White Matter Lesions Compared to Standard Clinical Contrasts

A complex sequence of inflammatory and neurodegenerative processes underlies lesion formation in MS. The disappearance and subsequent re-appearance of white matter lesions on serial T_2-weighted MR images of RRMS patient brain is a trademark feature which has been linked to clinical relapses and subsequent periods of remission. However, observation of lesion dynamics on serial T_1 and T_2-weighted MRI scans has not offered significant predictive power toward understanding disease progression. One possible explanation is that standard MRI contrasts only visualize a fraction of the disease burden (in both gray and white matter) which exists in MS. Standard T_1 and T_2-weighted sequences employed in clinical trials and routine follow-up assessment usually fail to identify transient white matter lesions. This is because, during remission phases of the RRMS disease, lesions on T_2-weighted scans can appear isotense compared to surrounding normal white matter. This confounds assessment of total lesion burden.

An alternative to single time point lesion number or lesion volume-based assessment is time-series modeling of the MRI signal within a lesion. Serial MRI of MS patients has identified that, in the short time period ($\leq$ 1 year) following contrast enhancement, distinct phases of increased and decreased signal intensity appear in concentric patterns around the centre of white matter lesions (36, 37). More specifically, Meier et al. (37, 38) demonstrated that, for selected white matter lesions, a sigmod-function mathematical model of two competing processes (degeneration and repair) could partially explain the temporal evolution of lesions. The time-series modeling approach also has the potential to detect how drugs target specific phases of disease evolution, thus enhancing the assessment of drug treatment efficacy.

However, time-series modeling using standard T_1 and T_2-weighted clinical scans is non-quantitative and inherently challenging due to the presence of coil sensitivity and bias field offsets which can change across RF coils and MRI scanners. Moreover, it is very difficult to assign the signal change on T_1 and T_2-weighted images to specific inflammatory or repair processes occuring in MS at the cellular level. In this regard, the sensitivity of the quantitative susceptibility-based MRI contrasts to iron and myelin may offer an improved picture of the biological changes occuring across time within MS lesions (39, 40).

To perform a preliminary investigation of the potential of the susceptibility contrasts for longitudinal monitoring of lesion dynamics, serial scans taken at four months intervals over one year for RRMS patients enrolled in the ongoing, longitudinal 7 T MS imaging study at the Robarts Research Institute were analyzed. The four contrasts employed for this analysis included two non-quantitative MRI contrasts (T_1-weighted MPRAGE and T_2-weighted MP-FLAIR anatomical images), as well as two quantitative MRI contrasts (R_2^* and LFS). Seventy-six lesions were selected in four RRMS patients on the basis of their appearance on all four MRI contrasts for at least one time point in the serial images. A manual segmentation was initially performed around the edge of lesions on the LFS maps in each slice. The resulting binary, 2D segmentation masks were subsequently converted to 3D lesion masks by merging connected components. For each patient, all images were affine-registered to the high-resolution

GRE image corresponding to the patients' most recent visit. The mean and standard error in R_2^* and LFS of the lesions on each visit were then computed.

Figure 6.1 on page 128 displays the results of the above analysis. Over the full eight to twelve month time course for each patient, distinct changes in mean R_2^* and LFS are visible. Figure 6.1a demonstrates the results for a 46 year-old female RRMS patient with an EDSS score of 1.0. The reduction in R_2^* and positive, paramagnetic shift in the LFS can be interpreted as demyelination occuring over a 12 month period. All of the seven lesions identified for this patient followed the same pattern of steadily reduced R_2^* and increased LFS (Note that this is LFS relative to frontal white matter). Although iron might be present in these lesions, iron increase would generally be coupled with increased R_2^* and this is not observed.

Fig. 6.1b displays imaging data taken from a 40 year-old female RRMS patient with an EDSS score of 1.5 and 18 uniquely identified lesions. In the majority of lesions, R_2^* decreased during the period from zero to four months, followed by a steady increase to the one year time point. When coupled with the patterns seen on LFS, this result is interpreted as demyelination in the first four months, followed by increased iron deposition between four months and one year. A justification for this interpretation is the combined increase in R_2^* and the paramagnetic shift on LFS between four months and one year.

Figure 6.1c presents serial imaging data taken from a 34 year-old male RRMS patient with an EDSS score of 1.0. For the majority of the 26 lesions, the R_2^* slowly increased, then decreased. The local frequency shift showed a distinct increase from zero to four months, followed by a subsequent decrease. Such a result can be interpreted as a period of remyelination from zero to four months followed by demyelination occuring from the four month to one year time points.

Fig. 6.1d demonstrates serial imaging data for a 38 year-old male RRMS patient with an EDSS score of 1.5. For this patient, in the majority of the 25 lesions, the mean LFS increased, then decreased over an eight month period. However, the R_2^* value in lesions steadily increased between zero and four months, then leveled off. This result suggests accumulation of iron in macrophages and glial cells around the lesion in the zero to four month period, followed by subsequent remyelination and a resultant diamagnetic shift (decrease in the relative LFS signal).

In Figure 6.2 on page 129, changes in lesion visibility on the four MRI contrasts acquired from a 38 year-old male RRMS patient with an EDSS score of 1.5 are displayed as serial images. Enlarged views of two selected lesions (highlighted by blue and yellow arrows) are shown in Figure 6.3 on page 130. Three trends are apparent: (i) diffusely reduced R_2^* and paramagnetically shifted (darker colours) LFS appear in some lesions prior to lesion visibility on T_1 or T_2-weighted scans (yellow arrows), (ii) some chronic lesions which are persistent across all scans on T_1 and T_2-weighted images show decreases in R_2^* over the 8 month time course (blue arrows), (iii) not all R_2^* visible lesions are observed on corresponding LFS maps. For instance, the lesion indicated by the red arrow in the R_2^* map is not visible on the corresponding LFS map.

The finding that subtle changes on R_2^* and LFS can precede lesion appearance on T_1 and T_2-weighted images suggests these contrasts could improve the monitoring of relapsing-remitting lesions. The progressive reduction in lesion R_2^* over the course of eight months, highlighted by the red arrow in Figure 6.2c, suggests that, in chronic lesions where little to no dynamic changes are observed on T_1 or T_2 –weighted images, R_2^* may be useful for quantifying the subtle microstructural changes to myelin and axonal integrity that are occuring.

It should be underlined that this preliminary data requires further validation by incorporating a larger number of lesions in RRMS patients with varying EDSS scores. As well, due to the lack of contrast-enhanced imaging in our 7 T study, it was not possible to determine when a lesion first appeared. Using clinical scans acquired at the time of the first diagnosis for these patients may allow approximation of lesion age and improved stratification of white matter lesions into those which have persisted over time, those that have undergone transient signal intensity changes over time and those that have newly appeared in white matter during the course of the 7 T study. A goal for future analysis of the longitudinal imaging data from the 7 T MS imaging study is to characterize the R_2^* and LFS signal changes into specific lesion types, such as transient T_2 enhancing lesion, transient T_1 black holes and chronic T_1 black holes. Further research will also incorporate QSM analysis of both lesions and surrounding white matter.

6.2.2 Cortical R_2^* Mapping in MS Patients

Recently, there has been a surge of interest in MRI-based evaluation of cortical sub-pial demyelination using such quantitative techniques as magnetization transfer (41) and T_2^*-based imaging (42). This interest has been fueled by the increased spatial resolution and improved SNR provided by high-field MRI in combination with conformal, multi-channel receive RF coils (43). Several post-mortem studies have noted a frequent and wide-ranging influence of cortical demyelination in MS (44, 45). To date, however, there

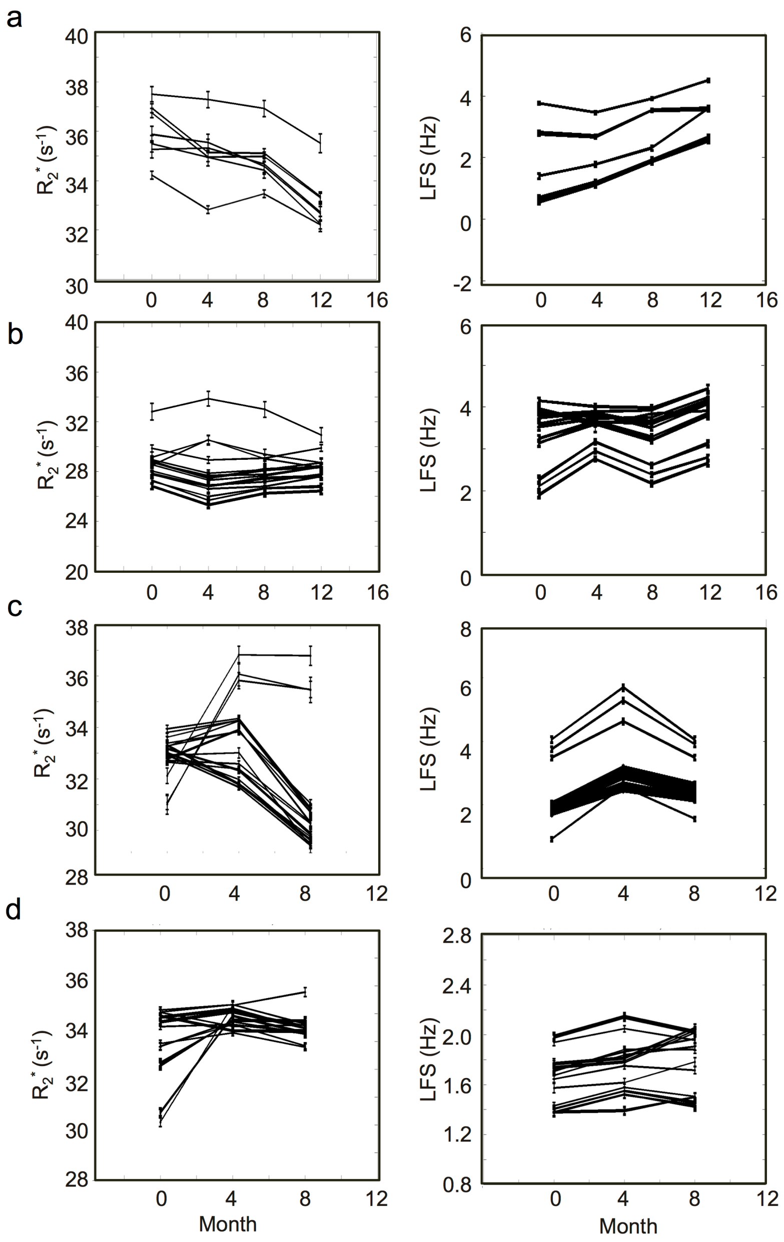

Figure 6.1. Temporal evolution of the mean R_2^* and LFS signal within RRMS white matter lesions over the course of the first year of the longitudinal MS imaging study. (a) corresponds to a 46 year-old female patient with an EDSS score of 1.0. (b) corresponds to a 40 year-old female patient with an EDSS score of 1.5. (c) corresponds to a 34 year-old male patient with an EDSS score of 1.0. (d) corresponds to a 38 year-old male patient with an EDSS score of 1.5.

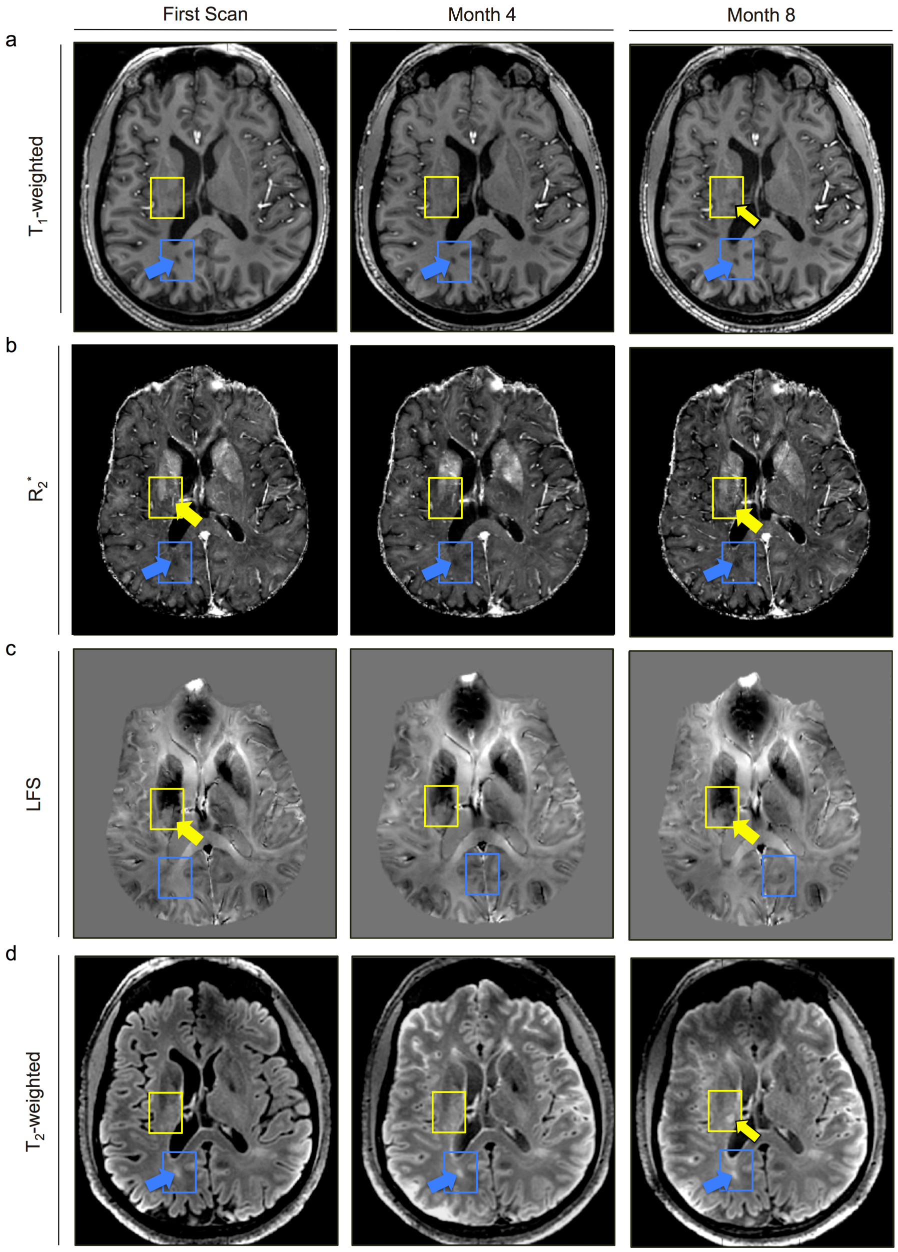

Figure 6.2. Representative longitudinal images from a select patient with MS. Serial MR images, taken at four month intervals, for a 38 year-old male RRMS patient with an EDSS score of 1.5. The yellow arrows point to a lesion in the sub-cortical GM which is detected before its subsequent appearance on T_1 and T_2-weighted MRI scans 8 months after the first scan. The blue arrows indicate a lesion in white matter which is visible on R_2^* but not on LFS.

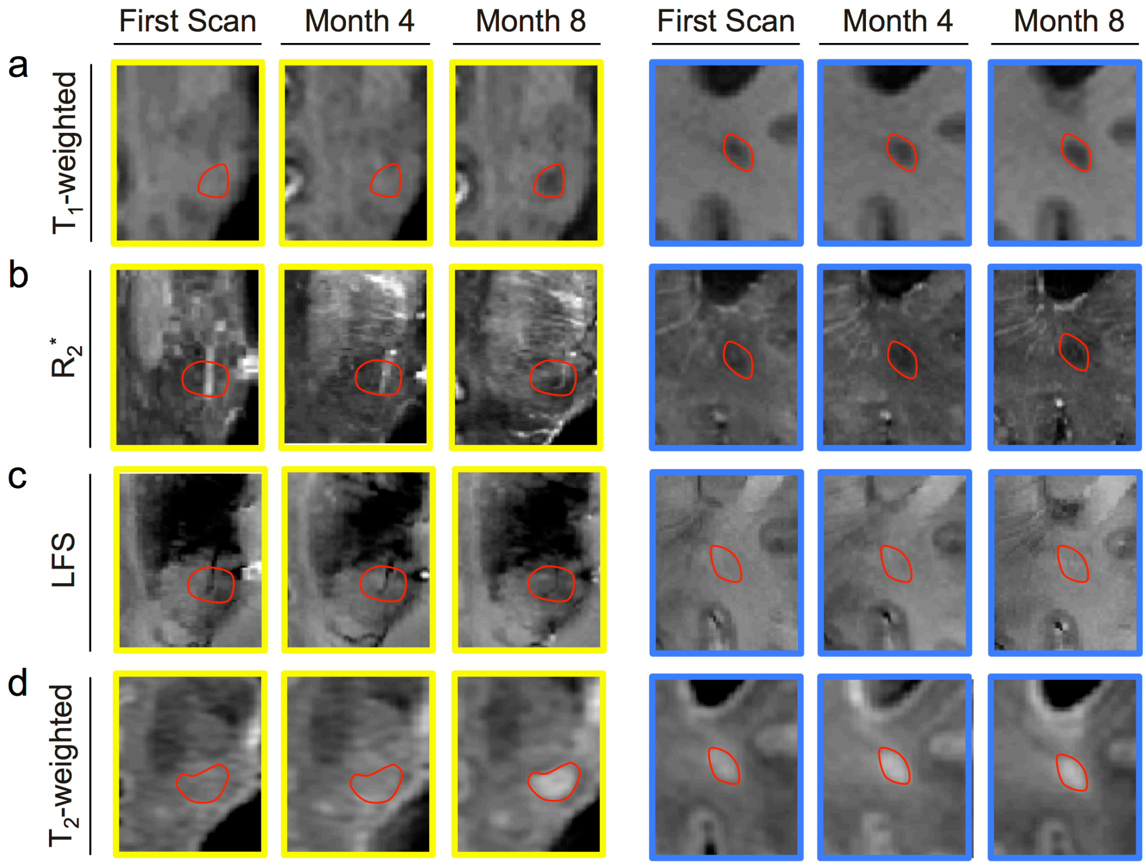

Figure 6.3. Cropped and enlarged lesions as visualized by UHF MRI. These are enlarged views of the lesions identified with yellow and blue arrows in Figure 6.2. The changes in the R_2^* and LFS contrasts are compared to the standard T_1 and T_2-weighted clinical images. Regions of interest (lesions) are outlined in red.

have been few *in vivo* studies examining the role of subpial demyelination across different brain regions.

Equally important, the existence of reduced R_2^* values in patients with MS compared to age and gender-matched controls has yet to be evaluated. With this in mind, as part of the 7 T MS imaging study, we examined localized differences in R_2^* of 25 MS patients compared to 15 controls along the cortical pial surface utilizing group-averaged cortical surface renderings generated in the Freesurfer software (46). Decreases in and along the cortical surface are characteristic of subpial demyelination. Such changes have already been observed at 7 T using the magnitude signal in a small cohort of MS patients (47). Nevertheless, the use of R_2^* in cortical surface mapping and the reproducibility of these changes remains unclear. In our study, we evaluated cortical R_2^* changes to determine their utility in monitoring MS disease severity and staging.

Figure 6.4 displays statistical differences ($-\log_{10}(p)$) in cortical R_2^* of patients compared to age-matched controls. Statistical significance colour maps are overlaid on the average pial surface from all 25 patients included in the cross-sectional study outlined in Chapter 5. Reduced R_2^* in patients compared to controls is represented with blue colours. Areas of significantly reduced R_2^* along the pial surface of the cortex may represent regions of sub-pial demyelination. Reduced R_2^* is visible: (i) near the intersection of the post-central gyrus and superior parietal lobule (green arrows, left and right hemispheres), (ii) in the inferior portion of the pre-frontal cortex (pink arrow, left and right hemispheres) and (iii) at the interface between the superior frontal and caudal frontal gyri (yellow arrow, left hemisphere). Red areas indicate regions of significantly increased R_2^*, indicative of elevated iron deposition along the pial surface. Elevated R_2^* is shown in the caudal frontal sulcus of the left lateral surface (purple arrow, left hemisphere).

Cortical pathology has previously been examined utilizing high-field (7 T) MRI with multi-channel receive coils in a small population of MS patients (42). Cortical lesions were visualized and categorized into sub-types (I – IV) using high-resolution, multi-slice, 2D gradient echo imaging at 7 T. This work was recently extended to full cortical surface mapping employing the T_2^*-weighted magnitude signal projected onto an

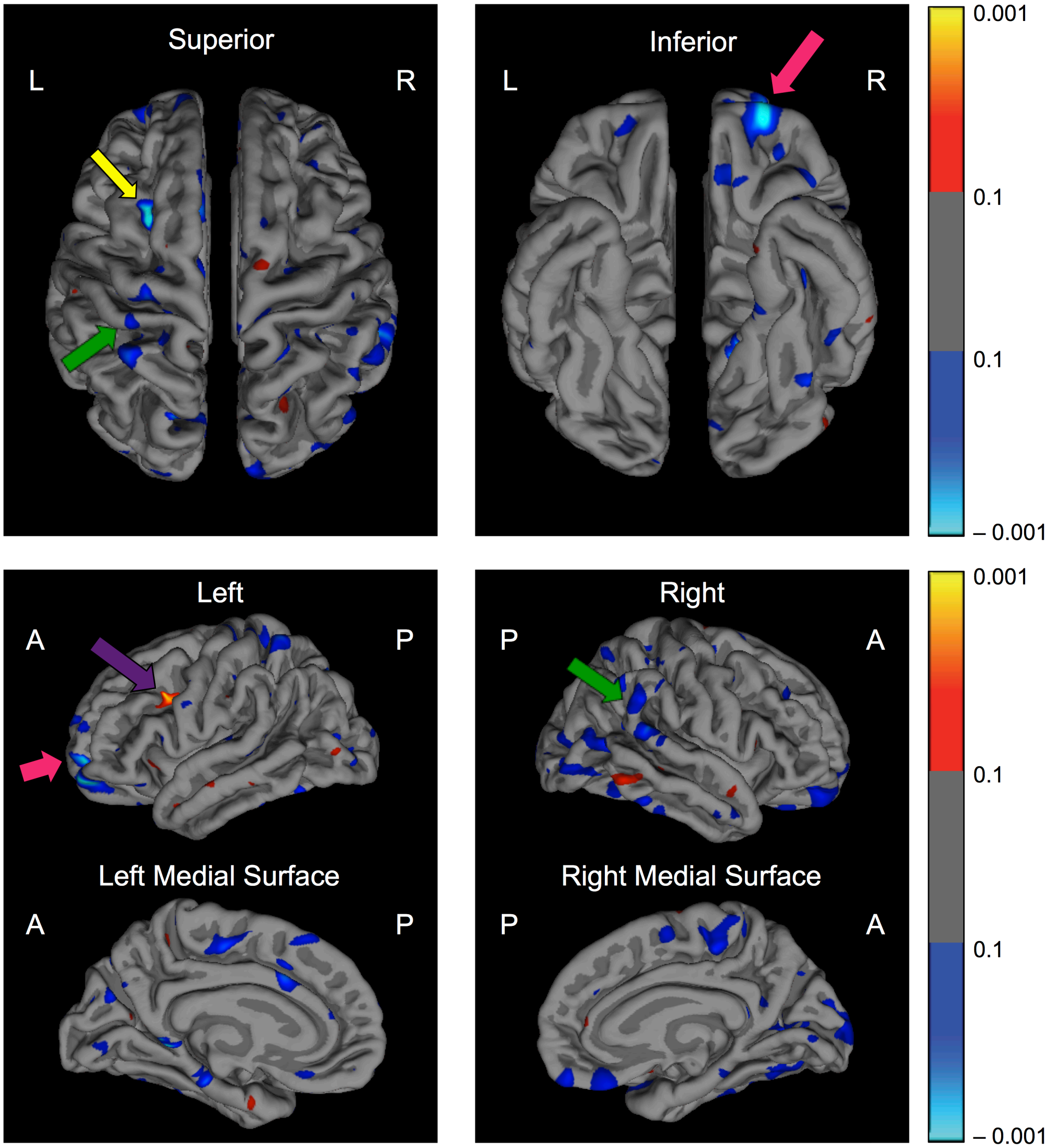

Figure 6.4. Student's t-test significance (-$\log_{10}(p)$) overlaid on the freesurfer-generated average pial surface for the patient cohort. Significance maps are thresholded at a level of $p < 0.1$. Blue areas indicate regions of significantly reduced R_2^* for patients compared to controls. Reduced R_2^* is representative of sub-pial demyelination and is observed along the post-central gyrus, in the superior temporal lobe and in the pre-frontal cortex. Red areas indicate regions of significantly increased R_2^* which are indicative of increased iron deposition along the pial surface.

average pial surface (47). However, the T_2^*-based magnitude signal varies as a function of receiver coil sensitivity, field strength and B_1 and B_0 shimming protocols (48). In our study, areas of significantly reduced quantitative R_2^*, independent of receiver coil technology and B_1 or B_0 shimming, were observed along the pial surface in brain regions associated with sensorimotor, memory and cognitive function. In particular, reductions in Figure 6.4 are seen in the motor region near the intersection of the post-central gyrus and superior parietal lobule (Figure 6.4, green arrows, left and right hemispheres), in the inferior portion of the pre-frontal cortex (Figure 6.4, pink arrow, left and right hemispheres) and at the inferface of the superior frontal and caudal frontal gyri (Figure 6.4, yellow arrow, left hemisphere). These results are consistent with a previous report (47) of heightened T_2^* in the sensorimotor regions, near the left parsopercularis and in the superior parietal lobe.

In contrast to the previous study (33), however, our data showed no significant changes in T_2^* (R_2^*) in the lateral occipital lobe but did show R_2^* reductions in the pre-frontal cortex. Such differences may reflect differences in the imaging parameters used in each study (2D, single-echo FLASH imaging was used by Cohen-Adad et al. with a resolution of $0.33 \times 0.33 \times 1$ mm^3 , while our study employed 3D, multi-echo FLASH with $0.5 \times 0.5 \times 1.25$ mm^3). The differences may also be characteristic of the different patient cohorts. Cortical mapping of R_2^* in a larger patient cohort combined with longitudinal analysis is presently underway to verify changes observed in our study and relate them to clinical disease status.

6.3 References

1. Tofts PS, Du Boulay EPGH. Towards quantitative measurements of relaxation times and other parameters in the brain. Neuroradiology. 1990;32:407-415.
2. Stanisz GJ, Odrobina EE, Pun J et al. T1, T2 relaxation and magnetization transfer in tissue at 3T. Magn Reson Med. 2005;54:507-512.
3. Haacke EM, Brown RW, Thompson MR, Venkatesan R. Magnetic resonance imaging: physical principles and sequence design. Wiley-Liss New York:; 1999
4. Liu C. Susceptibility tensor imaging. Magn Reson Med. 2010;63:1471-1477.
5. Kim DH, Choi N, Gho SM, Shin J, Liu C. Simultaneous imaging of in vivo conductivity and susceptibility. Magn Reson Med. 2013
6. Basser PJ, Jones DK. Diffusion-tensor MRI: theory, experimental design and data analysis - a technical review. NMR Biomed. 2002;15:456-467.
7. Mori S, Crain BJ, Chacko VP, van Zijl PC. Three-dimensional tracking of axonal projections in the brain by magnetic resonance imaging. Ann Neurol. 1999;45:265-269.
8. Derek K. Diffusion MRI: Theory, methods, and applications. 2011
9. Filippi M, Rocca MA, De Stefano N et al. Magnetic resonance techniques in multiple sclerosis: the present and the future. Arch Neurol. 2011;68:1514-1520.
10. Liu Y, Mitchell PJ, Kilpatrick TJ et al. Diffusion tensor imaging of acute inflammatory lesion evolution in multiple sclerosis. J Clin Neurosci. 2012;19:1689-1694.
11. Sbardella E, Tona F, Petsas N, Pantano P. DTI Measurements in Multiple Sclerosis: Evaluation of Brain Damage and Clinical Implications. Mult Scler Int. 2013;2013:671730.
12. McNab JA, Jbabdi S, Deoni SC, Douaud G, Behrens TE, Miller KL. High resolution diffusion-weighted imaging in fixed human brain using diffusion-weighted steady state free precession. Neuroimage. 2009;46:775-785.
13. Miller KL, Stagg CJ, Douaud G et al. Diffusion imaging of whole, post-mortem human brains on a clinical MRI scanner. Neuroimage. 2011;57:167-181.
14. Sarlls JE, Pierpaoli C. In vivo diffusion tensor imaging of the human optic chiasm at sub-millimeter resolution. Neuroimage. 2009;47:1244-1251.

15. Tournier JD, Calamante F, Gadian DG, Connelly A. Direct estimation of the fiber orientation density function from diffusion-weighted MRI data using spherical deconvolution. Neuroimage. 2004;23:1176-1185.
16. Wedeen VJ, Hagmann P, Tseng WY, Reese TG, Weisskoff RM. Mapping complex tissue architecture with diffusion spectrum magnetic resonance imaging. Magn Reson Med. 2005;54:1377-1386.
17. Li W, Wu B, Avram AV, Liu C. Magnetic susceptibility anisotropy of human brain in vivo and its molecular underpinnings. Neuroimage. 2012;59:2088-2097.
18. Liu C, Li W, Wu B, Jiang Y, Johnson GA. 3D fiber tractography with susceptibility tensor imaging. Neuroimage. 2012;59:1290-1298.
19. Wisnieff C, Liu T, Spincemaille P, Wang S, Zhou D, Wang Y. Magnetic susceptibility anisotropy: cylindrical symmetry from macroscopically ordered anisotropic molecules and accuracy of MRI measurements using few orientations. Neuroimage. 2013;70:363-376.
20. Li X, Vikram DS, Lim IA, Jones CK, Farrell JA, van Zijl PC. Mapping magnetic susceptibility anisotropies of white matter in vivo in the human brain at 7 T. Neuroimage. 2012;62:314-330.
21. Liu C, Li W. Imaging neural architecture of the brain based on its multipole magnetic response. Neuroimage. 2013;67:193-202.
22. Schweser F, Deistung A, Lehr BW, Reichenbach JR. Quantitative imaging of intrinsic magnetic tissue properties using MRI signal phase: an approach to in vivo brain iron metabolism? Neuroimage. 2011;54:2789-2807.
23. Schweser F, Sommer K, Deistung A, Reichenbach JR. Quantitative susceptibility mapping for investigating subtle susceptibility variations in the human brain. Neuroimage. 2012;62:2083-2100.
24. Deistung A, Schafer A, Schweser F, Biedermann U, Turner R, Reichenbach JR. Toward in vivo histology: a comparison of quantitative susceptibility mapping (QSM) with magnitude-, phase-, and R2*-imaging at ultra-high magnetic field strength. Neuroimage. 2013;65:299-314.

25. Voigt T, Katscher U, Doessel O. Quantitative conductivity and permittivity imaging of the human brain using electric properties tomography. Magn Reson Med. 2011;66:456-466.
26. van Lier AL, Raaijmakers A, Voigt T et al. Electrical Properties Tomography in the Human Brain at 1.5, 3, and 7T: A Comparison Study. Magn Reson Med. 2013
27. Schaefer M, Gross W, Ackemann J, Gebhard MM. The complex dielectric spectrum of heart tissue during ischemia. Bioelectrochemistry. 2002;58:171-180.
28. Liu L, Dong W, Ji X et al. A new method of noninvasive brain-edema monitoring in stroke: cerebral electrical impedance measurement. Neurological research. 2006;28:31-37.
29. Joines WT, Zhang Y, Li C, Jirtle RL. The measured electrical properties of normal and malignant human tissues from 50 to 900 MHz. Medical physics. 1994;21:547.
30. Katscher U, Findeklee C, Voigt T. B1-based specific energy absorption rate determination for nonquadrature radiofrequency excitation. Magn Reson Med. 2012;68:1911-1918.
31. editors. Electrical conductivity imaging using magnetic resonance tomography. Engineering in Medicine and Biology Society, 2009. EMBC 2009. Annual International Conference of the IEEE; 2009; IEEE; 2009.
32. Yarnykh VL. Actual flip-angle imaging in the pulsed steady state: a method for rapid three-dimensional mapping of the transmitted radiofrequency field. Magn Reson Med. 2007;57:192-200.
33. van Lier AL, Brunner DO, Pruessmann KP et al. B1(+) phase mapping at 7 T and its application for in vivo electrical conductivity mapping. Magn Reson Med. 2012;67:552-561.
34. Zhang X, Van de Moortele PF, Schmitter S, He B. Complex B1 mapping and electrical properties imaging of the human brain using a 16-channel transceiver coil at 7T. Magn Reson Med. 2013;69:1285-1296.
35. Schröder JM, Bohl J, Von Bardeleben U. Changes of the ratio between myelin thickness and axon diameter in human developing sural, femoral, ulnar, facial, and trochlear nerves. Acta neuropathologica. 1988;76:471-483.

36. Meier DS, Guttmann CR. MRI time series modeling of MS lesion development. Neuroimage. 2006;32:531-537.
37. Meier DS, Weiner HL, Guttmann CR. MR imaging intensity modeling of damage and repair in multiple sclerosis: relationship of short-term lesion recovery to progression and disability. AJNR Am J Neuroradiol. 2007;28:1956-1963.
38. Meier DS, Weiner HL, Guttmann CR. Time-series modeling of multiple sclerosis disease activity: a promising window on disease progression and repair potential? Neurotherapeutics. 2007;4:485-498.
39. Yao B, Li T-Q, Gelderen Pv, Shmueli K, de Zwart JA, Duyn JH. Susceptibility contrast in high field MRI of human brain as a function of tissue iron content. Neuroimage. 2009;44:1259-1266.
40. Walsh AJ, Blevins G, Lebel RM, Seres P, Emery DJ, Wilman AH. Longitudinal MR Imaging of Iron in Multiple Sclerosis: An Imaging Marker of Disease. Radiology. 2014;270:186-196.
41. Chen JT, Easley K, Schneider C et al. Clinically feasible MTR is sensitive to cortical demyelination in MS. Neurology. 2013;80:246-252.
42. Mainero C, Benner T, Radding A et al. In vivo imaging of cortical pathology in multiple sclerosis using ultra-high field MRI. Neurology. 2009;73:941-948.
43. Keil B, Wald LL. Massively parallel MRI detector arrays. J Magn Reson. 2013;229:75-89.
44. Schmierer K, Parkes HG, So PW et al. High field (9.4 Tesla) magnetic resonance imaging of cortical grey matter lesions in multiple sclerosis. UCL Institute of Neurology, Department of Neuroinflammation, NMR Research Unit, London, UK. k.schmierer@qmul.ac.uk: England; 2010:858.
45. Schmierer K, Thavarajah JR, An SF, Brandner S, Miller DH, Tozer DJ. Effects of formalin fixation on magnetic resonance indices in multiple sclerosis cortical gray matter. J Magn Reson Imaging. 2010;32:1054-1060.
46. Fischl B. FreeSurfer. Neuroimage. 2012;62:774-781.
47. Cohen-Adad J, Benner T, Greve D et al. In vivo evidence of disseminated subpial T2* signal changes in multiple sclerosis at 7 T: a surface-based analysis. Neuroimage. 2011;57:55-62.

48. Fernandez-Seara MA, Wehrli FW. Postprocessing technique to correct for background gradients in image-based R*(2) measurements. Magn Reson Med. 2000;44:358-366.

Appendix: Ethics Approval

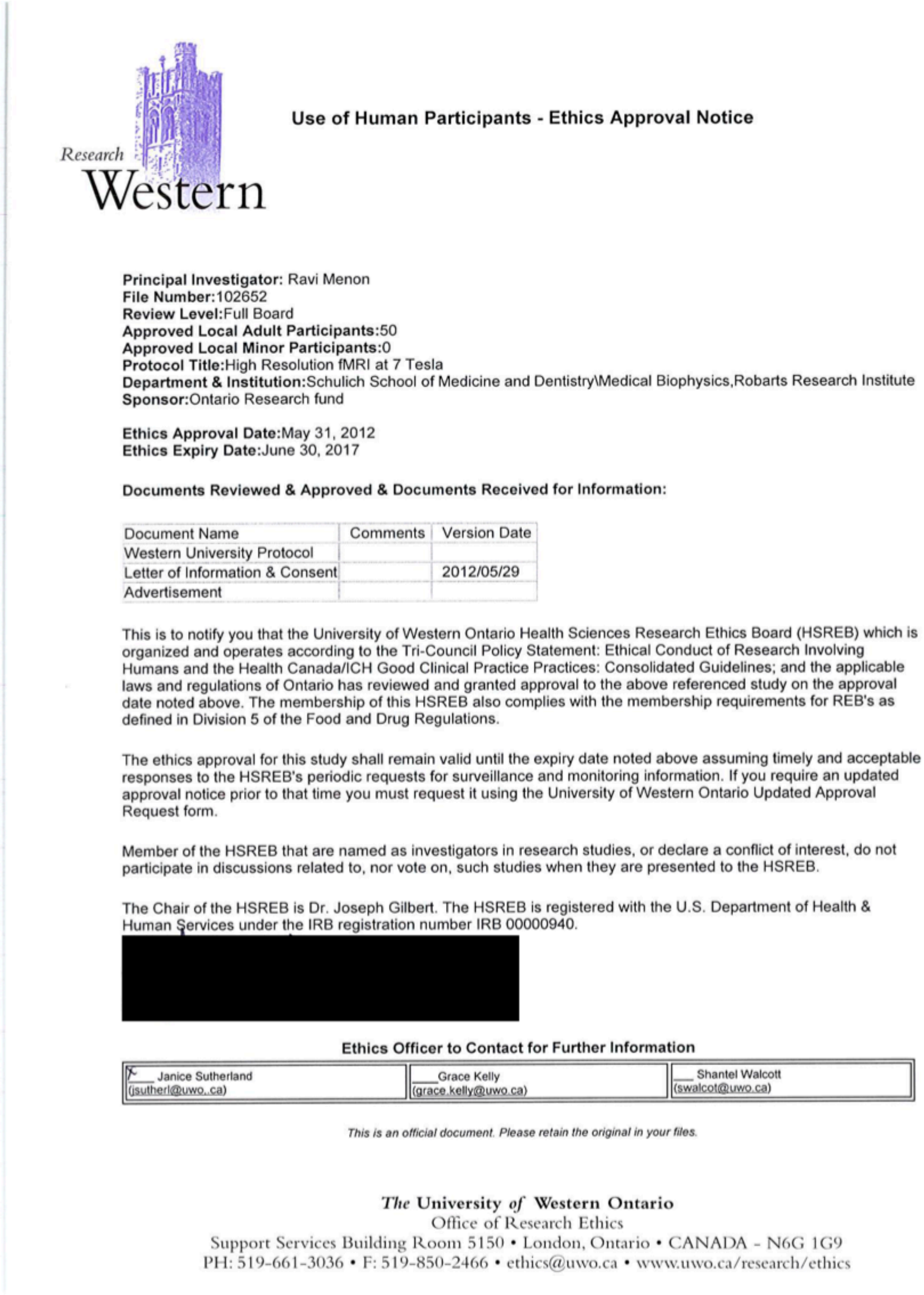

Research
Western

Use of Human Participants - Ethics Approval Notice

Principal Investigator: Ravi Menon
File Number:102652
Review Level: Full Board
Approved Local Adult Participants:50
Approved Local Minor Participants:0
Protocol Title: High Resolution fMRI at 7 Tesla
Department & Institution: Schulich School of Medicine and Dentistry\Medical Biophysics,Robarts Research Institute
Sponsor: Ontario Research fund

Ethics Approval Date: May 31, 2012
Ethics Expiry Date: June 30, 2017

Documents Reviewed & Approved & Documents Received for Information:

Document Name	Comments	Version Date
Western University Protocol		
Letter of Information & Consent		2012/05/29
Advertisement		

This is to notify you that the University of Western Ontario Health Sciences Research Ethics Board (HSREB) which is organized and operates according to the Tri-Council Policy Statement: Ethical Conduct of Research Involving Humans and the Health Canada/ICH Good Clinical Practice Practices: Consolidated Guidelines; and the applicable laws and regulations of Ontario has reviewed and granted approval to the above referenced study on the approval date noted above. The membership of this HSREB also complies with the membership requirements for REB's as defined in Division 5 of the Food and Drug Regulations.

The ethics approval for this study shall remain valid until the expiry date noted above assuming timely and acceptable responses to the HSREB's periodic requests for surveillance and monitoring information. If you require an updated approval notice prior to that time you must request it using the University of Western Ontario Updated Approval Request form.

Member of the HSREB that are named as investigators in research studies, or declare a conflict of interest, do not participate in discussions related to, nor vote on, such studies when they are presented to the HSREB.

The Chair of the HSREB is Dr. Joseph Gilbert. The HSREB is registered with the U.S. Department of Health & Human Services under the IRB registration number IRB 00000940.

[redacted]

Ethics Officer to Contact for Further Information

✓___ Janice Sutherland (jsutherl@uwo..ca)	___Grace Kelly (grace.kelly@uwo.ca)	___ Shantel Walcott (swalcot@uwo.ca)

This is an official document. Please retain the original in your files.

The **University** *of* **Western Ontario**
Office of Research Ethics
Support Services Building Room 5150 • London, Ontario • CANADA - N6G 1G9
PH: 519-661-3036 • F: 519-850-2466 • ethics@uwo.ca • www.uwo.ca/research/ethics

Abbreviated Curriculum Vitae

David Rudko

Post-Secondary Education and Degrees

University of British Columbia
Vancouver, British Columbia, Canada
2001-2005, BSc.

University of Victoria
Victoria, British Columbia, Canada
2006-2008, MSc.

The University of Western Ontario
London, Ontario, Canada
2008 – 2014, Ph.D.

Related Work Experience	Teaching Assistant The University of Western Ontario 2008 – 2010

Publications, Presentations and Abstracts

Publications (Accepted)

Junmin Liu, **Rudko D.A**., Gati J.S., Menon R.S., Drangova M. "Inter-echo variance as a weighting factor for multi-channel combination in multi-echo acquisition for local frequency shift mapping," **Magnetic Resonance in Medicine (Accepted, March 2014),** (International Journal, PhD work).

Rudko D.A., Solovey I., Gati J.S., Kremenchutzky M., Menon R.S. "Improved Identification of MS Disease-Relevant Changes in Grey and White Matter Using Susceptibility-Based Ultra-High Field MRI," **Radiology (Accepted, March 2014),** (International Journal, PhD work).

Rudko D.A., Klassen L.M., de Chickera S.N, Gati J.S., Dekaban G.A., Menon R.S. "Origins of R_2^* orientation dependence in grey and white matter," **Proceedings of the National Academy of Sciences of the United States of America.** 2014 Jan 7;111(1):E159-67. (International Journal; PhD work).

Goubran M., **Rudko D.A**., Santyr B., Gati J., Szekeres T., Peters T.M., Khan A.R. "In vivo normative atlas of the hippocampal subfields using multi-echo susceptibility imaging at 7 Tesla," **Human Brain Mapping,** 2013 Dec 13. [Epub ahead of print]. (International Journal, PhD work).

Campbell W.G., **Rudko D.A**., Braam N.A., Wells, D.M., Jirasek A. "A prototype fan-beam optical CT scanner for 3D dosimetry," Med Phys. 2013 Jun;40(6):061712. (International Journal, MSc. work).

Rudko, **D**. (August 2008) "Prototype Fan-Beam Optical CT Scanner for Three-Dimensional Radiotherapy Dose Verification," (129 pages) **Master's Thesis, University of Victoria** (MSc work).

Presentations (Oral)

Rudko D., Klassen L.M., de Chickera S.N, Dekaban G.A., Menon R.S. (February 2011) "Susceptibility Mapping in Rat Deep Brain Structures using UHF MRI," **Imaging Network Ontario Symposium** (Provincial Conference, PhD work).

Rudko D., Wells D., Jirasek A. (March 2008) "Three-Dimensional Radiation Therapy Dose Verification with Optical Computed Tomography," **Western Canadian Medical Physics Conference** (National Conference, MSc work).

Rudko D., Wells D., Jirasek A. (June, 2008) "Prototype Fan Beam Optical Computed Tomography Scanner for Three-Dimensional Radiation Therapy Dose Verification," **Canadian Organization of Medical Physics, J.R. Cunningham Young Investigators Symposium** (National Conference, MSc work).

Abstracts Accepted (with Poster Presentation)

Streijger F., Lee J.H.T., Manouchehri N., Anderson L., **Rudko D**, Dekaban G.A., Kwon B.K. (November, 2013) "Characterizing white matter damage in porcine spinal cord with quantitative MRI and histology," **Society for Neuroscience 2013 Annual Meeting** (International Conference, PhD work).

Rudko D.A., Gati J.S., Kremenchutzky M., Menon R.S. (April 2013) "Quantitative high-field MRI of Multiple Sclerosis," **International Society for Magnetic Resonance in Medicine 2013 Annual Meeting** (International Conference, PhD work).

Rudko D.A., Gati J.S., Kremenchutzky M., Menon R.S. (February 2013) "Quantitative high-field MRI of Multiple Sclerosis," **Imaging Network Ontario Symposium** (Provincial Conference, PhD work).

Rudko, D., Klassen L.M., de Chickera S.N, Dekaban G.A., Menon R.S. (August 2012) "Biophysical Examination of MRI Susceptibility Contrast Parameters in Fixed Rat Brain Tissue at 9.4 T," **Gordon Research Conference on In Vivo Magnetic Resonance,** (International Conference, PhD work).

Rudko, D., Klassen L.M., de Chickera S.N, Dekaban G.A., Menon R.S. (March 2012) "Biophysical Analysis of Magnetic Susceptibility Contrast in Rat Brain Tissue at 9.4 T," **2012 University of Toronto Neuroinflammation Symposium and Manitoba/Ontario Regional Researchers in Training endMS Retreat,** (National Conference, PhD work).

Rudko D., Klassen L.M., de Chickera S.N, Dekaban G.A., Menon R.S. (March 2012) "Biophysical Analysis of Magnetic Susceptibility Contrast in Rat Brain Tissue at 9.4 T," **London Health Graduate Research Day Annual Meeting** (Provincial Conference, PhD work).

Rudko D., Klassen L.M., de Chickera S.N, Dekaban G.A., Menon R.S. (May 2011) "Susceptibility Mapping in Rat Deep Brain Structures using UHF MRI," **International Society for Magnetic Resonance in Medicine 2011 Annual Meeting** (International Conference, PhD work).

Rudko, D., Klassen L.M., Meakin S., Menon R.S. (May 2010) "Susceptibility-Corrected Magnetization Transfer Contrast in a Mouse Model of Glioblastoma Multiforme," **International Society for Magnetic Resonance in Medicine 2010 Annual Meeting** (International Conference, PhD work).

Rudko D., Klassen L.M., Meakin S., Menon R.S. (March 2010) "Susceptibility-Corrected Magnetization Transfer Contrast in a Mouse Model of Glioblastoma Multiforme," **Ontario Institute for Cancer Research Annual Scientific Meeting** (Provincial Conference, PhD work).

Scholarships and Awards

09/12 Queen Elizabeth II Graduate Scholarship in Science and Technology
Eligibility: Demonstration of academic excellence in graduate courses and research abilities.
Duration: 1 year
Value: $15,000/year ($5,000/term)

07/12 Gordon Research Conference on In Vivo Magnetic Resonance Trainee Stipend
Eligibility: Graduate trainee presenting novel research at the Gordon Research Conference.
Duration: One-time award
Value: $500

09/11 Western Graduate Thesis Research Award
Eligibility: Competition open to all graduate students registered at University of Western Ontario.
Duration: One time award
Value: $600

02/11 ISMRM Educational Stipend
Eligibility: Graduate student attending the educational portion of the ISMRM conference; travel award.
Duration: One time award
Value: $450

09/08 Western Graduate Research Scholarship
Eligibility: Registered graduate student at University of Western Ontario with an academic average >80%.
Duration: 3 years
Value: $3,600/year

09/08 Schulich Graduate Scholarship (declined)
Eligibility: Registered graduate student at University of Western Ontario with an academic average >80%.
Duration: 1 year
Value: $6,627

09/07 Pacific Century Graduate Scholarship
Eligibility: Awarded to outstanding graduate students based on academic and research achievement.
Duration: 1 year
Value: $10,000

09/07 University of Victoria Graduate Award
Eligibility: Recipients must be registered fulltime in a graduate program at University of Victoria with an overall graduate academic average of >80%.
Duration: 1 year
Value: $800

Teaching Experience

Teaching Assistant/ Laboratory Instructor	09/09 – 04/10	TA for Physics 1028/1029, a first year physics lab course at University of Western Ontario. One year duration; taught theory involved in lab sessions, outlined experimental procedures, assisted students and graded lab assignments.
Teaching Assistant/ Laboratory Instructor	09/06 - 04/08	TA for Physics/Electrical Engineering 216 (Electricity and Magnetism) at the University of Victoria. Two year duration; taught the theory for each lab session, demonstrated experiments, guided students in their investigations and graded assignments.
Teaching Assistant	09/07 - 12/07	TA for Physics 102 (Introductory Physics) at the University of Victoria. One term duration; graded course assignments and mentored students enrolled in course.